INVESTIGATION OF FRACTURE MECHANISMS IN THE DUCHESNE FAULT ZONE, UINTA BASIN, NORTHEASTERN UTAH:

The Role of Fluid Overpressures and Other Processes

Department of Earth &
Environmental Science
New Mexico Tech
Socorro, NM 87801

by

JENNIFER LYNN SMITH

Submitted in partial fulfillment of the requirements for the

Masters of Science in Hydrology

New Mexico Institute of Mining and Technology, Socorro, NM

December 2004

ABSTRACT

The Duchesne Fault and Fracture Zone (DFZ) in the Uinta Basin, northeastern Utah is an area of local intense faulting and fracturing. The exact cause of this fracturing has not been determined previously and served as a major motivation for this research. The potential to investigate the role that high fluid pressures may play in fracture initiation and propagation when other fracturing mechanisms are present made the DFZ a desirable study site. This area coincides with other possible fracturing mechanisms, including anomalously high fluid pressures, minor local flexure, and a change in facies/lithology.

We developed three specific conceptual models that attempt to take into account field observations and measured data. These models explore different potential scenarios for the history of the DFZ with emphasis on the fracturing. Field observations were made and rock samples collected from the vicinity of the DFZ. These samples were characterized in laboratories at New Mexico Tech and the New Mexico Bureau of Geology and Mineral Resources in terms of hydrological (porosity), mechanical (tensile and compressive failure strength), and physical (rock framework, mineralogy, cementation, and grain size) parameters. Results were analyzed for geographical trends and physical controls on strength.

No distinct geographical trend in material properties was identified; a general trend of decreasing grain size from north to south across the DFZ was noted from the fieldwork. In areas nearby the DFZ, other local flexures of comparable magnitude in the same rock unit and possessing a similar geologic history do not show such intense fracturing and/or faulting similar to that observed in the DFZ. The

difference between the DFZ anticline and these other anticlines is the presence of fluid pressures; the fluid overpressures do not exist in the areas of the other anticlines.

No evidence was found in this research against the case of fracturing induced by high fluid pressure. All of the observations made and data collected suggest that fluid pressures most likely played a crucial role in the DFZ fracturing. Based on this interpretation, fluid pressures are assumed to have been critical in the history of the DFZ.

ACKNOWLEDGEMENTS

This research couldn't have been done without the help of so many different people. Everyone provided a unique perspective and input to this work.

I would like to extend my thanks to Brian McPherson, my academic advisor, as well as my committee members – Ronald Bruhn (University of Utah), S. Robert Bereskin, and John Wilson – for all of their insight and discussions. Laurel Goodwin was also a huge help and support through this project in so many different ways. Many thanks to David Boutt who has been able to help me with everything from brainstorming to labwork and data interpretation. The expertise of Craig Morgan (Utah Geological Survey) and Alicia Groeger in the field was invaluable. Thanks to Dana Ulmer-Scholle who aided in the petrographic analysis.

I spent countless hours in the laboratory, and couldn't have done it without the help and assistance of many. Thanks to Aaron Abel, Adam Barker, Mike Blanchard, Alan Erickson, Weonshik Han, Kalman Oravez, Diane Meier, Maxwell Sandford, and others. I'd also like to thank Susan Delap (help with graphics), Lynn Heizler (SEM analysis), Chris McKee (XRD analysis), and Erich Peterson, University of Utah (fluid inclusion analysis).

Funding for this research was eclectic, ranging from the Alberta Geological Survey to the Petroleum Recovery Research Center, and including everything in between- Gas Technology Institute, Research Partnership to Secure Energy for America, Institute of Geophysics and Planetary Physics at Los Alamos National Laboratory, New Mexico Tech's Graduate Student Association, and the McPherson Discretionary Fund.

Finally, I would like to extend my gratitude to Matthew Sherer (perhaps one of the most fracture-aware computer programmers out there) for all of his support and time spent listening to stories about the Uinta Basin...

TABLE OF CONTENTS

	Page
ABSTRACT	n/a
ACKNOWLEDGEMENTS	ii
TABLE OF CONTENTS	iii
LIST OF FIGURES	vi
LIST OF TABLES	viii
Chapter 1: INTRODUCTION	1
1.1 Driving Concept	1
1.2 Evidence	3
1.3 Hypothesis	4
Chapter 2: SITE DESCRIPTION	5
2.1 Geologic Setting	5
2.2 Hydrodynamics	10
2.2.1 General Hydrology	10
2.2.2 Fluid Overpressures	12
2.3 Geologic History	14
2.3.1 Uinta Basin	14
2.3.2 Specific to the DFZ	17
2.4 Fieldwork and Observations	19
2.4.1 Motivation	19
2.4.2 Sampling Strategy	20
2.4.3 Observations	21

Chapter 3: CONCEPTUAL MODEL 35
3.1 Motivation for Development 35
3.2 Evidence used in Development 36
3.2.1 Observations 36
3.2.2 Other Applicable Considerations 40
3.3 Possible Scenarios 44
3.3.1 CM#1: High fluid pressure / fault-valve 44
3.3.2 CM#2: Extension-Anticline 47
3.3.3 CM#3: Fractures unrelated to high fluid pressures 49
3.3.4 Some Alternative Combination 51
3.4 Summary: Conceptual Model 51
Chapter 4: ROCK CHARACTERIZATION 52
4.1 Hydrological 53
4.1.1 Porosity 53
4.1.2 Permeability, Diffusivity, and Storativity 57
4.1.3 Paleo-Pressure and Temperature 58
4.2 Mechanical 59
4.2.1 Tensile Strength 59
4.2.2 Compressive Strength 63
4.3 Physical 71
4.3.1 Rock Framework 71
4.3.2 Mineralogy 74
4.3.3 Cementation 79
4.4 Summary: Rock Characterization 81
Chapter 5: INTERPRETATION and DISCUSSION 82
5.1 Material-Controlled Fracturing 83

5.1.1 Geographical Trends 83
5.1.2 Physical Controls on Strength 85
5.1.3 Micro- versus Macro-Scale Trends 86
5.1.4 SUMMARY: Material-controlled fracturing 88
5.2 Flexure-Controlled Fracturing 88
5.2.1 Reasons CM#2 Cannot Explain the DFZ 89
5.2.2 Reasons CM#3 Cannot Explain the DFZ 92
5.3 Flexure/Pressure-Controlled Fracturing 92
5.3.1 CM#1: A Consistent Model for the DFZ 93
5.3.2 Numerical Modeling 93
5.4 Summary and Conclusions 94
Chapter 6: RECOMMENDATIONS for FUTURE WORK 98
APPENDIX I: Sample Summary and Description 103
APPENDIX II: Lab Procedures for Rock Properties Testing 108
APPENDIX III: Characteristics of Uinta Formation Aquifers 148
APPENDIX IV: SEM images (electronic version only) 151
REFERENCES 152

LIST OF FIGURES

Figure		Page
2-	1. Map of the Uinta Basin, northeastern Utah	6
	2. General structure and Tertiary stratigraphy	7
	3. Flow vectors for the Flagstaff Mbr of the Green River Fm	11
	4. Observed hydraulic head in the Flagstaff Mbr	13
	5. Chart illustrating related structural and tectonic events in the vicinity of the DFZ	16
	6. Locations and sample numbers	20
	7. Uinta Fm, southwestern part of FZ; #38-39	23
	8. Uinta Fm, southeastern part of FZ; #21-26	24
	9. Uinta Fm, north of FZ; #35-37	25
	10. Uinta/Duchesne River Fm, north of FZ; #42, 47	26
	11. Large-scale fault feature; #1-15	27
	12. Smaller-scale fault feature showing slickensides; #1-15	28
	13. Fault with displacement of approximately 3 m; #21-26	28
	14. Fractured sandstone unit; #21-26	30
	15. Fractured outcrop in the western fault zone; #31	30
	16. Gilsonite in the vicinity of the Duchesne Graben; #32-34	32
	17. Concretions in Balcron area; #1-15	33
3-	18. Hydraulic fracture	40
	19. Basic illustration of cyclic fault-valve behavior	41
	20. Conceptual model #1: High fluid pressures / fault valve.	45
	21. Conceptual model #2: Extension-anticline	48

22. Conceptual model #3: Fractures formation unrelated to high fluid pressures 50
4- 23. Data and corresponding graph illustrating porosity results . 54
24. Porosity as a function of location with respect to the DFZ . 56
25. Porosity as a function of depth for the Amoco samples . . . 57
26. Brazil tensile strength tests 60
27. Inherent variation present in tensile strength tests 62
28. Tensile strength as a function of location with respect to the DFZ 63
29. Compressive strength variation 69
30. Compressive strength as a function of location with respect to the DFZ 70
31. Compressive strength plotted as a function of depth . . . 70
32. Graphs of compressive and tensile strength versus grain size 73
33. SEM images illustrating the differences in grain size 75
34. SEM images illustrating samples with relatively low and high strength 76
35. Qualitative XRD results showing the major mineralogical components of the UB samples 77
36. Compressive and tensile strength versus percent cement . 80
37. Tensile and compressive failure strength versus the connectedness of the cement 81
5- 38. Effect of scale on permeability 87
39. Cross-sections of the Upper Marker of the Green River Fm . 90

LIST OF TABLES

Table		Page
2-	1. Regional joint sets in the Tertiary strata of the eastern Uinta Basin	10
	2. List of sample numbers and general location names	21
3-	3. Values of viscosity for gilsonite	39
	4. Parameters used in calculation of characteristic decay time.	42
4-	5. Values of porosity for the UB collected and Amoco samples	55
	6. Statistical analysis of measured porosity data	56
	7. Ranges and median values of porosity, hydraulic conductivity, permeability, and transmissivity for Uinta Fm aquifers	58
	8. Values of tensile strength for select UB samples	61
	9. Statistical analysis of measured tensile strength data	62
	10. Values of compressive strength for UB samples and Amoco samples	65
	11. Values of elastic parameters for UB samples and Amoco samples	66
	12. Statistical analysis of measured compressive strength data	67
	13. Statistical analysis of calculated elastic parameters	67
	14. Results of thin section analysis regarding rock type, grain size, and compaction	72

15. Results of thin section analysis regarding mineralogical and biological components 79

16. Results of thin section analysis regarding cement amount, cement type, and the character of the cement 80

17. Computed R-squared values for select parameters versus location 85

18. Calculation of slope for selected N-S sections in the Uinta Basin 91

This thesis is accepted on behalf of the
Faculty of the Institute by the following committee:

Brian McPherson
Advisor

John L Wilson

S. Robert Bowker

Ronald L Bruhn

08/23/04
Date

I release this document to the New Mexico Institute of Mining and Technology.

Jennifer Smith
Student's Signature

08/23/04
Date

Chapter 1: Introduction

1.1 DRIVING CONCEPT

Mechanisms of fracture formation have always been a topic of interest to geologists, hydrologists, and the petroleum industry. A number of factors can influence fracture initiation, and a better understanding of such mechanisms will provide insight to the resulting behavior and associated repercussions throughout the system. The Uinta Basin as a whole is a rich onshore hydrocarbon resource. The hydrodynamics and petroleum migration pathways are largely influenced by regional fracture patterns. Understanding fracturing as a part of the overall system is important since transport of both hydrocarbons and contaminants is strongly dependent on the hydrodynamics of a system, and fractures commonly lead to changes in permeability and fluid flow.

The Duchesne Fault and Fracture Zone (DFZ) is rare in that a variety of potential fracturing mechanisms are present along with a localized zone of intense fracturing and faulting. Traditional causes of fracturing cited in the Uinta Basin include: regional tectonics (Fouch et al., 1992a), uplift and erosion (Narr and Currie, 1982), local flexure such as anticlinal noses (Clem, 1985), and variations in rock strength associated with changes in lithology (Lucas and Drexler, 1976). More recently, rapid hydrocarbon generation and resulting fluid overpressures have been suggested as facilitating fracture formation (Sweeney et al., 1987; Bredehoeft et al., 1994). Overpressuring is generally an accepted means of making fracture initiation

and propagation more likely to occur through lowering the effective stress in an area (Hubbert and Rubey, 1959; Secor, 1965; Pollard and Aydin, 1988; Neuzil, 1995).

In the case of the DFZ, the definite origin or mechanisms of fracturing are unknown. This has been a subject of speculation and debate among geologists for many years in both the academic and petroleum fields. A number of researchers have worked extensively in northeastern Utah studying sedimentation and tectonics of the area on a basin-wide scale (Bruhn et al., 1986; Fouch et al., 1992a; Fouch et al., 1994). Spencer (1987) investigated hydrocarbon generation as a mechanism of overpressure in the Rocky Mountain region and suggested that vertical fractures in these areas are likely to have been caused by the rapid hydrocarbon expulsion. Other investigations have relied heavily on geologic field observations from the Uinta Basin area (Lemmon and others, 1998; Bruhn, 2001, personal communication). However, none of these studies specifically addressed the role of fluid pressures in causing the formation of fractures in the DFZ.

Another motivation for this study is the current lack of data, which is necessary for a study of relevant hydrogeological processes. Published quantitative data on the Uinta Formation, which is a major host unit of the DFZ, does not exist in any extensive manner. The DFZ is a well known and mapped feature in the Uinta Basin. However, data relating directly to this structure cannot readily be found in published sources. This deficiency has been recognized previously by others: "...Little published information exists concerning the age and structure of the fault zone or its hydrological properties" (Groeger and Bruhn, 2001); "...Little detailed work has been compiled concerning (the DFZ) extent, tectonic origin, or time of emplacement" (Lemmon and others, 1998).

This study of the DFZ was undertaken to increase our understanding of mechanisms of fracturing, specifically in the presence of high fluid pressures for the specific case of the DFZ. One objective was to use laboratory experiments to

characterize hydrological and mechanical properties of the rock units (porosity, permeability, compressive and tensile failure strength, mineralogy, and grain structure) and evaluate the corresponding relationships among them. This investigation provides an extensive foundation of quantitative data for the Uinta Formation in the immediate area of the DFZ. Development of a conceptual model to explain the DFZ history in the context of field observations and measured properties was another primary goal. These measurements and a conceptual model are a necessity for investigating mechanisms involved in the history of the DFZ.

In addition, lessons can be learned that may be applied to fracture genesis studies in general.

1.2 EVIDENCE

A variety of factors and uncommon coincidences suggest high fluid pressures may have played a role in fracturing in the DFZ. Anomalously high fluid pressures are documented north of the DFZ; these overpressures terminate approximately at the northern boundary, suggesting a relationship between the pressures and the DFZ. Large-scale gilsonite dikes present in the eastern Uinta Basin have been extensively studied by Verbeek and Grout (1992) and determined to be the result of hydraulic extension fracturing. Abundant mineralization (calcite and gypsum) in some fracture sets and concretions at the surface indicate prior presence of fluids that may have been forced upward due to some driving force or gradient directed toward the surface.

This rare convergence of fluid overpressures terminating at the northern DFZ boundary, gilsonite dikes, and the prior presence of fluids in the vicinity of the DFZ make it an ideal candidate for investigation of competing mechanism(s) of fracture

formation in a single location, as well as determining the potential role of fluid pressures.

1.3 HYPOTHESES

This work is based on the premise that anomalously high fluid pressures played a significant role in fracture initiation and propagation in the DFZ. A number of hypotheses were considered throughout the evolution of this research. Two main hypotheses are:

(1) The rocks in the DFZ are mechanically different than those outside. Spatial patterns can be analyzed and used to determine why rocks in the DFZ are extensively fractured while those outside are not. Mechanical properties alone may be used to determine what magnitude of stress the rock could withstand before fracturing.

(2) Hydrologic properties influence the mechanical strength (or response) of rocks. The important related implication is that rock units with low permeability and/or diffusivity would be more susceptible to hydraulic fracturing. High fluid pressures are inclined to develop within units where the rate of overpressure generation (hydrocarbon generation in this case) exceeds the rate of pressure dissipation or flow out of the unit.

Additional specific hypotheses were developed as a part of this research project and are presented in the form of detailed conceptual models (Chapter 3). These address different possible mechanisms of fracture in the DFZ including:

(3a) formation due to local flexure aided by abnormally high fluid pressures,

(3b) formation due to local flexure only, and

(3c) formation before high fluid pressures.

Chapter 2: Site Description

2.1 GEOLOGIC SETTING

The Uinta Basin is a topographic and structural basin in northeastern Utah that covers an area of more than 16,000 km^2. The basin developed during the Laramide Orogeny and is surrounded by the Uinta Mountains to the north, the Wasatch Mountains to the west, the San Rafael Swell and Uncompahgre Uplift to the south, and the Douglass Creek Arch and Piceance Basin to the east (Figure 1). The deepest portion of the synclinal basin is the northern margin, which is bounded by a large scale, northward dipping basement thrust fault (Campbell, 1978). The topographic low is approximately in the center of the basin. The basin is asymmetric, with a more steeply sloping north limb (10°-35° S) than south limb (4°-6° N).

The basin is filled with more than 9,000 m of material from the Cambrian to Tertiary, and up to an additional 6,000 m of Tertiary strata consisting mainly of alluvial and lacustrine sedimentary limestones, shales, and sandstones that were deposited during a time of fluctuating lake levels in response to the Laramide uplift. These strata are thicker in the northern part of the basin due to asymmetry. Tertiary units in the Uinta Basin directly overlie the Cretaceous Mesaverde Group and include: North Horn Fm (oldest), Wasatch/Colton Fm, Flagstaff limestone, Green River Fm (Willow Creek Mbr , Douglas Creek Mbr, Garden Gulch Mbr, Parachute Creek Mbr, Evacuation Creek Mbr), Uinta Fm, Duchesne River Fm, and Browns Park Fm (youngest). Quaternary glacial deposits and alluvium are found atop portions of

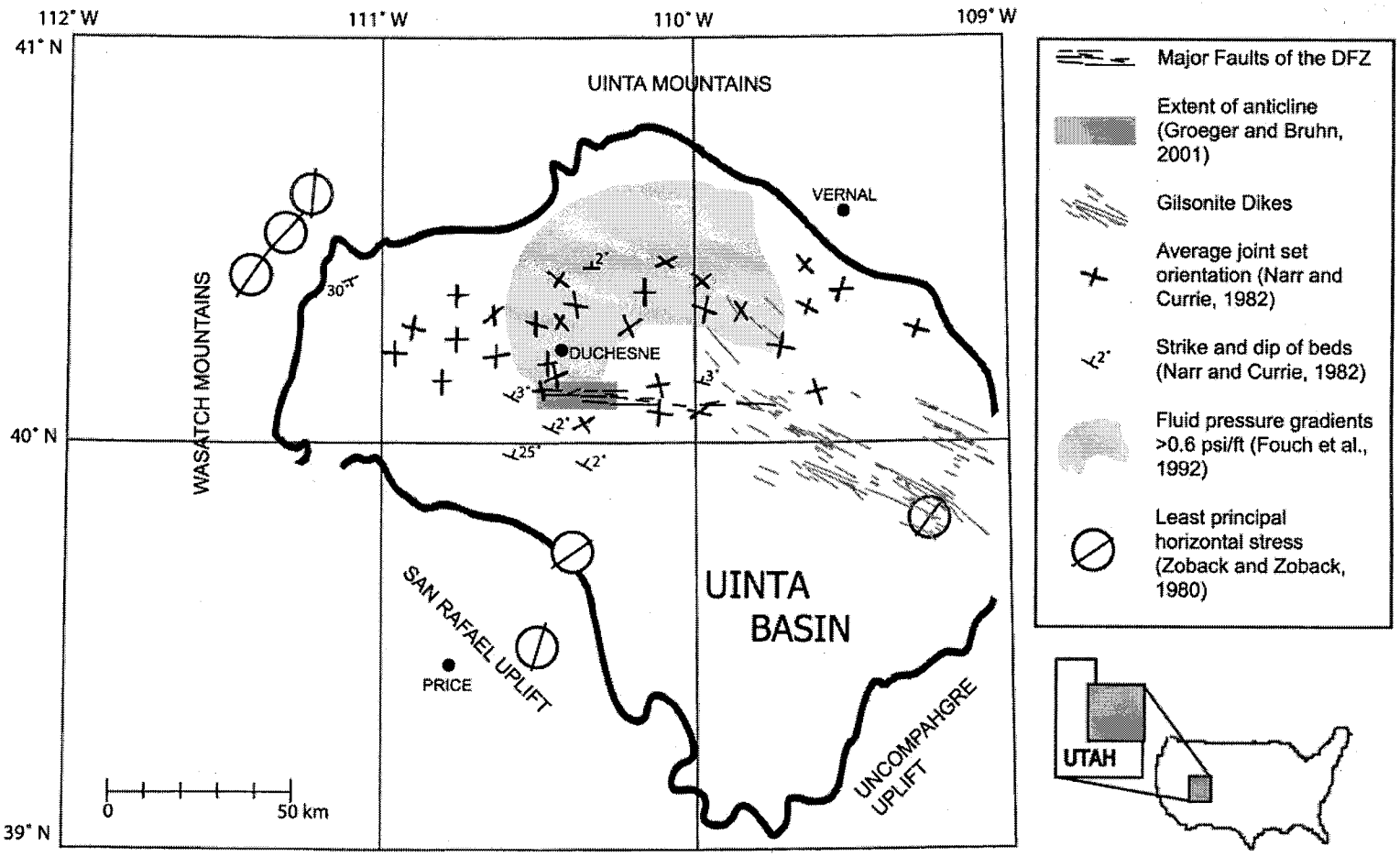

Figure 1: Map of the Uinta Basin, northeastern Utah; relevant structures and measurements include: the DFZ, the extent of the Duchesne Graben and associated anticline, average joint set measurements, strike and dip measurements of bedding, extent of fluid pressure gradients >0.6 psi/ft in Tertiary strata, and least principle horizontal Quaternary stress.

these Tertiary deposits. Figure 2 illustrates the general structural shape and stratigraphy; the general cross section shown is oriented N-S through the central area of the basin.

Total uplift of Tertiary strata since time of deposition is estimated to range from 1,800 m (Narr and Currie, 1982) to more than 3,000 m (Johnson, 1992). The timing of regional uplift varies, but is generally assumed to have started ~10 Ma (Johnson and Nuccio, 1993). Workers have used a variety of methods to estimate the thickness of overburden removed from the basin, including geologic/stratigraphic evidence (Narr and Currie, 1982), fluid inclusions (Narr and Currie, 1982), kerogen kinetic modeling (Sweeney et al., 1987), burial history modeling (Pitman et al., 1982), organic geochemistry (Pitman et al., 1982), vitrinite reflectance (Pitman et al., 1982; Johnson and Nuccio, 1993), and R_m-depth profiles (Johnson and Nuccio, 1993). Narr and Currie (1982) estimated 875 to more than 1,825 m removed

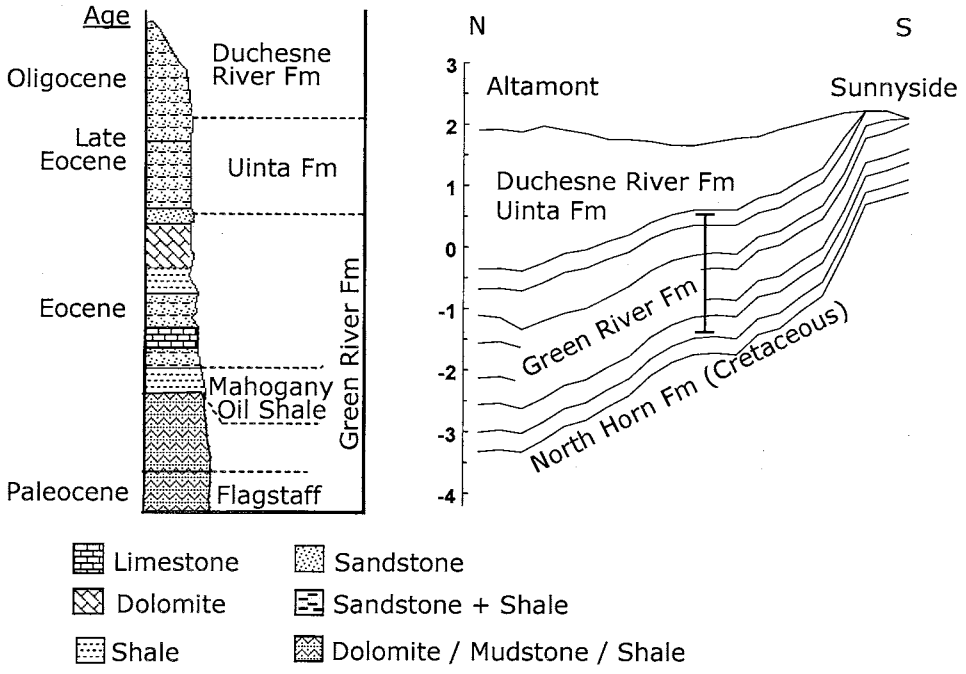

Figure 2: General structure and Tertiary stratigraphy of the Uinta Basin; the location of the cross section is through the central part of the basin, and is oriented N-S; from McPherson, 1996.

for the central part of the basin based on geologic evidence, and results of fluid inclusion studies led to estimates of 339 to 2,890 m of removal in the Altamont field.[1] Pitman et al. (1987) and Pitman et al. (1982) estimated an erosion thickness of 1,000 m for the Pariette Bench and Natural Buttes field area using a combination of vitrinite reflectance, burial history modeling, and organic geochemistry.

As a whole, the Uinta Basin is a rich onshore petroleum resource. The largest oil and gas fields produce from reservoirs in the Green River and/or lateral and temporal equivalents in the Wasatch, Colton, and North Horn Fms (Fouch et al., 1992a). These producing units consist primarily of open and marginal lacustrine facies. Oil shale (such as the Mahogany) is especially rich as a source rock. The Green River Fm is perhaps the most important unit in terms of hydrocarbon production, and has been recognized for its extensive oil shales, gilsonite, oil, and gas. Alluvial rocks in the basin commonly act as stratigraphic traps for oil migrating from down-dip lacustrine reservoirs (Fouch et al., 1994). For more detail on the Green River petroleum system in the Uinta Basin, refer to Ruble et al. (2001) and Fouch et al. (1994).

The DFZ is located in the central part of the basin, directly south and east of the town of Duchesne (Figure 1). It consists of a series of prominent east-west trending lineaments assumed to be the expression of normal faults (Ray et al., 1956, cited in Groeger, 2001; Bereskin et al., 1993). In general, these faults and major fractures trend N 80° W (Lemmon and others, 1998). Typical displacements along these faults range from several centimeters to 30 m and include no evidence of horizontal movement (Bereskin et al., 1993). The fault zone can be traced for ~58 to 68 km east to west (Lemmon and others, 1998) and is approximately 5 km wide. The region coincides with a present day facies transition from marginal lacustrine

[1] The Altamont field is located in the north-central part of the basin; Pariette Bench is located slightly northeast of the town of Duchesne; Natural Buttes is located directly to the east of Pariette Bench.

and alluvial facies to the north, changing to open lacustrine to the south (Fouch et al., 1992a). Groeger and Bruhn (2001) determined that the Duchesne Graben, located in the western part of the DFZ, is a structural half-graben with shallow basal detachment on the south-dipping master fault. The same study concluded that the graben is breached by a subtle anticline which spans the DFZ. Measured dips along the limbs of this anticline are not common; those that exist range from 4° to 16°. In addition to this documented anticline, a number of others exist in the area (Bereskin, 2001, personal communication; data from McPherson, 1996). The location and amplitude of the documented anticline, as well as implication for the conceptual model of the DFZ, will be discussed in Section 5.2.

An area of prominent gilsonite veins is located in the eastern part of the Uinta Basin and intersects the easternmost edge of the DFZ (Figure 1). Spatial relationships between the gilsonite dikes and the faults suggest that the DFZ pre-dates the gilsonite in that region (Lemmon and others, 1998; Bereskin, Bruhn, 2001, personal communication). Most of the dikes are approximately vertical and strike N 40°-70° W, a trend remarkably different from the east-west orientation of the DFZ. The gilsonite veins are genetically related to the Uncompahgre Uplift (Narr and Currie, 1982). They are associated with abnormally high pore-fluid pressures and hydrocarbon generation in the region (Monson and Parnell, 1992; Verbeek and Grout, 1992). For a detailed discussion of the structural evolution of the gilsonite dikes, refer to Verbeek and Grout (1992; 1993).

Five regional joint sets in the Tertiary strata of the eastern Uinta Basin were identified by Verbeek and Grout (1992). Relative age, common strike, and abundance are listed in Table 1. Joint sets F1, F2, and F3 have been dated 43-10 Ma; sets F3 and F4 formed with regional uplift, beginning ~10 Ma (Verbeek and Grout, 1992). Verbeek and Grout (1992) concluded that the fractures occupied by

the gilsonite are not part of any regional joint system. The estimated age of the gilsonite is older than the F2 joint set, but the gilsonite in the dikes had not solidified by the time of the F2 joint set. Therefore, the F2 joint set and the gilsonite dikes are believed to be similar in age, but not exactly (Verbeek and Grout, 1992).

SET	STRIKE RANGE	ABUNDANCE
F1 (oldest)	N 15°-30° W	Sparse
F2	N 55°-85° W	Very abundant
F3	N 60°-80° E	Moderate
F4	N 15°-40° E	Very abundant
F5 (youngest)	N 65°-85° W	Sparse

Table 1: Regional joint sets in the Tertiary strata of the eastern Uinta Basin (Verbeek and Grout, 1992).

2.2 HYDRODYNAMICS

2.2.1 GENERAL HYDROLOGY

McPherson (1996) modeled the hydrodynamics for the Flagstaff member of the Green River Fm. Two end-member cases for the burial history were considered: (1) an early uplift model, with uplift beginning at ~35-30 Ma and (2) a late uplift model, with uplift beginning at ~10 Ma. (Geologic history and tectonics are discussed in Section 2.3.) Results at a time of 10 Ma in the form of flow vectors from the early uplift model are shown in Figure 3a. Flow is generally oriented from the topographic highs in the north and the south towards the center of the basin. Discharge is concentrated in a limited zone in the central part of the basin east of the Green River, which is very similar to present-day flow patterns. Figure 3b illustrates results from the late uplift model. In this case, water flows primarily from the north to south. The discharge area is spread over a larger area in the southern part of the basin.

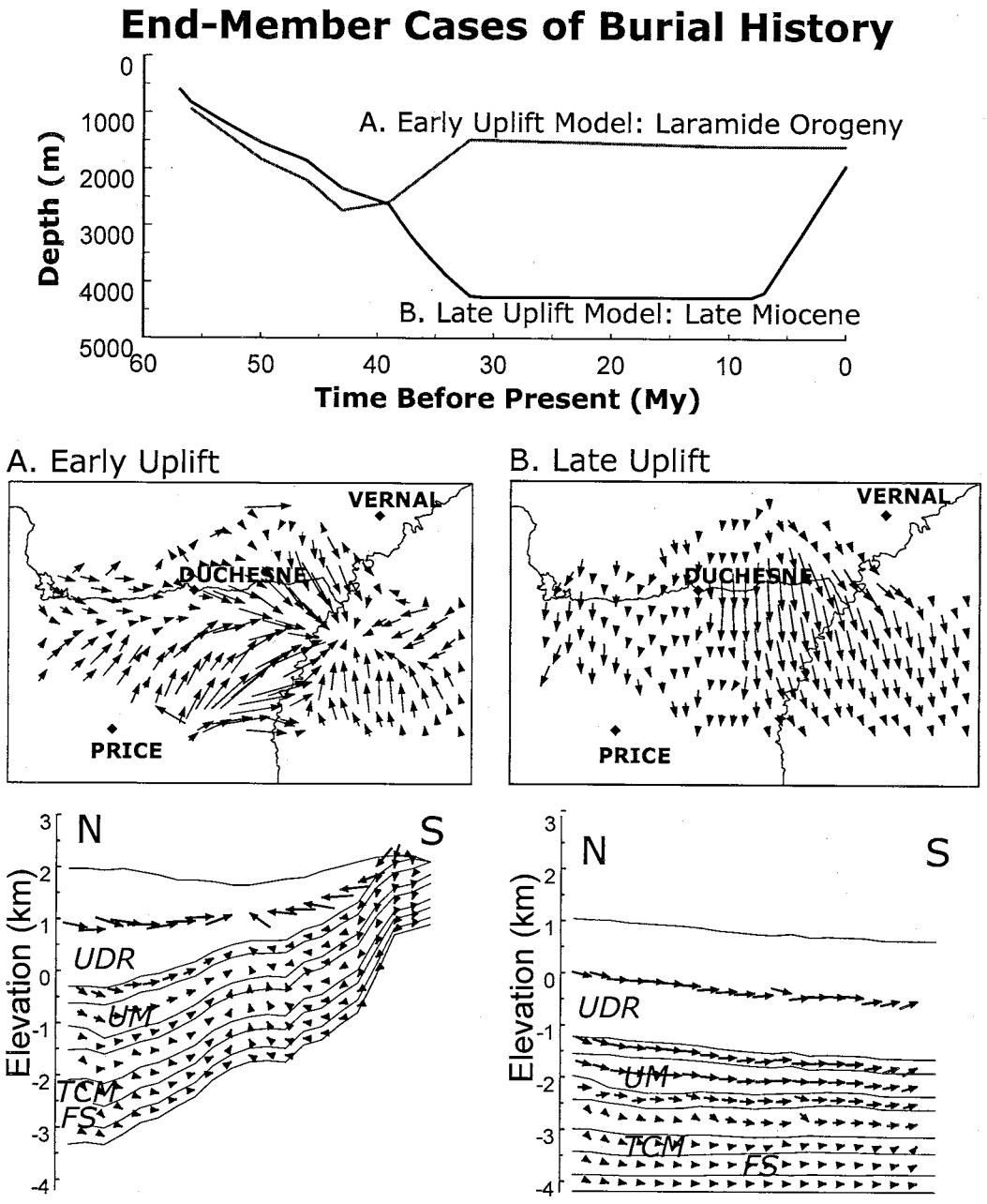

Figure 3: Map view of flow vectors for the Flagstaff Mbr of the Green River Fm and cross-sectional view oriented N-S through the central Uinta Basin corresponding to the (A) early and (B) late uplift models at 10 Ma; UDR= Uinta/Duchesne River Fm; UM= Upper Marker, Green River Fm; TCM= top of carbonate marker, Green River Fm; FS= Flagstaff Mbr; from McPherson, 1996.

A regional aquifer analysis was performed for the Duchesne River-Uinta aquifer in the Uinta Basin, Utah and Colorado (Glover, 1996). A paraphrased summary of some key points in this report is given in the following paragraph:

> Groundwater recharge is derived from precipitation and seepage loss from canals and streams. Discharge occurs to perennial streams. Hydraulic conductivity is dependent upon the lithology and degree of fracturing. Transmissivity within the DFZ is less than surrounding areas in the basin, as indicated by an aquifer test. Simulated steady-state hydraulic head contours for the aquifer are similar to flow patterns described by the early uplift model of McPherson (1996).

2.2.2 FLUID OVERPRESSURES

The productive Altamont-Bluebell oil field is located north of the DFZ. Spencer (1987), Fouch et al. (1992a), Bredehoeft et al. (1994), and others reported anomalously high fluid pressure gradients interpreted from drill-stem tests in Tertiary strata in this area. These overpressures are assumed to be the result of oil generation at depth in the Green River and Wasatch Fm (Spencer, 1987; Sweeney et al., 1987; Bredehoeft et al., 1994). Overpressure gradients range from 0.6 to >0.8 psi/ft (13.5 to >18 kPa/m) and seem to directly overlay the productive interval in the Altamont-Bluebell reservoir (Figure 1). Maximum observed pressures are range up to 65 MPa, or 27.5 MPa of overpressure (Bredehoeft et al., 1994). The rest of the basin and the underlying North Horn Fm appear to be normally pressured. The DFZ occurs at the boundary of the overpressured and normally pressured regions (Bredehoeft et al., 1994; McPherson and Bredehoeft, 2001).

A projection of observed hydraulic head in the Flagstaff member of the Green River Fm in the Altamont area of the Uinta Basin, modified from McPherson and Bredehoeft (2001), is shown in Figure 4. Values of observed head range from 2,000

to 6,065 m (3 km above surface in some areas). The same study modeled hydraulic head, considering a process of overpressuring as a result of oil generation. When fluid pressures exceeded the least principle stress, the permeability of the rock units was increased by an order of magnitude as an ad hoc method of fracture simulation. The modeled fluid pressure results are qualitatively consistent for the northern part of the basin. In the southern portion the model overpredicts pressures, however. In reality, they must have had an escape route by which to diffuse. McPherson and Bredehoeft (2001) recognized this discrepancy but never reconciled the unusual correlation between high fluid pressures and faulting in the DFZ. The possibility that the DFZ is directly related to this coincident and sharp drop in observed fluid pressures contributed to the motivation for this study.

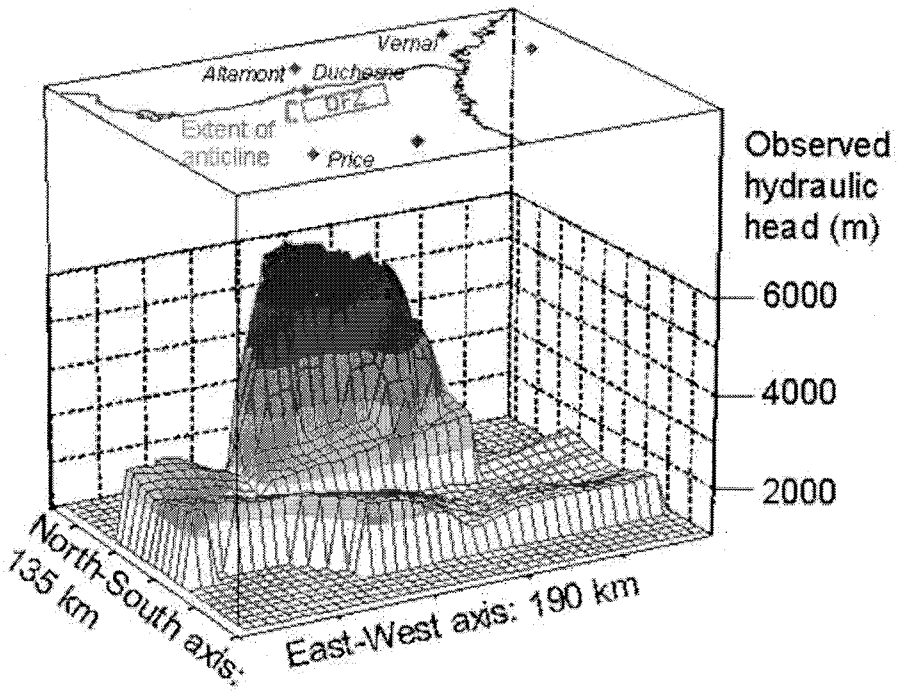

Figure 4: Observed hydraulic head in the Flagstaff Mbr, Green River Fm; the DFZ and the approximate extent of the observed anticline are designated; from McPherson and Bredehoeft, 2001 (projection of head).

2.3 GEOLOGIC HISTORY

2.3.1 UINTA BASIN

2.3.1.1 *Geology*

The area surrounding the Uinta basin was a stable shelf until the Cretaceous period. Depositional history was dominated by alluvial facies (Castlegate, Mesaverde, and North Horn Fm). Major sources of sediment included siliciclastics from the Wasatch and Uinta Mountains to the north and west, and feldspathic sands from the south (Ryder et al., 1976). The basin began to subside and take shape as the surrounding areas (including the San Rafael Swell, Uncompahgre Uplift, Uinta and Wasatch Mountains) were uplifted in the Laramide Orogeny.

Lake Uinta was created by streams emptying into the Uinta Basin by the Paleocene. Alluvial, marginal lacustrine, and some open lacustrine environments were present during this time. Depositional slope was steeper on the north than on the south flank of the basin. Sediment sources were similar to before, including quartzose sands from the west and north, and feldspathic sands from the south. The Flagstaff limestone, Wasatch (Colton), and the 'lower' Green River Fm were deposited at this time.

By Early Eocene, a major transgression resulted in extensive lacustrine environments surrounded by rims of marginal lacustrine and alluvial facies. The level of the lake was constantly fluctuating, reaching its most extensive phase in middle Eocene. The majority of the Green River Fm was deposited at this time, as were the Mahogany zone and associated oil shales. Alluvial sediments began to fill and bury Lake Uinta, which decreased in size throughout late Eocene. The Green River and the 'lower' Uinta Fm were deposited at this time.

Hydrocarbon generation began in the Green River Fm, peaked, and then slowed by late Oligocene. Petroleum generation in the Altamont-Bluebell area occurred during the Oligocene and early Miocene (Fouch, 1994). The Duchesne River Fm was deposited late in the Oligocene. Tertiary strata underwent post-Eocene uplift and subsequent erosion.

For a detailed discussion of Tertiary sedimentation in the western Uinta Basin, the reader is referred to Ryder et al. (1976).

2.3.1.2 *Related Tectonic Events*

Timing of uplift is critical to understanding (Rocky Mountain) foreland evolution, as was noted by Gries (1983a). However, most uplifts in the study area of interest have simply been accepted as "Laramide" age. This section attempts to clarify relative timing of certain events. Event timing discussed in this section is presented graphically in Figure 5.

The Uinta Basin region has been tectonically active since the Devonian (Lemmon and others, 1998). Laramide tectonism dominated the area from late Cretaceous to late Eocene/Oligocene (Johnson, 1992; McPherson and Bredehoeft, 2001) with the most evident movements occurring in the Tertiary.

The Uncompahgre Uplift underwent a period of uplift in late Paleozoic (Johnson, 1992) then again later during the Laramide Orogeny (Narr and Currie, 1982). The San Rafael swell had major movement in latest Cretaceous to early Paleocene time. Uplift of the Uinta and Wasatch Mountain ranges began in late Cretaceous (McPherson and Bredehoeft, 2001), with additional uplift of the Uinta Mountain block occurred in late Paleocene (Fouch et al., 1994) and/or Eocene (Gries, 1983a). During this uplift, the mountains moved up and southward relative to the basin along a steep dipping reverse fault (Narr and Currie, 1982). The Colorado

ERA	PERIOD		EPOCH	Age (Ma)	Related Structural or Tectonic Events
Cenozoic	Quaternary		Holocene	0-0.01	
			Pleistocene	0.01-1.6	
	Tertiary	Neogene	Pliocene	1.6-5.3	
			Miocene	5.3-23.7	
		Paleogene	Oligocene	23.7-36.6	
			Eocene	36.6-57.8	
			Paleocene	57.8-66.4	
Mesozoic	Cretaceous		Late	66.4-144	
			Early		
	Jurassic		Late	144-208	
			Middle		
			Early		
	Triassic		Late	208-251	
			Middle		
			Early		
Paleozoic	Permian			251-286	
	Pennsylvanian			-320	
	Mississippian			-360	
	Devonian			-408	
	Silurian			-438	
	Ordovician			-505	
	Cambrian			-543	

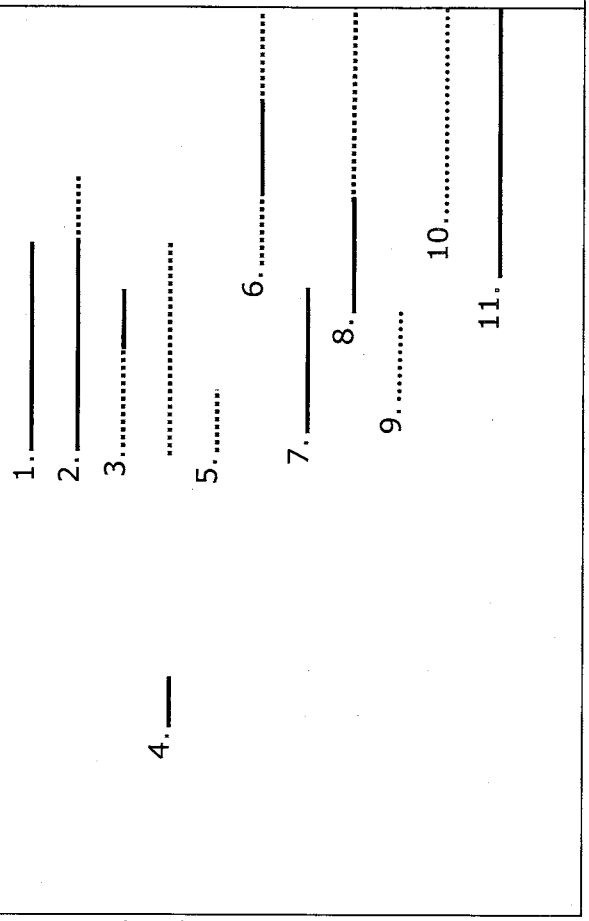

Figure 5: Illustration of related Tertiary structural and tectonic events in the DFZ vicinity: 1. Laramide Orogeny/associated tectonism, 2. Uinta Basin formation, 3. Uinta Mountain uplift, 4. Uncompahgre uplift, 5. San Rafael Swell, 6. uplift of the Colorado Plateau, 7. regional uplift, 8. gilsonite emplacement, 9. formation of the DFZ faults and fractures, 10. anticline(s) in the vicinity of the DFZ, 11. hydrocarbon generation in the Altamont Bluebell field; dotted lines indicate uncertainty.

Plateau underwent as much as 1 km of uplift in late Miocene/Pliocene (Fouch et al., 1994) after deposition in the basin ceased (Groeger, 1997); McPherson (1996) states that this uplift began ~10 Ma and is ongoing today.

Emplacement of the Cenozoic gilsonite dikes has been extensively studied by Verbeek and Grout (1992). The age of these dikes has been determined to be in the range of ~43-10 Ma (Verbeek and Grout, 1992). Relationships between the gilsonite

filling the dikes and the DFZ faults indicate that the DFZ pre-dates the gilsonite. More specifically, faults at the easternmost edge of the DFZ intersect with gilsonite dikes that appear to "bend" into the fault zone (Lemmon and others, 1998; Bereskin, 2001, personal communication; Bruhn, 2001, personal communication).

The state of tectonic stress in the basin is not well understood. This has been discussed in previous reports, including a DOE study (Lemmon and others, 1998). This report and investigation performed an analysis using maximum regional principal stresses of 37.9 MPa in the east-west direction, and 25.4 MPa in the north-south direction. Field evidence used in this determination included the presence and orientation of the DFZ and gilsonite emplacement, which indicates that principal stresses have changed over time.

2.3.2 SPECIFIC to the DFZ

This section examines previous work specific to the DFZ and the remaining uncertainties that served as additional motivation for this study. When investigating fracturing in general, the timing of events in the immediate vicinity is crucial. In the case of the DFZ, this includes (but is not limited to) regional tectonic stresses, deposition of different facies, uplift, removal of overburden, formation of anticlinal features, formation of other fault and/or fracture features, hydrocarbon generation and subsequent overpressuring.

General known timing ranges of deposition, regional uplift, gilsonite emplacement, and regional joint sets are discussed above. Hydrocarbon generation responsible for the overpressures in the North Horn Fm in the Altamont-Bluebell field directly to the north of the DFZ began ~30 Ma in the middle Oligocene (Fouch et al., 1992b). Bredehoeft et al. (1994) predicted that high pressures would increase to approximately 8 km of head within 10,000 years after oil generation began.

Detailed information about the geologic history of the fault zone itself is not readily available. Some of the most recent research done in the DFZ area focused on the Duchesne Graben (Groeger and Bruhn, 2001). However, this study did not specifically address timing of the fractures or the mechanism of fracturing. The DFZ cuts through the Green River, Uinta, and Duchesne River formations. This may indicate that the age is younger than the deposition of the Duchesne River Fm, or Oligocene (Ryder et al., 1976; Fouch et al., 1994). However, these may also be the result of reactivation of older fault features located in the Green River Fm (Fouch et al., 1994; McPherson and Bredehoeft, 2001).

This research focuses on the history of the DFZ including mechanisms involved in fracturing and the timing of fracturing relative to other events in the central Uinta Basin. Specific interest lies in deciphering the role that fluid overpressures may have played in fracturing. The geologic setting, observed confluence of overpressure termination and facies change, history of the basin, and previous work in the Uinta Basin provide a general baseline of data. Based on this, there is reason to suspect that relationships between fractures in the DFZ and fluid overpressures may exist, but have not been proven previously.

McPherson and Bredehoeft (2001), Bredehoeft et al. (1994), and Fouch et al. (1992a) suggest that overpressures developed in the Flagstaff Mbr of the Green River Fm. Overpressures can lead to changes in effective stress and possible fracturing. The rate at which these overpressures may have propagated throughout the system is dependent upon hydraulic diffusivity and permeability of the surrounding rock units.

Another relationship to consider is the temporal relationship between overpressure development and fracture formation, a type of "the chicken or the egg" question. Both could potentially explain the present-day relationship we see between overpressures and fractures. If the pressures formed first, the effective

stress may have been lowered, resulting in subsequent fracturing. On the other hand, if the fractures formed first in response to some other stress (such as local and/or large scale flexure), pressures may have escaped through the fractures rather than building up. The conceptual models that have been developed as a part of this research help investigate this matter.

2.4 FIELDWORK and OBSERVATIONS

2.4.1 MOTIVATION

Fracturing may be considered process- or material-based. Process-based occurrences, such as flexure or overpressuring, may induce additional stresses in a system. Material-based fracturing considers that fracturing may be amplified by differences in rock strength, but still caused by some underlying process. Determining which process or property controls the fracturing is complicated since they are highly coupled. Mechanical strength often depends on physical characteristics such as cementation and framework structure. Brittle failure (rather than ductile deformation) is likely to favor well-cemented rocks. Hydrological properties, such as porosity and permeability, may be strongly coupled with degree of cementation since the amount of fluid which passes through a rock is generally responsible for the cementation. Diffusivity and storativity are of additional interest since they can influence the rate at which a pressure can diffuse from a source area. If pressure cannot dissipate quickly, the possibility of overpressures leading to fractures becomes more likely.

An extensive characterization of rocks from the area is desired for the purpose of investigating the mechanism of fracturing in the DFZ. Knowledge of physical, hydrological, and mechanical properties as well as inherent relationships

that exist among them can be essential. A physical explanation for failure can be determined by analyzing patterns of rock failure. Investigating the general history of flow in the rocks is another point of interest in this project.

This research is largely built on previous field work in the Duchesne Graben area (Groeger 1997; Groeger and Bruhn, 2001). This work emphasized the structure of the graben and included structural measurements (such as strike, dip, and depth to marker beds). Because that research did not characterize the rocks in terms of smaller-scale properties, physical samples from the DFZ area were needed to perform the characterization desired for this study.

2.4.2 SAMPLING STRATEGY

I planned and conducted a field trip including specialists from the University of Utah, Utah Geological Survey, and others to make field observations of the DFZ and Uinta Basin area in general. Samples were collected from in the DFZ, as well as to the north and south. Figure 6 is a map illustrating sample collection sites and a

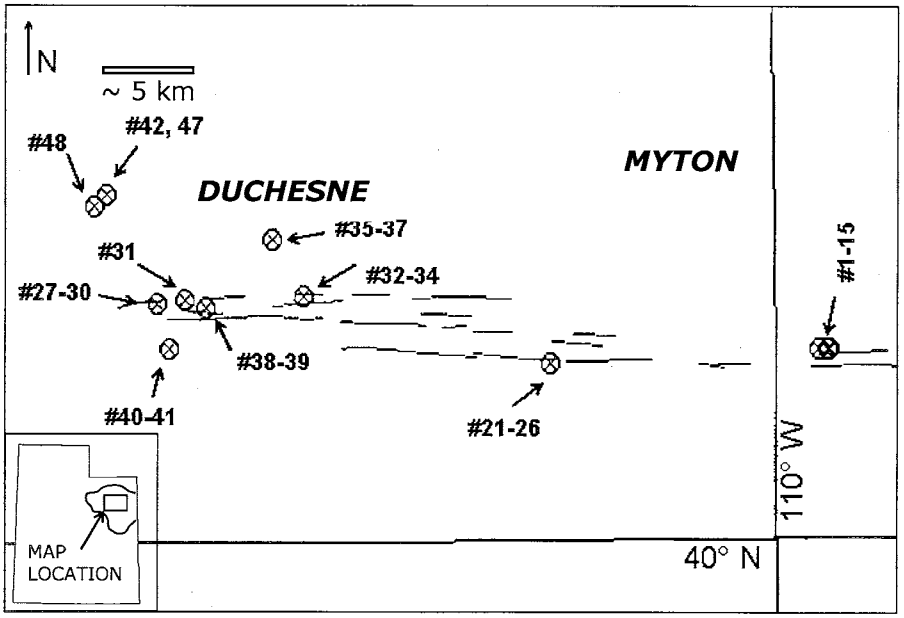

Figure 6: Locations and sample numbers where samples were collected in the DFZ area, marked by Xs; sub-horizontal lines represent major faults; see Table 2 for general location names.

table of location names referred to in the following discussions (Table 2). The sampling strategy was designed to maximize results of a planned rock characterization so that measured parameters could be compared for differences and patterns with respect to vicinity to the DFZ.

Location name	Sample numbers
Balcron Oil Field	1 – 15
Wells Canyon	21 – 26
Duchesne Graben	27 - 30, 31, 32 – 34
North of DFZ near Duchesne	35 – 37
Duchesne Graben/Indian Canyon Rd.	38 – 39
Indian Canyon Rd, south	40 – 41
North of DFZ	42 - 47, 48

Table 2: List of sample numbers and general location names.

2.4.3 OBSERVATIONS

This study is primarily concerned with the Uinta Fm since the fractured rocks of the DFZ occur in surface exposures of this unit. Basic rock property and characterization is needed as a framework for analysis. We are interested in rocks in the immediate vicinity of the fault zone so that any material-based patterns can be established. A large portion of previous stratigraphic and/or lithographic descriptive work done in the Uinta Basin describes the Uinta Fm in broader terms or focuses on the Green River Fm. The probable reason for this focus is that the majority of the hydrocarbon production occurring in the Uinta Basin is sourced and trapped in Green River strata. Such studies include:

- Dane, 1954 (Stratigraphy and facies relationships; Upper Green River and Lower Uinta Fm)
- Ryder et al., 1976 (Early Tertiary sedimentation; focus on North Horn, Wasatch/Colton, and Green River Fm through the middle marker)
- Hood, 1976 (Hydrologic properties of aquifers in the northern Uinta Basin)

- Pitman et al., 1982 (Deposition and diagenesis of reservoir rocks; Douglas Creek Member, Green River Fm)
- Fouch et al., 1992a (Oil and gas accumulations; North Horn, Wasatch/Colton, Green River, and Uinta Fm)
- Morgan et al., 2000 (Reservoir characterization; Middle and Lower Members, Green River Fm)

Although we are most interested in the Uinta Fm, the parameters of the Green River Fm (permeability and diffusivity in particular) are still crucial since this is the presumed source of the overpressures and they may have migrated through these units.

2.4.3.1 *LITHOLOGY: Uinta Formation*

Strata cropping out at the surface in the DFZ vicinity includes the Duchesne River and Uinta Fm, with a more frequent occurrence of the latter. Interbedded sandstone, limestone, and shale represent alluvial and marginal lacustrine environments. Photographs of typical strata present are shown in the figures that follow. South of the DFZ, the open lacustrine Green River Fm is exposed.

A general trend of decreasing grain size from north to south across the fault zone is evident, corresponding to a transition from alluvial to lacustrine facies. This is consistent with regional-scale geologic mapping (Hintze, 1997). Others recognize that the Green River Fm was deposited in an open and/or marginal lacustrine environment, the Uinta Fm in a marginal lacustrine and/or alluvial environment, and the Duchesne River Fm in a mainly alluvial environment. Spatial facies relationships are discussed only in a qualitative manner (Ryder et al., 1976; Fouch et al., 1992a; Verbeek and Grout, 1994) and are not generally mapped or described in detail in previously published research.

Many outcrops of the Uinta Fm in the southwestern part of the DFZ suggest a shallow lake bed depositional environment. The outcrop in Figure 7 consists largely of fine-grained carbonates or micritic mudstone. It also contains a sandstone layer, a significant amount of volcanic debris, and secondary chert (darker gray nodules). Bedding demonstrates a gentle northward-dip. Fractures are oriented nearly vertical and are closely spaced in the micrite (~2-5 cm) but slightly farther apart in the sandstone (~5-10 cm). Two sets were evident; one had a strike of N 80° E and the other N 10° E.

The transition from Uinta to Green River Fm at the surface occurs approximately 20 km south of the DFZ boundary. Traveling south of location #38-39 (see Figure 6 for locations) along Indian Canyon Road, the lithology appears muddier and becomes finer-grained. It is less massive, has thinner bedding planes, and

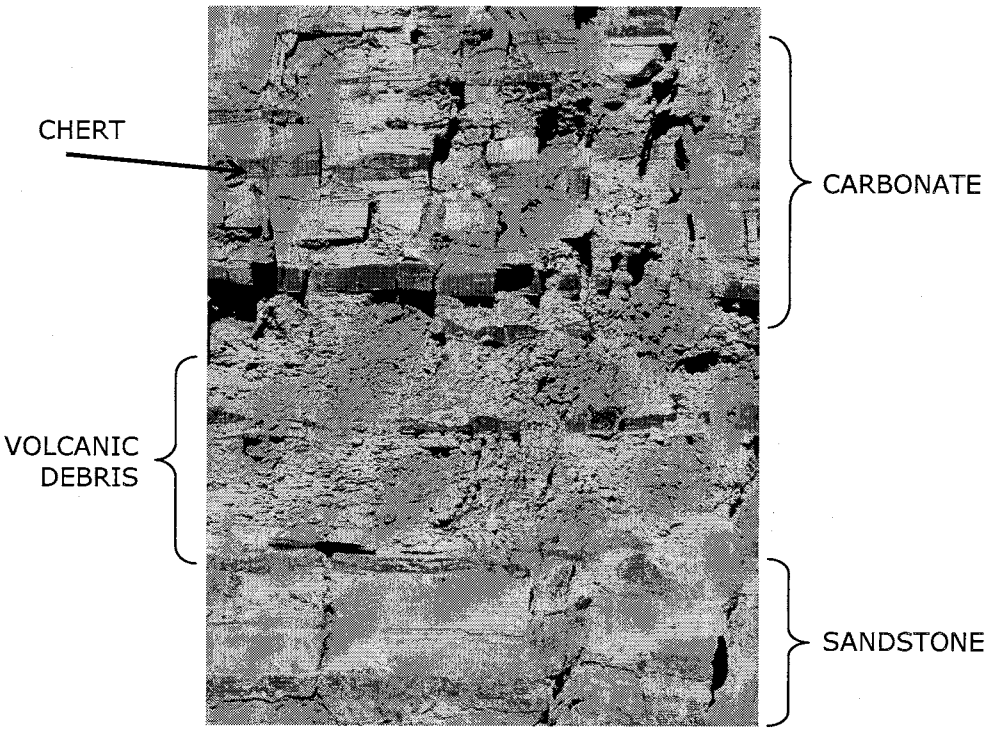

Figure 7: Uinta Fm in the southwestern part of the fault zone; sample location #38-39 on Figure 5 (Duchesne Graben/Indian Canyon Rd.); mechanical pencil for scale.

breaks apart very easily. Samples were collected at location #40-41. South of this site, we were unable to readily collect intact samples large enough for our planned mechanical tests (minimum size of 3 in thick by 5 in wide) because the rocks were too friable.

The Uinta Fm in the southeastern DFZ is similar in character to the southwestern part. Figure 8 illustrates an outcrop which contains layers of fine-grained carbonates and sandstones. Shale layers and a distinct layer of ostracods are also present in this section. This outcrop is highly weathered. Depositional environment was likely to have alternated between an alluvial and marginal lacustrine setting. Fractures are nearly vertical and strike N 80° E. Fracture spacing in the carbonates is typically vertical and dense (~1-5 cm), while fractures in the sandstones are less developed.

North of the DFZ, the Uinta Fm becomes less fine-grained. Interbedded limestones and sandstones are observed at location #35-37 (Figure 9). Bedding has a slight northward dip. These were most likely deposited in a marginal lacustrine

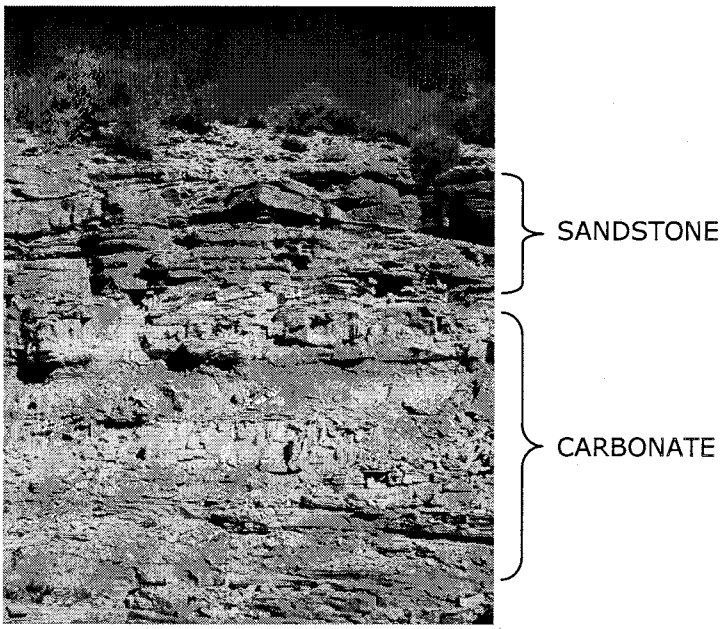

Figure 8: Uinta Fm in the southeastern part of the fault zone; sample location #21-26 on Figure 6 (Wells Canyon); rock hammer for scale (center of photograph).

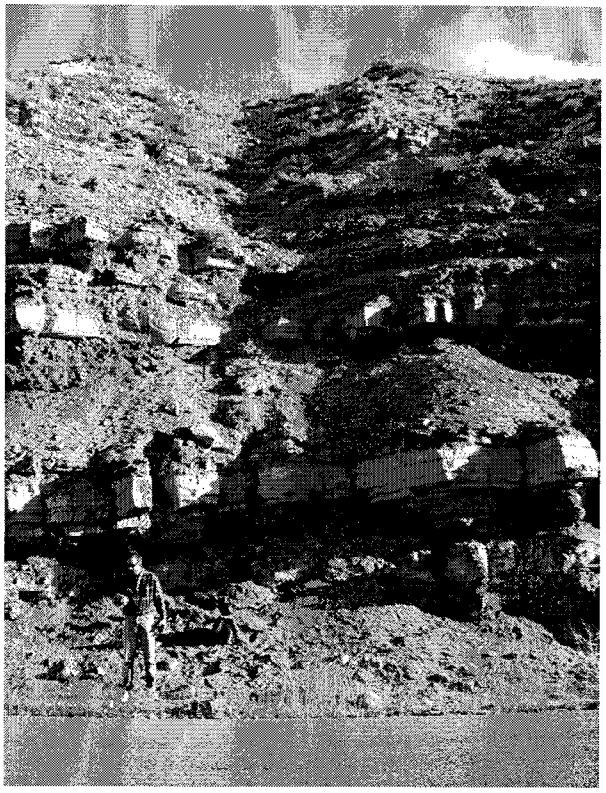

Figure 9: Uinta Fm north of the fault zone; sample location #35-37 on Figure 6 (north of DFZ near Duchesne); person for scale.

and/or alluvial setting. Fractures are oriented nearly vertical. The prominent joint set has a strike oriented approximately north. This outcrop was somewhat unique in its distribution of mineralization; small calcite crystals are found precipitated along both (horizontal) bedding planes and (vertical) fractures. In general, this outcrop exhibits layers that are thinner, sandier, and more weathered than those in the DFZ.

At the approximate boundary between the Uinta and Duchesne River Fm and farther to the north than location #35-37, the lithology is significantly different. Figure 10 illustrates a common coarse-grained alluvial deposit. Individual grain sizes range from millimeters to approximately 1 cm. These grains range in degree of roundness, but are generally sub-rounded to sub-angular. Layers of loosely consolidated deposits dominate the highly weathered outcrop. These layers were easily broken apart with a rock hammer. No fractures are evident.

Figure 10: Uinta/Duchesne River Fm north of the fault zone; sample location #42, 47 on Figure 6 (north of DFZ); marker for scale.

2.4.3.2 *FAULTS*

Many of the faults in the DFZ are large-scale, mappable features. The general character we observed in the field is that of significant offsets on the scale of tens of centimeters to meters; others report displacements ranging from several meters to 30 m in the Balcron area (Lemmon and others, 1998), and up to 200 m across a single fault plane in the Duchesne field (Groeger, 1997). Many of the observations presented in this section were made in the Balcron field. In this area, the DFZ is much more complex than what can be inferred from current mapping (Lemmon and others, 1998). Figure 11 illustrates one of the larger fault features found in the Balcron area. Features such as this are abundant and easily identified in the DFZ area.

A number of the faults include a damaged zone approximately 5-10 cm thick. This fault gouge is often rich in calcite. The source of this calcite is likely to be from water moving along the fault. Previous hydrological modeling determined that the DFZ was an area of a significant amount of flow (McPherson, 1996); see Figure 3. If

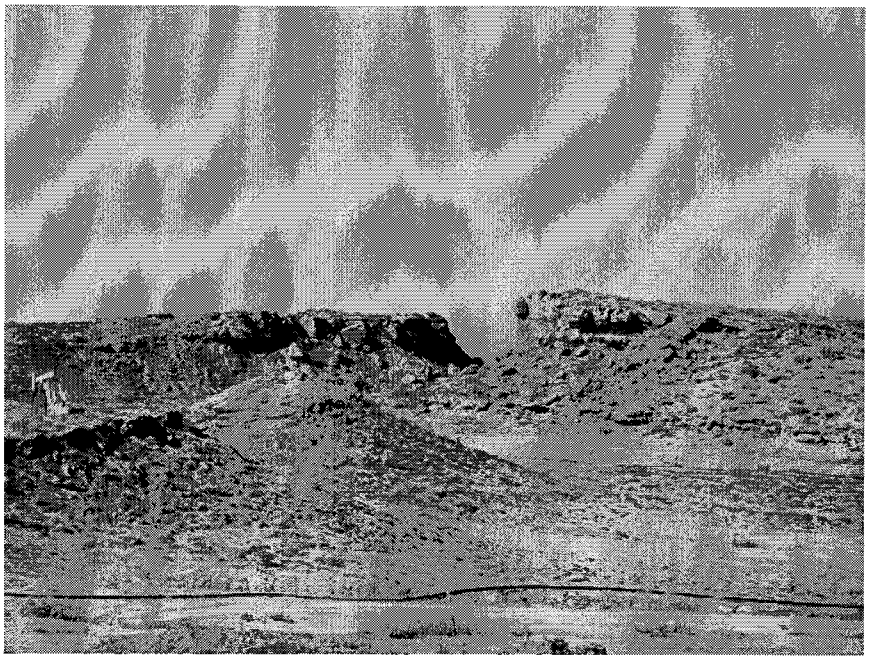

Figure 11: Large fault feature in the Balcron oil field area; Sample location #1-15 on Figure 6; pump jack for scale.

this is the case, one could expect that water flowing through carbonate rocks may acquire $CaCO_3$ in solution. It is reasonable to expect that this could be re-precipitated as calcite in fractures later along the flow path. More detailed hydrological modeling may be able to provide more insight to support this theory.

Distinct slickensides are present on other fault surfaces (Figure 12). Estimated displacement along this fault is approximately 1 m; the fault surface is stained by limonite and is coated with calcite (similar observations were made by Lemmon and others, 1998 in this area). There are instances of faults that show both damaged zones and slickensides along their length within the span of a few meters. A particular outcrop located in the Wells Canyon area illustrates a fault with approximately 3 m of displacement (Figure 13). A thick damaged zone along the fault contains crushed material of the host rock.

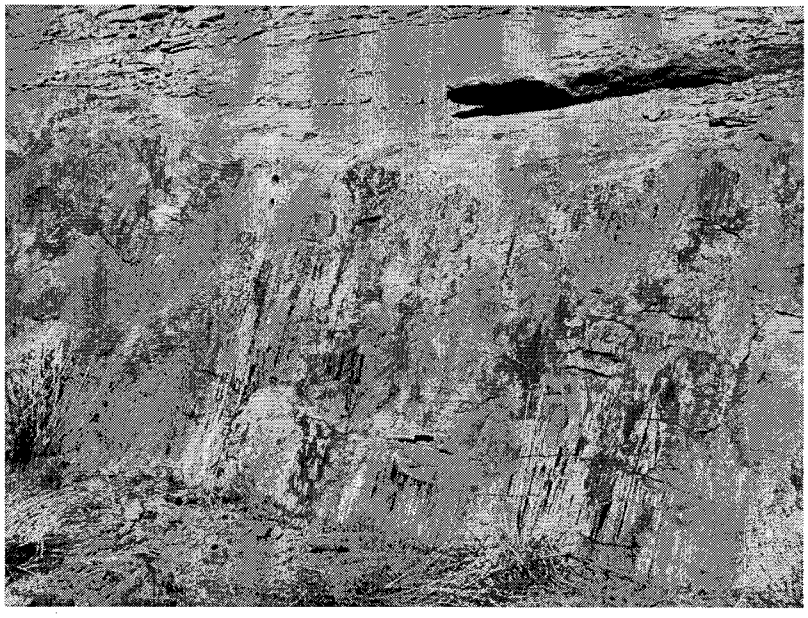

Figure 12: Smaller scale fault feature in the Uinta Fm in the Balcron area showing slickensides, limonite staining, and calcite coating; Sample location #1-15 on Figure 6; marker for scale.

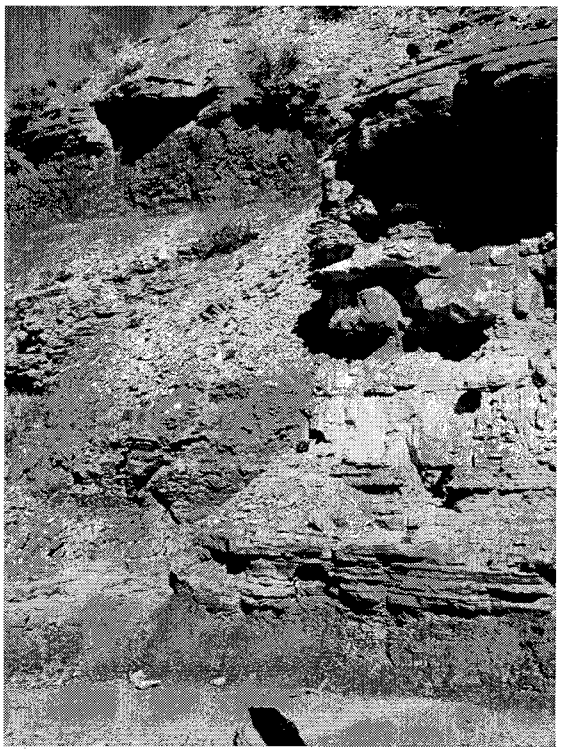

Figure 13: Fault with displacement of approximately 3 m in Wells Canyon; Sample location #21-26 on Figure 6; backpack for scale.

2.4.3.3 *FRACTURES*

Most outcrops in the DFZ area are extensively fractured. The main joint set strikes N 80-90° E and is nearly vertical. Spacing of such joints is normally 20-30 cm; however, the joints are much more dense near the faults (Groeger, 1997). Another less defined joint set strikes approximately N-S. Open fractures exist at depths up to 1,000 m and are commonly spaced 2.5-5 cm apart (Lemmon and others, 1998).

Calcite and gypsum can be found in many of the fractures (Groeger, 1997). Other fractures sets contain no evidence of fluid alteration or precipitation (field evidence; Bruhn, personal communication, 2001). The explanation for this difference is not known for sure, but may include one of the following possibilities: (1) fractures occurred at a time or location where fluids were not available, (2) when fracturing occurred, there was no gradient present to force fluids through the fractures, (3) fluids preferentially flowed through only a percentage of the fractures present, or (4) fluids flowed so rapidly or were of such a small volume that no alteration or mineralization was left on the fracture walls.

To the right of the mound-like features in the middle of Figure 11, distinct calcite-filled fractures are visible at the surface. These veins are 1–2.5 cm thick. They strike N 80° W and are nearly vertical with a dip that varies slightly around 70° S. Calcite was collected at this site with the intention of fluid inclusion analysis.

Fracture patterns in coarser-grained sandstones are markedly different than the near-vertical fractures normal in the finer-grained carbonates. This dependency of fracture character upon lithology was also noted by a DOE Report that stated sandstones in the Ûinta Fm often contain conjugate fractures that dip steeply to the north and south, while fine-grained carbonates that are lower in porosity contain only vertical fractures (Lemmon and others, 1998). A sandstone unit with fracture patterns that developed in proximity to the DFZ is illustrated in Figure 14. These

particular fracture sets are at angles of almost exactly 60° and 120°. Figure 15 illustrates the difference in fracture character between different lithology as well as the variability that can be found in a single outcrop. A set of closely spaced vertical fractures are developed in the carbonate; a less developed set of angled fractures is observed in the sandstone.

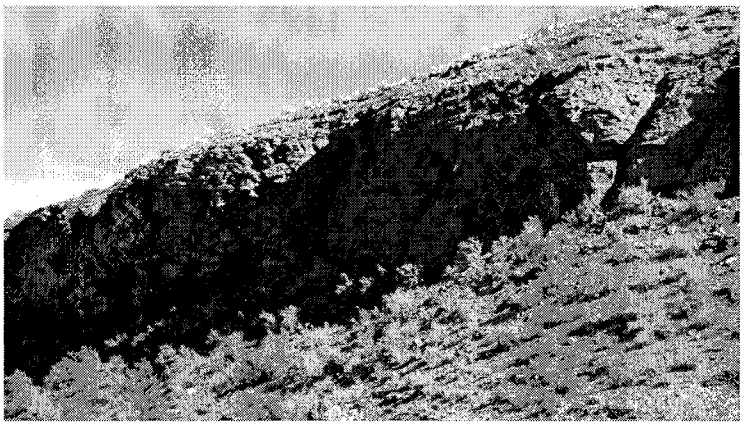

Figure 14: Fractured sandstone unit; Sample location #21-26 on Figure 6 (near Wells Canyon); no scale shown.

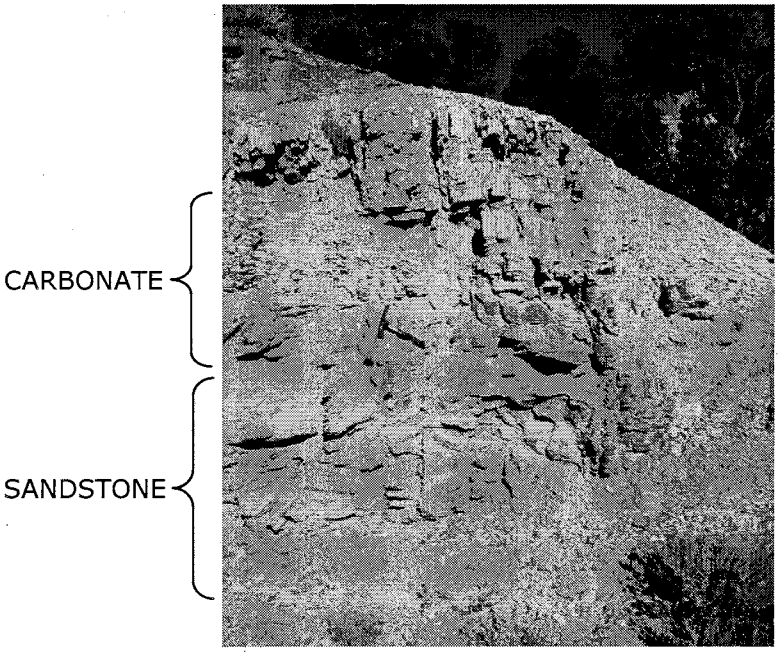

Figure 15: Fractured outcrop in the western fault zone illustrating the difference in fracture character between different lithology; Sample location #31 on Figure 6 (Duchesne Graben); rock hammer for scale.

Regional fracture patterns are an interesting part of the conceptual model development, which will be discussed in the following chapter. Regional stress direction at some point in the history of an area may be inferred based on the orientation of such fracture patterns. Additionally, differences in fracture character between lithology indicate that stress may be expressed in different ways depending on differences in composition and/or rock strength.

2.4.3.4 *GILSONITE*

As discussed in Section 2.1, a series of prominently northwest-trending gilsonite dikes are found directly to the south/southeast of the DFZ (Figure 1). East of the DFZ, these dikes have a general orientation of N 50° W; these same dikes turn into a N 80° W orientation when the faults of the DFZ are encountered (Lemmon and others, 1998). This observation led to the assumption that the DFZ is older than the gilsonite emplacement in the N 50° W orientation. These observations have important implications in terms of overall basin stress regimes throughout the history of the basin. Because of this, they were considered when developing a conceptual model for the DFZ (discussed in Chapter 3).

Minor amounts of gilsonite are observed throughout the Balcron oil field area (also observed by Lemmon and others, 1998). This gilsonite is believed to have formed after calcite diagenesis, and is often found as a "vug filling" that occupies intercrystalline pore space in calcite mineralization (Lemmon and others, 1998).

Traces of gilsonite can be found as far west in the DFZ as the Duchesne Graben. The amount that can be found is rare, and only found in a few places. At the locations sampled, gilsonite and calcite fill the east-west fractures while only gilsonite is found in the north-south trending fractures (Figure 16). This western extent has been previously documented only by Groeger (1997) and mentioned as a possibility by Lemmon and others (1998). In this area, gilsonite can be found as

small solid bubbles or 'blebs' spotted throughout the rocks. Relationships between the calcite and nearby fractures suggest that fractures formed first, followed by calcite, then finally gilsonite. This interpretation is based on the facts that calcite is filling the fractures, and the gilsonite blebs seem to fill void spaces and/or fractures in the calcite. This interpretation seems to be consistent with that of Lemmon and others (1998) for the case of the Balcron area. For the exact location of the Duchesne Graben site in latitude/longitude (shown in Figure 16), upon which this interpretation is based, see Appendix I.

Due to the high viscosity of gilsonite, the possibility that it migrated any significant distance from its source is unlikely. If the source is the same as that of the gilsonite dikes, however, some mechanism of transport must be explained considering the fact that gilsonite is commonly associated with high pressure flows; this will be discussed in more detail in Section 3.2.1.4.

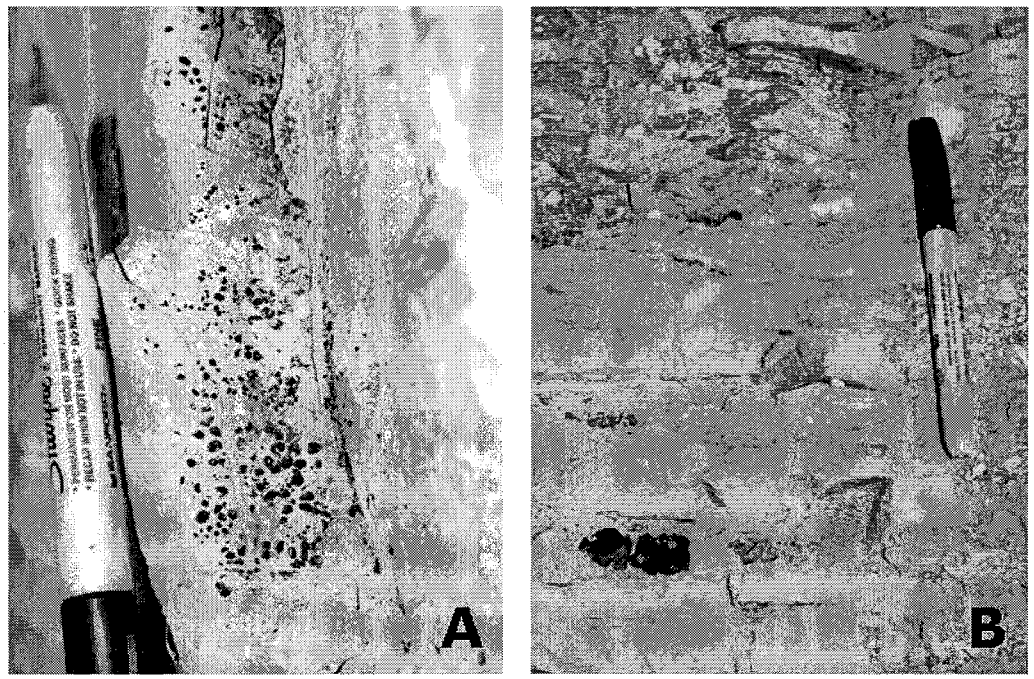

Figure 16: (A) Gilsonite in N-S trending fracture set and (B) gilsonite and calcite in E-W trending fracture set in the vicinity of the Duchesne Graben; Sample location #32-34 on Figure 6; marker for scale.

2.4.3.5 *CONCRETIONS*

In the Balcron area, a number of mound-like structures exist (Figure 17). These mounds are coincident with distinct changes in lithology that occur over a small distance (less than a few meters). Differential weathering of units of different lithology and resistance could result in such a structure, which is likely the case here. The tops of these mounds are covered with sub-spherical concretions that range in size from 10–30 cm in diameter.

The origin of the concretions is not known, but fluid and/or fluid flow is a likely possibility. In some cases, elongated concretions may be used to determine the direction of paleo-groundwater flow (Mozley and Davis, 1996). This kind of determination was not possible for the Balcron concretions, however, since they were not elongated nor were they found in place.

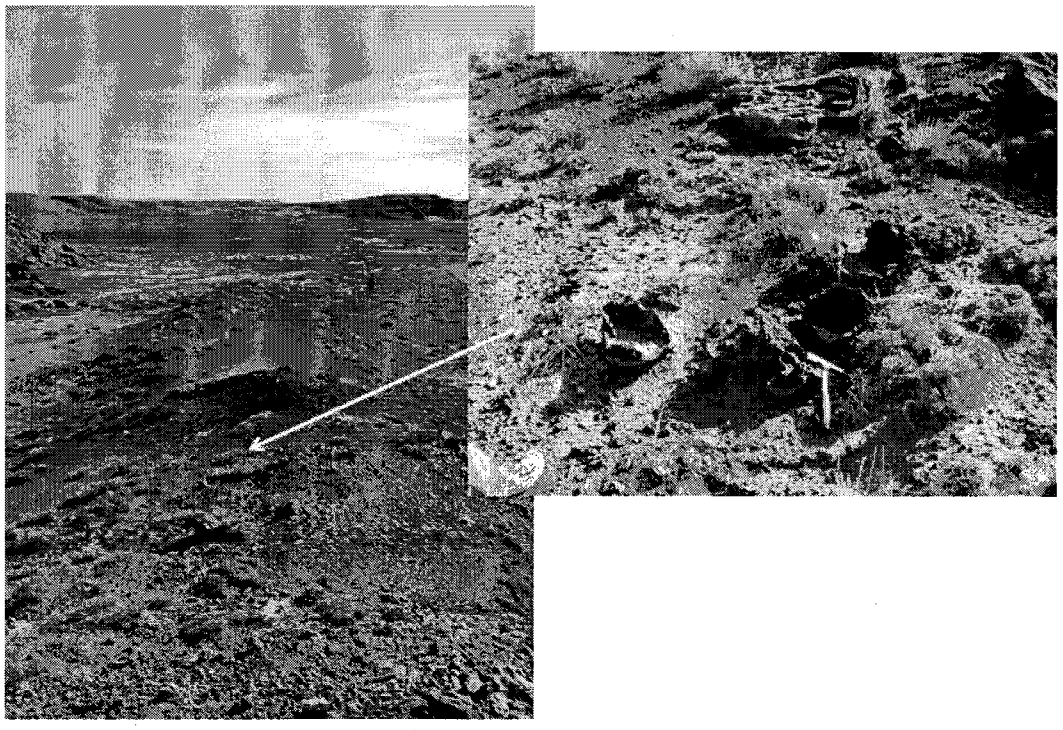

Figure 17: Concretions found on the tops of mounds in the Balcron area; Sample location #1-15 in Figure 6; person (on left) and rock hammer (on right) for scale.

In the conceptual model discussion that follows in Chapter 3, the presence of concretions at the surface support the possibility that fluid may have been forced through the open fractures due to high pressures at depth and a pressure gradient directed upward.

Chapter 3: Conceptual Model

3.1 MOTIVATION for DEVELOPMENT

The exact history of the DFZ is not known nor has it been investigated specifically. Previous researchers in the area offer multiple possible explanations for the fractures that occur in the Uinta Basin: regional tectonic stresses, uplift and erosion, local flexure such as anticlinal noses, preferential fracturing controlled by lithology, and/or hydrocarbon generation with resulting overpressures. Even though the possibility of high fluid pressures lowering effective stress and leading to fracturing is recognized, this process is not often considered because other, more traditional fracturing mechanisms are inferred for the area. Previous explanations do not always consider all of the possible relevant factors. Groeger (1997), for example, noticed that the DFZ coincided with an anticline; since a simple and reasonable option had been discovered, other mechanisms were not considered extensively. No previous studies explain the curious coincidence evident in the field: termination of high fluid pressures at the fault zone boundary, a marked facies change, and subtle local flexure. The currently proposed explanations may in fact be true; however, there may also be more to the story than they suggest.

One of the primary goals of this research project was to develop a conceptual model for the history of the DFZ considering the role that fluid pressures may have played. These developed models were presented as specific hypotheses in Section 1.3. The development offers an explanation for observations in the area, how they may have interacted with one another, and how they may have affected the system

as a whole. This model is presented so that field observations and measured rock properties could be used to support the model.

3.2 EVIDENCE used in DEVELOPMENT

3.2.1 OBSERVATIONS

3.2.1.1 *ANOMALOUS FLUID PRESSURES*

The present day occurrence of high fluid pressures terminates approximately at the northern DFZ boundary. This indicates a probability of some relationship between the two features.

Pressures may have built up beneath the DFZ before the fracturing occurred. If the fractures acted to enhance permeability, pressures may have bled off through the DFZ. This has been suggested in the general case by many, including Ingebritsen and Sanford (1998). However, if the fracturing occurred first, the high pressures probably escaped through the DFZ before they had the chance to build to significant amounts. Another option to consider is the case where the DFZ may have acted as a barrier to flow, preventing pressure from dissipating so that they could increase in the DFZ. A USGS Water Resources Investigation found that the area of the DFZ had a value of transmissivity lower than the surrounding area (Glover, 1996). If this was the case, the pressures may have migrated to the surface through the rock matrix rather than through the fault zone itself. An additional possibility exists in which a fault or fracture could act as both a preferred pathway and a barrier through time. This is likely to occur if the area undergoes a cyclic behavior. These possibilities will be examined in more detail in Section 3.3.

3.2.1.2 *PRECIPITATION in FRACTURES*

The presence of calcite and/or gypsum in many of the fracture sets in the area indicates that an abundance of fluid passed through many of the fractures at some point in history. In certain cases, precipitation in faults or fractures (or in the form of concretions) can be used to infer paleo-flow direction. Mozley et al. (1996) investigated the distribution of calcite cement to infer paleo-flow direction through a fault, and Mozley and Davis (1996) used the orientation of concretions to perform a similar determination. Some of the fractures are filled with up to 1–2.5 cm of calcite. Although in the case of the DFZ we do not have enough data for a quantitative estimation, we believe that this is a reasonable amount of calcite precipitation based on the gradients that must have existed.

3.2.1.3 *DIFFERENCE in FRACTURE FILL / MINERALIZATION*

The fracture sets in the DFZ vicinity differ in fill character: most are filled with calcite, others are filled with gypsum, some do not show any mineralization (discussed in Section 2.4.3.3), and a small minority are filled with or show signs of gilsonite. In the case of a specific site in the Duchesne Graben, fracture sets of different orientation demonstrated obviously different fill (recall Figure 16). Previous work done by Jeff Hulen (Lemmon and others, 1998; Bereskin, 2001, personal communication) made an observation of multiple generations of calcite growth within fractures in the Balcron field area (see Figure 6 for location). Evidence for this interpretation was based on thin sections and petrographic work performed by Hulen and as a minor part of this study. Fluid inclusion analysis performed and reported by Hulen (1998) indicated different temperatures within the different layers of calcite mineralization. The observations from this study are not presented due to lack of a full characterization; thin sections were prepared for fluid inclusion paleo-

temperature and paleo-pressure analysis but were not yet finished upon completion of this research.

These differences imply different conditions that must have been present throughout the history and formation of the DFZ and surrounding area, and must be considered when developing the conceptual model.

3.2.1.4 *GILSONITE*

Gilsonite is a relatively viscous hydrocarbon substance, especially at low temperatures. Table 3 shows the viscosity of gilsonite at different temperatures, along with the viscosity of other common substances for comparison. Gilsonite is commonly - and unofficially - associated with high pressures.

Gilsonite is abundant in the eastern parts of the Uinta Basin. Traces occur frequently in the Balcron area, and can be found as far west as the Duchesne Graben (recall Figure 16). The gilsonite found in the Duchesne Graben is found as smooth, solid bubbles in the void spaces of the calcite (as described by Groeger, 1997); this makes it seem unlikely that it solidified at any significant pressure or depth, and introduces the possibility that it may have formed at the surface. The estimated source beds of the gilsonite are located in the Green River Fm to the northwest of the dikes, and at a depth of 3,800–8,000 ft (1,160–2,440 m) (Verbeek and Grout, 1992). Additionally, we know that the gilsonite dikes must have formed after the DFZ, since gilsonite dikes near the eastern edge of the fault zone commonly turn into an east-west orientation. This is an important point to consider since it provides information about the regional stress regime in the basin, which can control the orientation of fracturing. A critical part of the conceptual model relies heavily on the idea that the regional stresses changed throughout time.

If we assume the gilsonite found in the DFZ is the same, or from the same source, as that composing the large-scale gilsonite dikes in the eastern Uinta Basin,

it is interesting that such a high viscosity substance would be found so far from its presumed source. A migration of this distance suggests the following possibilities:

(1) The gilsonite may have formed as small drops in a brine solution, when then essentially migrated as drops in water. In this case viscosity would not be an issue, since the viscosity of water is relatively low.

(2) A pressure gradient existed that was large enough to force the viscous gilsonite through the fractures. High fluid pressures at depth would have been able to provide such a gradient.

(3) The gilsonite flowed at a significant depth, lowering its viscosity due to the high temperature (see Table 3 for values of viscosity at various temperatures). In the area of interest, the maximum amount of overburden removed is assumed to be 3 km. Consider a depth of 6 km, which is deeper than the maximum depth of the source: at this depth, the temperature is probably 190 °C (according to a surface temperature of 10 °C and a geothermal gradient of 30 °C/km) and thus the viscosity is significantly high and similar to that of a lava flow. Any flow shallower than this would have a higher viscosity, making movement more difficult.

SUBSTANCE	VISCOSITY (Pa•s)
Air, 18 °C (64 °F)	0.000019
Water, 20 °C (68 °F)	0.003
Motor oil, room temperature	1
Gilsonite, 450 °F (232 °C)	2.8
Gilsonite, 425 °F (218 °C)	6.6
Corn syrup, room temperature	8
Gilsonite, 400 °F (204 °C)	22.8
Gilsonite, 375 °F (191 °C)	55
Pahoehoe lava	100 – 1,000
A'a lava	1,000 – 10,000

Table 3: Values of viscosity for gilsonite and other common substances at various temperatures; data from Ziegler Chemical and Mineral Corporation.

3.2.2 Other APPLICABLE CONSIDERATIONS

This section explains some instances of fault behavior and evidence that may remain as a result. Such behavior is expected in the case of the DFZ.

3.2.2.1 *HYDRAULIC FRACTURES*

Extensional rock failure depends on if/when the effective stress acting on the rock exceeds the internal strength of the rock. A specific case is that of *hydraulic fractures*, which occur when the internal pore-fluid pressure, P, exceeds the normal stress across the fracture surface, σ_3 (Figure 18). Empirical evidence suggests that hydraulic fractures can occur in cases where the internal fluid pressure reaches ~1.5 times that of hydrostatic (~100 bars/km), or ~0.6 times that of lithostatic (~250 bars/km) (Ingebritsen and Sanford, 1998). The increase in pore-fluid pressure decreases the effective stress, making the conditions for fracturing more favorable. We know that conditions for hydraulic fracturing are possible in the case of the DFZ.

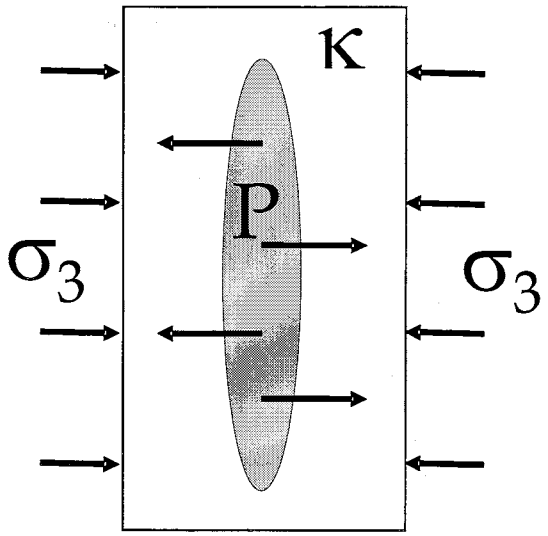

Figure 18: Hydraulic fractures can occur when the pore fluid pressure within a rock (P) exceeds the normal stress across the fracture surface (σ_3); the rate at which the pore-fluid pressure can escape is limited by the permeability or diffusivity (κ).

The concept of hydraulic fractures is often presented and illustrated with the following equation:

$$\sigma_{eff} = \sigma_3 - P$$

where σ_{eff} = effective stress

σ_3 = least principle stress

P = pore-fluid pressure

3.2.2.2 *FAULT VALVE BEHAVIOR*

Fault-valve behavior can result in pressures that oscillate in a predictable fashion, such as that illustrated in Figure 19. In this scenario, fracturing occurs after high pressures have built up. The fracture provides a preferential pathway for pressures to escape, and the result is an immediate drop in pressure. Fluid flow through the fracture results in calcite precipitation. As the calcite begins to effectively narrow the fracture, the rate at which they can diffuse is limited and overpressures develop. At some point in time, the pressure within the fracture may exceed the minimum stress, resulting in a hydraulic fracture. This cycle could repeat a number of times. Research by Sibson (1998) points out the common occurrence of hydraulic extension fractures in sedimentary basins and the possible cyclic nature which may result. This cycle may include hydraulic fracturing, fluid loss through

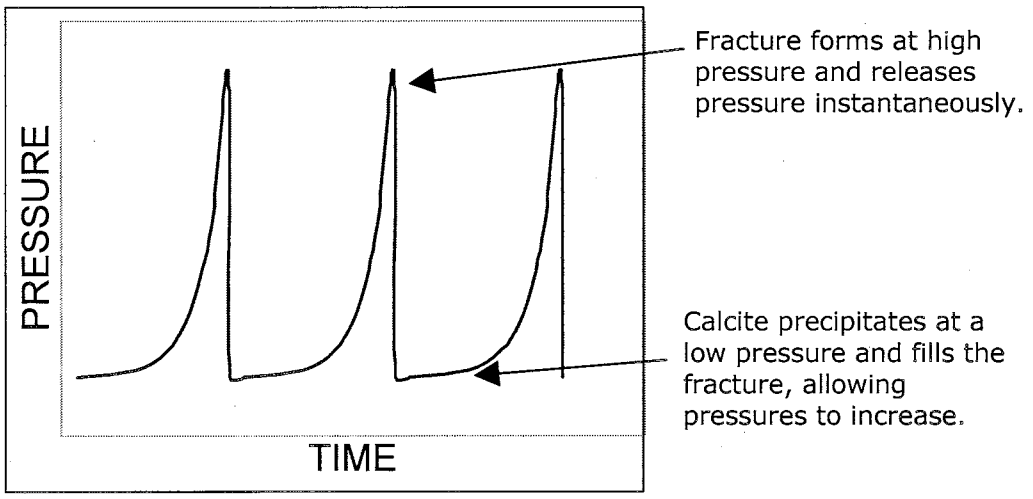

Figure 19: Basic illustration of cyclic fault-valve behavior.

vertical fractures, and a drop in fluid pressure level. He points out that unless the faults heal and regain their cohesive strength, no additional hydraulic fracturing is possible. Other work by Sibson (1996) addresses fault-valve action along suprahydrostatic gradients. The breaching of fluid compartments and resulting structural permeability leads to episodes of fluid migration and is important to fluid flow and redistribution.

Characteristic decay time, or pressure length calculations were made for the DFZ. This is some approximation of how long it might take for fluid overpressures to develop once fracturing and pressure dissipation occurs. The results represent the time required for a pressure pulse to propagate some distance, d. In this case, we are interested in the time for a pressure pulse to propagate from the overpressure source (Flagstaff Mbr) to the fractured units (Uinta/Duchesne River Fm), or 2,800 m. The hydrologic parameters used in these calculations are listed in Table 4 (data from

	Uinta/Duchesne River Fm	Green River Fm
Hydraulic Conductivity, K (m/s)	5×10^{-6} (Hood, 1976)	5×10^{-11} (Morgan et al., 2000)
Permeability, k (m^2)	5×10^{-13} (Hood, 1976)	5×10^{-18} (Morgan et al., 2000)
Matrix compressibility (m^2/N)	1×10^{-8} (McPherson and Garven, 1999)	1×10^{-8} (McPherson and Garven, 1999)
Porosity, n (no units)	0.15	0.10
Specific Storage, S_s (m^{-1}), calculated	9.9×10^{-5}	9.9×10^{-5}
Diffusivity, κ (m^2/s), calculated from K/S_s	5×10^{-2}	5×10^{-7}

Table 4: Parameters used in calculation of characteristic decay time.
used due to the fact that diffusion is often controlled by the most resistant layer.

Hood, 1976; Morgan et al., 2000). The value of hydraulic conductivity (K) used is lower than the mean but higher than the minimum measured value; this value was The resulting time is on the order of 400,000 years. Sensitivity to changes in hydrologic parameters was explored by varying K and n of each unit as a whole. Resulting time lengths varied drastically from ~1,000 years to 4 million years. This emphasizes the dependency of fluid pressure behavior and/or migration on the diffusivity capabilities of the surrounding material.

3.2.2.3 *CRACK-SEAL RELATIONSHIPS*

Crack-seal relationships may be expected in the vein precipitation if fault valve behavior is occurring in the fractures. Such relationships are usually visible in properly-oriented thin sections of the complete fracture (including both walls and the fracture fill). Individual generations of mineral growth may differ in chemical makeup, fiber, crystallographic orientation, color, etc. This was the conclusion arrived at by Hulen (1998). In the case of the samples collected in this study, samples of fracture fill were collected. However, sufficient caution was not taken during collection, and the walls of the fracture were not included.

An additional method of differentiating multiple generations of mineralization within a single fracture is fluid inclusion analysis, which can provide information on the temperature and/or pressure of individual or groups of calcite crystals. Different generations may have experienced different paleo-conditions in terms of pressures and/or temperature. Hulen's work (1998) confirmed multiple generations of paleo-temperature in the case of fracture fill collected in the Balcron field area. Meaningful results depend in part on whether a sufficient number of suitable inclusions exist.

3.2.2.4 *DISSOLUTION by CARBOXYLIC ACID*

Carboxylic acid may be formed as a byproduct of hydrocarbon generation. This happens because alteration of organic material raises the partial pressure of CO_2. Such acid has the ability to dissolve calcite and enhance secondary porosity in beds that have already been cemented by calcite (Schmidt and McDonald, 1979).

3.3 POSSIBLE SCENARIOS

3.3.1 CM#1: HIGH FLUID PRESSURES / "FAULT VALVE" MODEL

This conceptual model considers the case in which high fluid pressures were not only present, but also played a crucial role in the development of the DFZ and associated fractures. Given that the fractures coincide with the extent of the anticline, the most likely mechanism is the stress induced by the anticline aided by the high fluid pressures, and perhaps also aided by regional extension and/or unloading. This model is illustrated in Figure 20. The following discussion pertains directly to this figure, and is numbered accordingly.

FRACTURING MECHANISM: High fluid pressures lowered effective stress, making it easier to fracture due to local flexure.

1. HYDROCARBON GENERATION: Oil and gas generation occurs at depth in the Green River and/or Wasatch Fm in the area beneath the present-day location of the DFZ (Fouch et al., 1992a). There is an associated volume increase with the conversion from kerogen to hydrocarbon; Neuzil (1995) suggested this forcing is on the order of 10^{-14} s^{-1}. Buoyancy of the hydrocarbons alone would provide an upward gradient.

2. OVERPRESSURES: The Green River Fm above the area of hydrocarbon generation has a very low permeability (k). Morgan et al. (2000) reported values

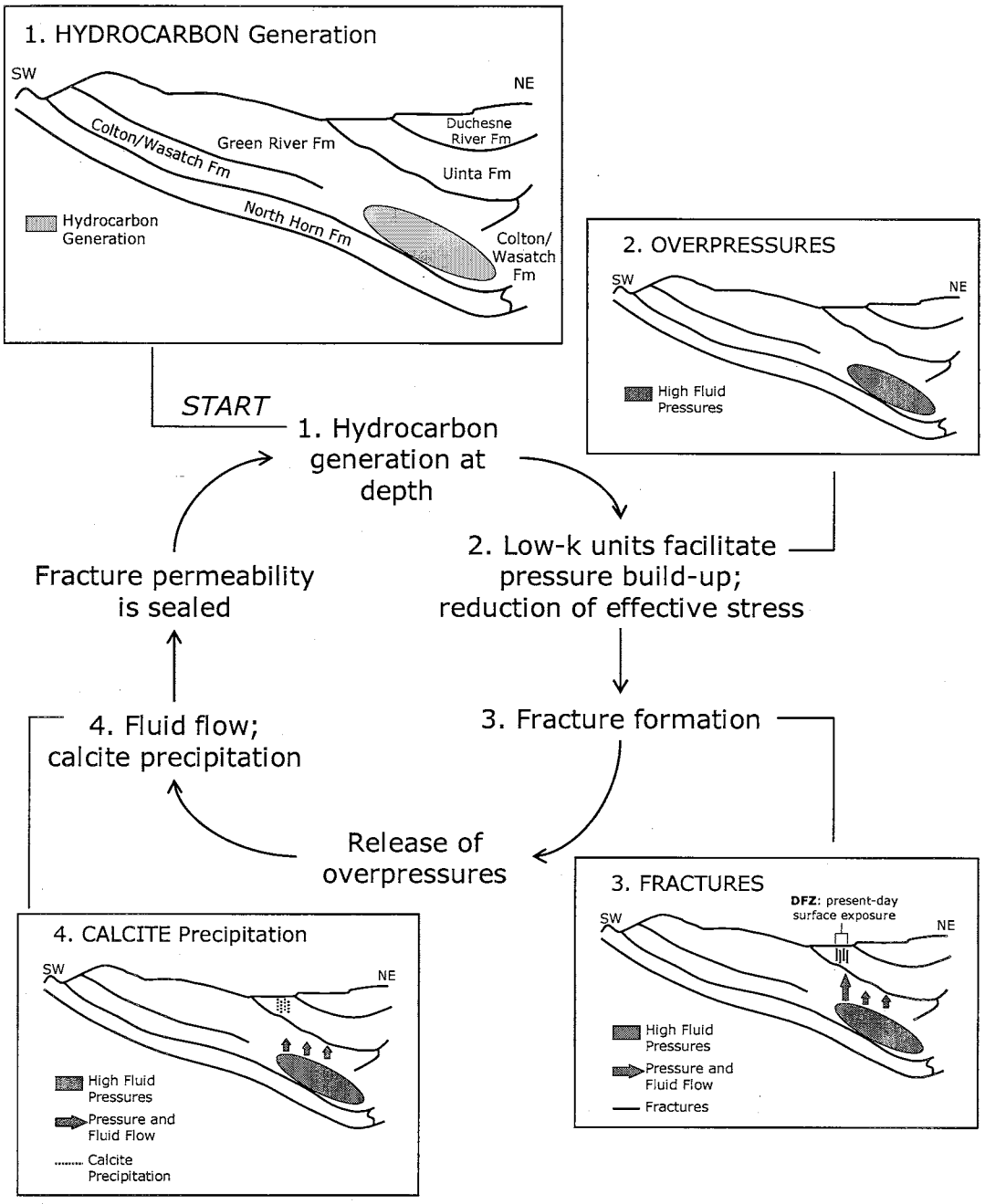

Figure 20: Conceptual model CM#1 illustrating high fluid pressures / fault valve behavior; see text for a detailed explanation of related events.

that ranged from 0.001 to 10 mD (10^{-18} to 10^{-14} m^2) in the lower Green River Fm. This low permeability acts to slow the upward escape of hydrocarbons given the case in which the rate of hydrocarbon generation and subsequent overpressuring is greater than the maximum rate of escape, as controlled by the permeability. Ingebritsen and Sanford (1998) documented various forms of geologic forcing and their magnitudes, including petroleum generation, compaction in a subsiding basin, and smectite dewatering. According to these values and using permeability values from Morgan et al. (2000), rough calculations suggest that significant effects on the fluid-pressure regime would be expected in the Green River Fm and are also possible in the Uinta Fm to a lesser degree. Such processes are likely to result in anomalous fluid pressures within the pores of a rock unit.

If hydrocarbon generation continues at a rate greater than that of pressure escape, the difference between expected (normal) and actual (anomalously high) fluid pressure will increase over time. This results in a change in the stress regime over time, one of the reasons that we are interested in such a process.

3. FRACTURES: Fluid pressures reach some critical magnitude and the least principle stress is exceeded, resulting in fracture. The increased fluid pressures make it possible for these units to fracture under conditions in which it would otherwise not fracture. In other words, without these fluid pressures, the rocks would not have fractured under the regional stress regime alone. The orientation of the fracture set depends on the orientation of the regional stresses. The fractures provide an "escape route" for the high fluid pressures, which decrease temporarily. The preference for location was most likely influenced by the subtle anticline at the surface.

4. CALCITE PRECIPITATION: Initially after the fractures form, groundwater from depth is driven upward by the pressure gradient. Preferential flow channels are created for the fluids through the fractures and increased fracture permeability.

Calcite and, in some cases, gypsum is precipitated in the fractures; calcite solubility depends on the partial pressure of CO_2 and temperature changes.

As calcite seals the fracture and reduces corresponding fracture permeability, the fluid pressures below increase again since they can no longer dissipate quickly. This assumes that hydrocarbon generation is ongoing and provides a source of overpressure. McPherson and Bredehoeft (2001) concluded that overpressure generation is ongoing today.

Given sufficient time, this pressure buildup could result in reopening the previous fracture set, along with another generation of calcite precipitation as groundwater flows through the fractures. If the regional stress regime has rotated, another fracture set with a different orientation may be the result. This cycle of fracturing and precipitation may have repeated multiple times throughout the history of the DFZ.

3.3.2 CM#2: EXTENSION–ANTICLINE model

This conceptual model examines the possibility of how the DFZ fractures may have formed in the presence of, but without the aid of, high fluid pressures. Given the coincidence of the fractures and the anticline, the most likely mechanism is the stress induced by the anticline and perhaps aided by regional extension and/or unloading. This model is illustrated in Figure 21.

FRACTURING MECHANISM:
Local flexure.

1. HYDROCARBON GENERATION, as in CM#1 above.

2. OVERPRESSURES, similar to CM#1 above: The difference here is that overpressures may or may not have built up rapidly; the rate of hydrocarbon generation and the permeability of the surrounding unit are not as crucial. In addition, the fluid pressures did not reach the magnitude that they must in

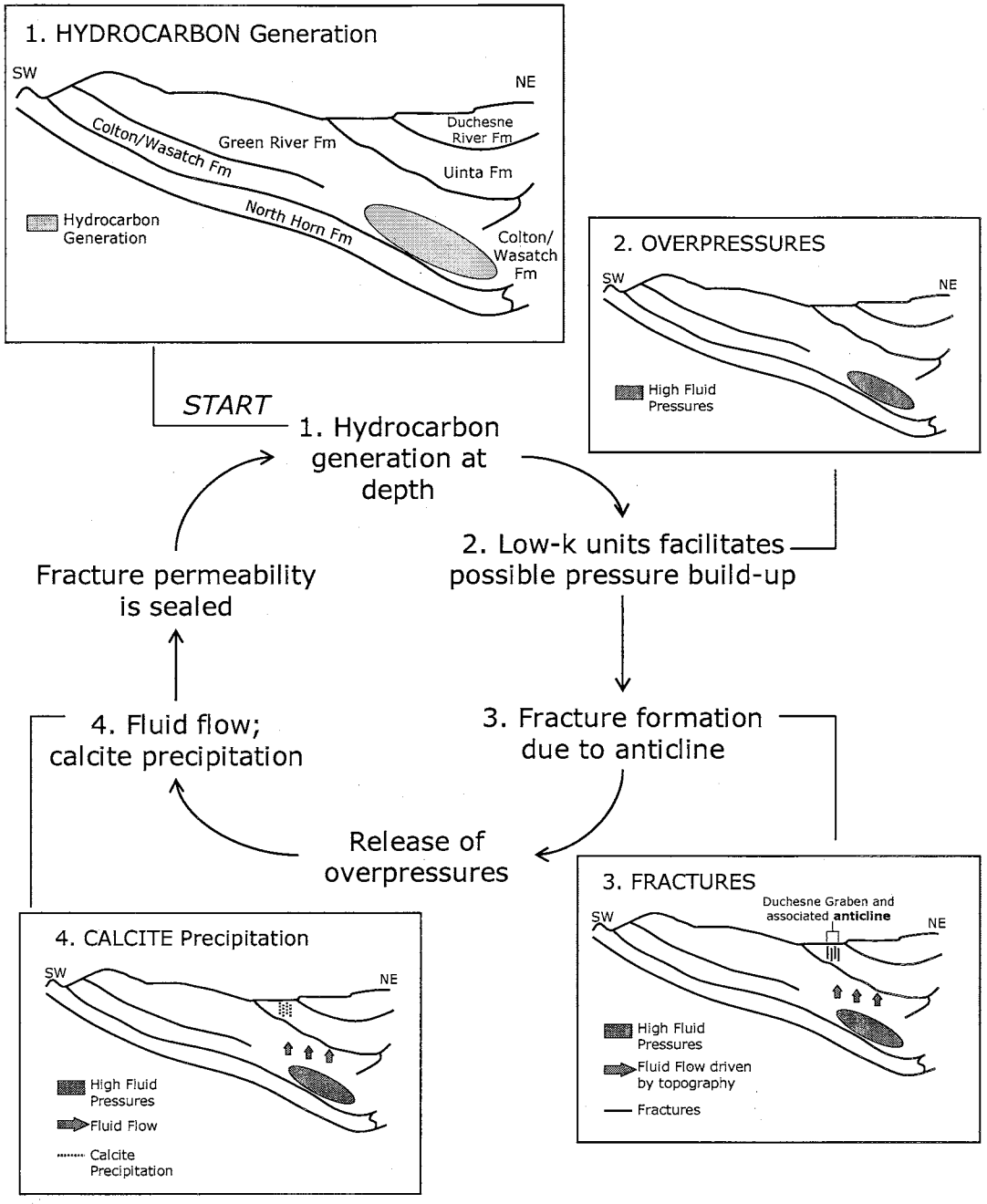

Figure 21: Conceptual model CM#2 illustrating fracture formation due to extension and/or anticline; see text for a detailed explanation of related events.

CM#1 based on the fact that the least principle stress is not exceeded in this case. However, we know that they did increase to some extent since an area of high fluid pressures is observed north of the DFZ.

3. FRACTURES: Local flexure causes the rocks in the DFZ to fracture. Topographically driven groundwater flows through the fractures while they are open. An additional driving force may be provided by the fluid pressures at depth, but it is not necessary. This flow also allows for pressure escape.

4. CALCITE PRECIPITATION: Calcite and/or gypsum are precipitated in the fractures; calcite solubility depends on the partial pressure of CO_2 and temperature changes.

3.3.3 CM#3: FRACTURES BEFORE HIGH FLUID PRESSURES

This conceptual model examines the possibility of how the DFZ fractures could have formed in the complete absence of high fluid pressures. It also examines the present-day relationship that exists between the DFZ and the pocket of anomalous overpressures. This model is illustrated in Figure 22. CM#2 and CM#3 are very similar; the significant difference is the timing of the fractures relative to the fluid pressure buildup.

FRACTURING MECHANISM: Local flexure, regional extension and/or unloading; perhaps amplified by changes in lithology.

1. FRACTURES: Fractures form in response to local flexure, regional extension, and/or unloading. The location of fracturing is dependent upon the location of the local flexure itself, and may also be amplified by changes in lithology in the region.

2. HYDROCARBON GENERATION, as in CM#1 above.

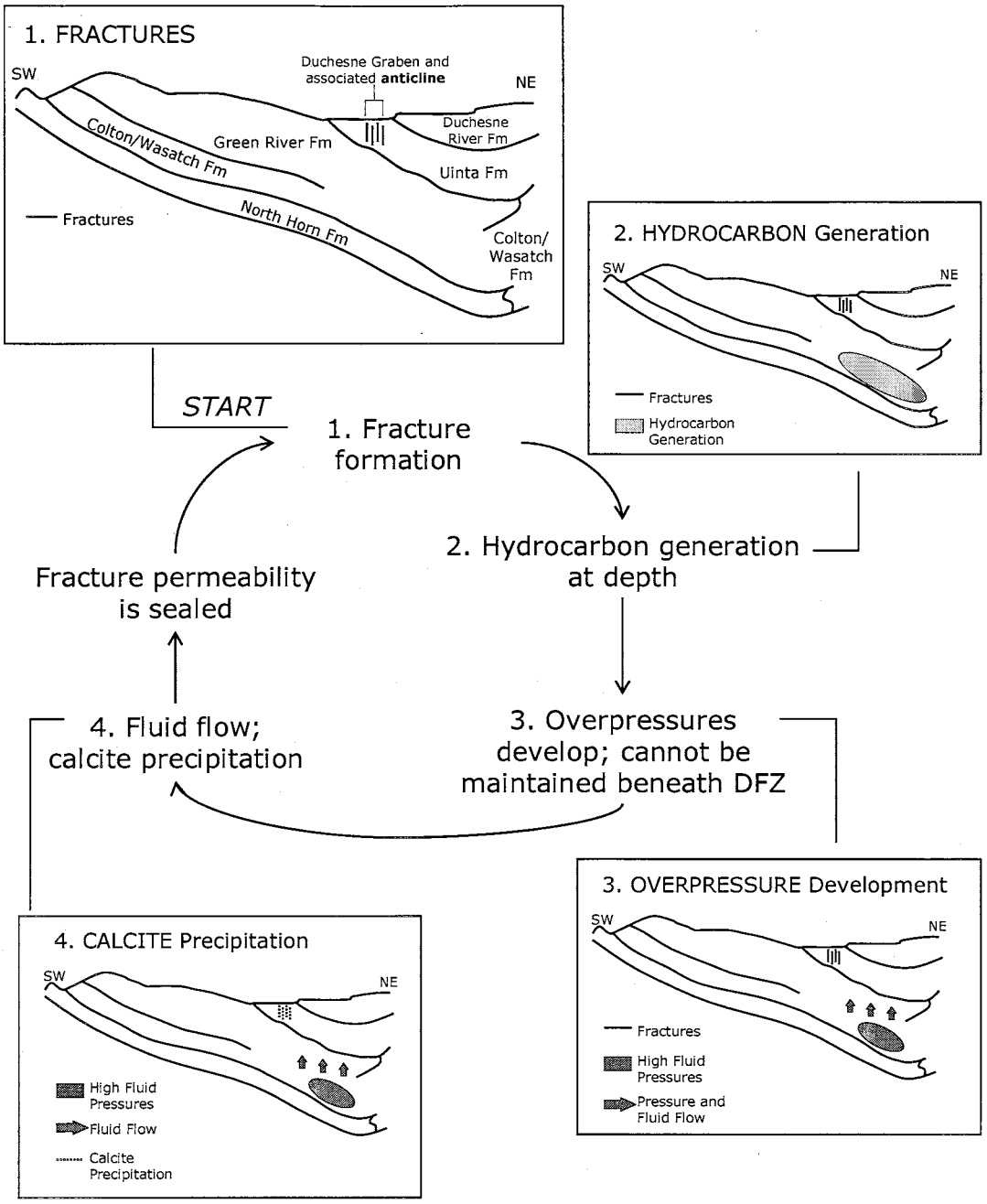

Figure 22: Conceptual model CM#3 illustrating fracture formation unrelated to high fluid pressures; see text for a detailed explanation of related events.

3. OVERPRESSURE DEVELOPMENT: The hydrocarbon generation at depth leads to the generation of high fluid pressures. These fluid pressures cannot be maintained in the area beneath the DFZ since they can escape through the fractures with enhanced permeability.

4. CALCITE PRECIPITATION: Groundwater from depth flows upward. Calcite and/or gypsum are precipitated in the fractures; calcite solubility depends on the partial pressure of CO_2 and temperature changes.

3.3.4 Some ALTERNATIVE COMBINATION

The fractures underwent some cycle of fracturing, calcite precipitation, and re-fracturing. This model considers the endless permutations of the above fracturing mechanisms occurring in these different cycles.

3.4 SUMMARY: Conceptual Model

The most realistic scenario appears to be the case where high fluid pressures were crucial, as discussed in CM#1. This is because it allows for explanation of the observations made in the DFZ through laboratory and field investigations. High fluid pressures seem to provide the best mechanism for multiple fracturing episodes. In addition, the other possible scenarios seem to lack a complete explanation. Further evidence to support this conceptual model will be presented and discussed in the following chapters. Chapter 4 presents measured data, and Chapter 5 provides an interpretation of the observations and data in the context of the presented conceptual model.

Chapter 4: Rock Characterization

The main goal of the laboratory work was to characterize the collected rock samples as completely as possible within the scope of this project. Physical, hydrological, and mechanical strength properties were evaluated. After collecting the data, trends that exist geographically and/or between strength and other properties were examined and analyzed.

The majority of the samples tested in the lab were those collected on the field trip to the Uinta Basin and DFZ from surface outcrops, and are referred to as UB (Uinta Basin) collected samples #1-41. A detailed map of sample locations is provided in Figure 6. Some tests were also run on samples from core donated to this study by Amoco. These cores are from two separate locations located to the northeast and northwest of the DFZ and are from depths ranging from 4,645-11,055 feet (1,415-3,370 m). All of the samples from the Amoco core are marked by a sample name beginning with "A_" followed by the depth in feet. A summary of all samples tested is listed in Appendix I. Graph notation in this section generally adheres to the following: UB collected samples (solid symbols), UB samples north of the DFZ (diamonds), in the DFZ (triangles) south of the DFZ (squares), Amoco samples (hollow symbols), Amoco samples northwest of the DFZ (diamonds), Amoco samples northeast of the DFZ (squares).

In the discussion that follows, only relevant sample results are presented. Method overviews are provided. For detailed method descriptions for most of the laboratory procedures used, see Appendix II.

4.1 HYDROLOGICAL

4.1.1 POROSITY

Method Overview:

Porosity of the Uinta Basin samples was initially analyzed by two different methods as a check for accuracy and consistency: stereopycnometer (Quantachrome Instruments, model SPY-3) and the 'manual' method. The manual method refers to using volume, saturated weight, and dry weight to calculate pore space, or porosity, in the sample. After determination that both methods were reliable, and since regular-shaped samples for measurement were not available in all cases (the stereopycnometer has the flexibility to measure porosity of any shape of sample), the stereopycnometer was used to measure porosity of all samples. In the following cases where only one value is reported, the method used was the stereopycnometer. For method details, see Appendix II.

Results:

A comparison of the stereopycnometer and manual methods was made (Figure 23). Results obtained from the two separate calculations did not yield significantly different results. Replicate samples were tested for a number of samples and can be identified by the same number (different letter). Measured values of porosity are shown in Table 5.

A simple statistical analysis was performed for the porosity measurements. The results of the statistical analysis for porosity measurements are given in Table 6. For *all samples* (N=48), the range is 0.6-12.4, the mean is 5.4, and the standard deviation is 3.9 (all values given in %). For *UB samples* only (N=21), the range is 0.6-10.9, the mean is 6.0, and the standard deviation is 3.4; *UB samples north of*

SAMPLE	POROSITY (stereopyc)	(manual)
48A	9.67%	7.59%
31B	10.48%	10.09%
33A	2.38%	2.33%
35B	10.86%	10.23%
39A	5.34%	5.13%
21A	8.48%	10.06%
22D	3.45%	3.92%
23	9.35%	11.30%
24B	1.62%	1.99%
26B	7.00%	7.05%
27A	5.66%	5.40%
41B	9.21%	9.24%

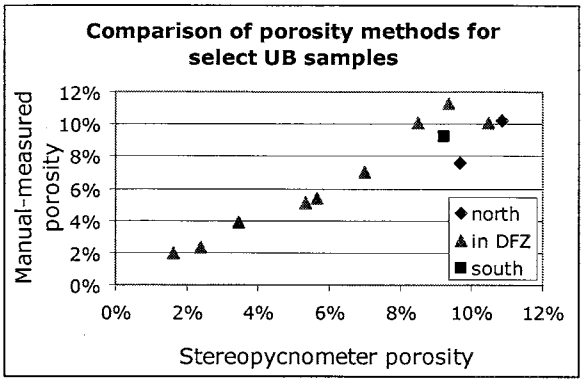

Figure 23: Data and corresponding graph illustrating porosity results from the stereopycnometer and manual methods; *all are UB collected samples*; points falling along a 45° line in the graph on the right correspond to samples in which porosity measured by both methods was exactly the same.

the DFZ (N=3) have a range of 6.4-10.9, a mean of 9.0, and a standard deviation of 2.3; *UB samples in the DFZ* (N=16) have a range of 0.6-10.5, a mean of 5.0, and a standard deviation of 3.1; *UB samples south of the DFZ* (N=2) have a range of 9.2-10.6, a mean of 9.9, and a standard deviation of 1.0. *Amoco samples* (N=27) have a range of 1.0-12.4, a mean of 4.9, and a standard deviation of 4.2. There is a statistical difference between the porosity of UB samples in the DFZ and those north and south of the DFZ based on an ANOVA test (P-value of 0.022).

Figure 24 plots porosity versus location with respect to the DFZ. It should be noted that not all samples shown are from the same depth; recall that the Amoco samples range from 4,645-11,055 feet and the UB samples were collected from surface outcrops. No trends are evident, even if only UB samples are considered.

Relationships between porosity and depth are investigated in Figure 25. This graph illustrates a very general trend of decreasing porosity with depth. This is to be expected due to compaction effects associated with increasing depth and overburden weight. The likely reason this trend is not stronger is due to sample heterogeneity.

SAMPLE	POROSITY	Avg POROSITY	LOCATION
35B	10.86%		north of DFZ
37-1	6.42%		north of DFZ
48A	9.67%		north of DFZ
12	6.89%		in FZ: Balcron
14	4.18%	4.68%	in FZ: Balcron
14A	5.19%		in FZ: Balcron
15-3	6.62%		in FZ: Balcron
21A	8.48%		in FZ: Wells Canyon
22D	3.45%		in FZ: Wells Canyon
23	9.35%		in FZ: Wells Canyon
24	1.26%	1.44%	in FZ: Wells Canyon
24B	1.62%		in FZ: Wells Canyon
25A	1.16%		in FZ: Wells Canyon
26B	7.00%		in FZ: Wells Canyon
27A	5.66%		in FZ: Graben
28	0.57%		in FZ: Graben
31B	10.48%		in FZ: Graben
33A	2.38%		in FZ: Graben
39A	5.34%		in FZ: south
40B	10.63%	9.92%	south of DFZ
41B	9.21%		south of DFZ
A_4645A	11.70%	11.93%	northeast of DFZ
A_4645B	11.70%		northeast of DFZ
A_4645C	12.38%		northeast of DFZ
A_4672A	1.16%	1.07%	northeast of DFZ
A_4672B	0.98%		northeast of DFZ
A_4712A	1.10%	1.65%	northeast of DFZ
A_4712B	2.28%		northeast of DFZ
A_4712C	2.10%		northeast of DFZ
A_4712D	2.14%		northeast of DFZ
A_4712E	1.19%		northeast of DFZ
A_4712F	1.10%		northeast of DFZ
A_4743A	11.43%	11.79%	northeast of DFZ
A_4743B	12.16%		northeast of DFZ
A_4774A	2.70%	1.99%	northeast of DFZ
A_4774B	1.98%		northeast of DFZ
A_4774C	1.30%		northeast of DFZ
A_5320A	7.48%	8.60%	northeast of DFZ
A_5320B	8.89%		northeast of DFZ
A_5320C	9.44%		northeast of DFZ
A_8569	4.04%		northwest of DFZ
A_8602	2.40%		northwest of DFZ
A_10157	3.13%		northwest of DFZ
A_10168	2.51%		northwest of DFZ
A_10171A	2.66%		northwest of DFZ
A_10176A	2.53%		northwest of DFZ
A_11030	2.43%		northwest of DFZ
A_11055	9.10%		northwest of DFZ

Table 5: Values of porosity and average porosity (where applicable) for the UB collected and Amoco samples; values from stereopycnometer measurements.

	All Samples	*UB Samples*	*North of DFZ*	*In DFZ*	*South of DFZ*	*Amoco Samples*
N	48	21	3	16	2	27
Minimum	0.6	0.6	6.4	0.6	9.2	1.0
Maximum	12.4	10.9	10.9	10.5	10.6	12.4
Mean	5.4	6.0	9.0	5.0	9.9	4.9
Median	4.1	6.4	9.7	5.3	9.9	2.5
Standard Deviation	3.9	3.4	2.3	3.1	1.0	4.2

Table 6: Statistical analysis of measured porosity data; all values are given as percentages; N is the number of samples.

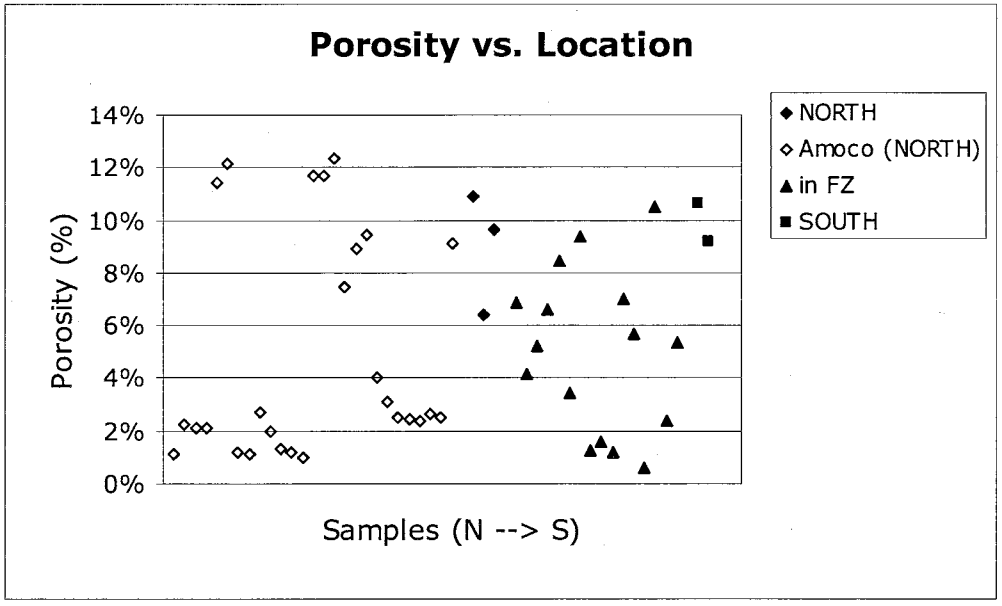

Figure 24: Porosity as a function of location with respect to the DFZ; *note*: UB samples were collected from surface outcrops and Amoco samples ranged from 4,645-11,055 feet.

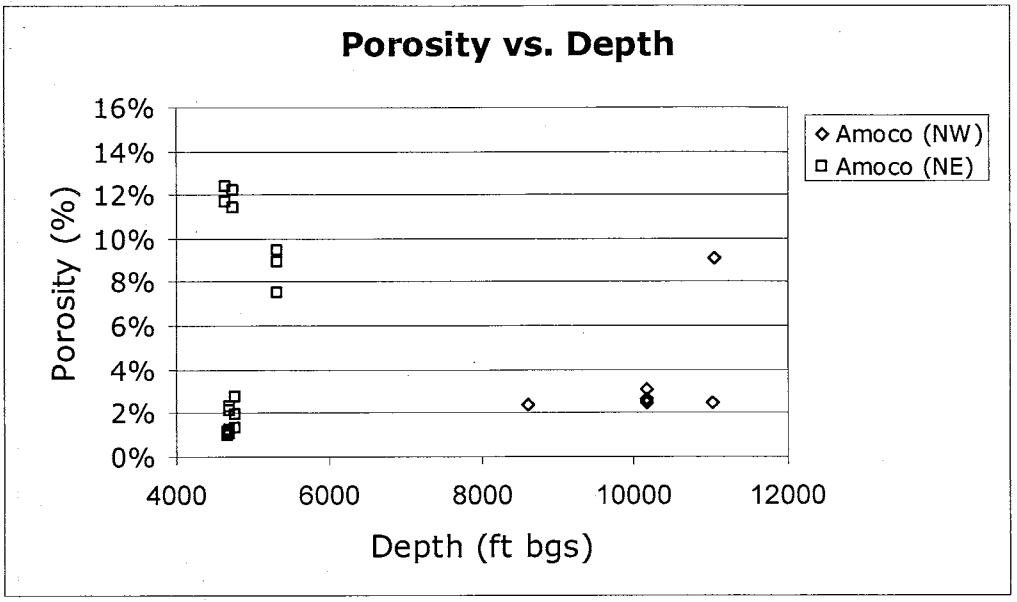

Figure 25: Porosity as a function of depth for the Amoco samples only; a general decrease in porosity with depth is apparent for most of the samples.

4.1.2 PERMEABILITY, DIFFUSIVITY, and STORATIVITY

Plans included in this research project were to measure permeability in the rock mechanics laboratory, and use this data to calculate diffusivity and storativity. Equipment problems arose and did not allow us to do so. The difficulties stemmed from electrical signal "drift" associated with the long testing period (~24 hours) needed for permeability measurement using the oscillating pore pressure method (discussed in Kranz et al., 1990). We were unable to eliminate this drift immediately. However, progress is being made and such data should be collected and published within the year. A preliminary constant-head permeability test was run in the lab (sample UB48) and indicated the permeability is on the order of 10^{-17} to 10^{-16} m^2.

We want to be able to analyze and discuss the conceptual model in terms of measured rock properties, including the context of diffusivity and storage properties. Data from a Utah Department of Natural Resources publication (Hood, 1976) are presented below in lieu of data measured in our laboratory. This report focused on

characteristics of aquifers in the northern Uinta Basin (slightly north of the DFZ); it does not include results from other (non-aquifer) layers. Data provided in this investigative report indicated that the upper sandy section of the Uinta Fm aquifer has a hydraulic conductivity of 3.04×10^{-5} m/s, transmissivity of 6.23×10^{-3} m^2/s, permeability of 3.1×10^{-12} m^2, and a porosity of 19.2 % (all are median values calculated from the data provided). Results are summarized in Table 7; for the complete data set, see Appendix III.

This research focuses on fluid pressure buildup, which is often limited by the lowest permeability layer. The presented permeability and hydraulic conductivity data should be analyzed in a qualitative manner, keeping in mind that the median value presented does not fairly represent the entire formation, nor is it the controlling value.

	POROSITY (%)	HYDRAULIC CONDUCTIVITY (m/s)	Calculated PERMEABILITY (m^2)	TRANSMISSIVITY (m^2/s)
N	4	52	52	55
Minimum	12.7	7.97×10^{-7}	8.13×10^{-14}	3.99×10^{-6}
Maximum	23.1	2.81×10^{-1}	2.87×10^{-8}	3.74×10^{0}
Median	19.2	3.04×10^{-5}	3.10×10^{-12}	6.23×10^{-3}

Table 7: Ranges and median values of porosity, hydraulic conductivity, permeability, and transmissivity for Uinta Fm aquifers; N is the number of samples; modified from Hood, 1976.

4.1.3 PALEO-PRESSURE and TEMPERATURE

Calcite precipitated in fractures was collected in the Balcron field area (Figure 6). Planned fluid inclusion analysis could provide paleo-temperature and paleo-pressure conditions at the time of calcite precipitation. As this research is being concluded, the fluid inclusion analysis has been planned to take place with the assistance of Erich Peterson from the University of Utah but has not yet been completed.

In addition, these samples were also those intended to investigate multiple episodes of calcite precipitation that may or may not support fault valve behavior. Polished thin sections were prepared and briefly examined through petrographic analysis. Such observations are not presented here due to an incomplete analysis.

4.2 MECHANICAL

4.2.1 TENSILE STRENGTH

Method Overview:

Brazil tests were used as an indirect method of measuring tensile strength. Disc-shaped samples were carefully drilled and prepared according to accepted standards which are outlined in Appendix II.

The sample was loaded across its diameter by the triaxial machine at the slowest speed. This loading (F) generates a compressive stress (σ_1) as well as a tensile stress (σ_3) oriented in a direction perpendicular to the applied load, as shown in Figure 26. The sample was oriented so that the induced tensional field was oriented north-south. When the applied load reaches a critical level, the sample fails in tension; the failure plane is oriented in a direction parallel to the applied load. The peak load reached by the sample recorded in force (N) was considered to be the point of failure. This was converted to a tensile stress (MPa) using the equation:

$$\mathbf{MPa = (2 \cdot F) / (\pi \cdot d \cdot L)}$$ *where* MPa = tensile stress
F = axial load at failure
d=sample diameter
L=sample thickness.

Results:

Due to the size of sample required for the tensile test, only select samples of

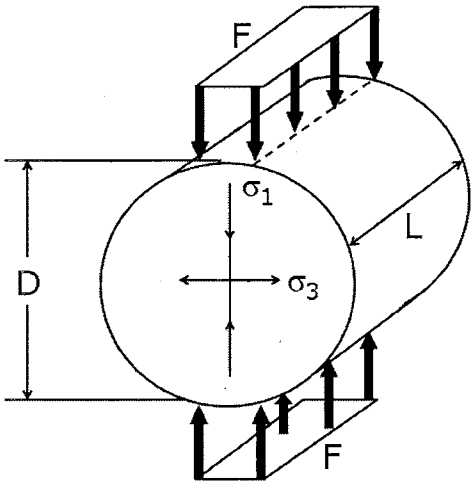

Figure 26: In Brazil tensile strength tests, a load (F) is applied which generates both a compressional (σ_1) and tensional (σ_3) stress on the sample; D is sample diameter; L is sample length/width; the sample will fail perpendicular to σ_3 once a critical load is reached.

the collected UB samples could be tested. Results of the tensile tests are reported in Table 8. Individual tests as well as the sample average and standard deviation within tests for each sample are shown.

Basic statistics were performed for the tensile strength measurements. The results are given in Table 9. For all of the *UB samples* (N=40), the range is 5.24-15.30, the mean is 10.57, and the standard deviation is 2.88 (values of tensile strength are reported in MPa). For *UB samples north of the DFZ* (N=8), the range is 9.60-15.30, the mean is 11.91, and the standard deviation is 1.83; for *UB samples in the DFZ* (N=30) the range is 5.24-15.20, the mean is 10.33, and the standard deviation is 3.03; for *UB samples in the DFZ* (N=2), the range is 6.55-11.00, the mean is 8.78, and the standard deviation is 3.14. There is no statistical difference between the porosity of UB samples north of, in, and south of the DFZ based on an ANOVA test (P-value of 0.263). An interesting pattern to note is the apparent discontinuity in the data from in the DFZ between samples 21 and 22. The exact reason for this is not known, but may simply be a coincidence. However, it should

SAMPLE	TENSILE STRENGTH (MPa)	AVG TENS STRENGTH (MPa)	ST DEV	LOCATION
35-T1	11.14	12.21	2.09	north of DFZ
35-T2	10.72			
35-T3	15.30			
35-T4	11.71			
48-T1	13.76	11.60	1.78	north of DFZ
48-T2	9.60			
48-T3	10.88			
48-T4	12.16			
21-T1	6.53	6.10	0.63	DFZ: Wells Canyon
21-T2	6.04			
21-T3	6.61			
21-T4	5.24			
22-T1	14.86	13.34	1.37	DFZ: Wells Canyon
22-T2	11.10			
22-T3	13.56			
22-T4	13.50			
22-T5	12.60			
22-T6	12.70			
22-T7	15.06			
26-T1	13.45	13.31	0.93	DFZ: Wells Canyon
26-T2	12.32			
26-T3	14.16			
27-T1	9.06	8.47	0.83	DFZ: Duchesne Graben
27-T2	7.88			
31-T1	10.19	8.80	1.04	DFZ: Duchesne Graben
31-T2	7.38			
31-T3	9.20			
31-T4	8.87			
31-T5	8.36			
39-T1	14.79	10.15	2.90	DFZ: south
39-T2	9.84			
39-T3	15.20			
39-T4	8.36			
39-T5	9.84			
39-T6	8.00			
39-T7	8.11			
39-T8	7.36			
39-T9	9.88			
41-T1	6.55	8.78	3.14	south of DFZ
41-T2	11.00			

Table 8: Values of tensile strength, average tensile strength, and standard deviation (ST DEV) for select UB samples.

be kept in mind that stresses are often concentrated at discontinuities.

Replicate plugs from the same sample were tested in order to gain an understanding of the amount of the inherent variability present in tensile tests. This variability is illustrated graphically in Figure 27. Using the sample averages with error bars equal to the standard deviation of that sample, tensile strength is plotted as a function of location with respect to the DFZ in Figure 28.

	UB Samples	*North of DFZ*	*In DFZ*	*South of DFZ*
N	40	8	30	2
Minimum	5.24	9.60	5.24	6.55
Maximum	15.30	15.30	15.20	11.00
Mean	10.57	11.91	10.33	8.78
Median	10.45	11.42	9.84	8.78
Standard Deviation	2.88	1.83	3.03	3.14

Table 9: Statistical analysis of measured tensile strength data; all values in MPa; N is the number of samples.

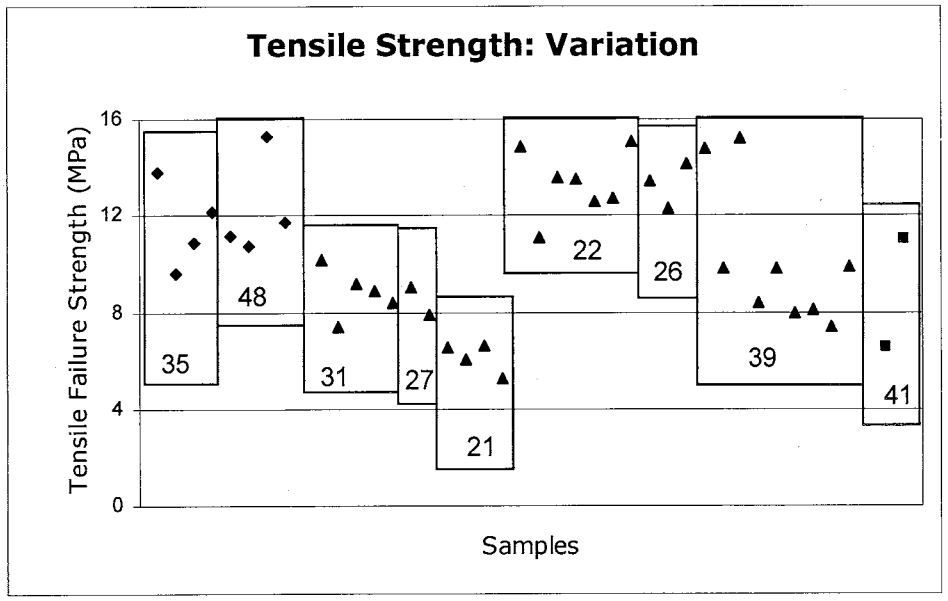

Figure 27: Inherent variation present in tensile strength tests; sample numbers are labeled; see Table 8 for location with respect to the DFZ.

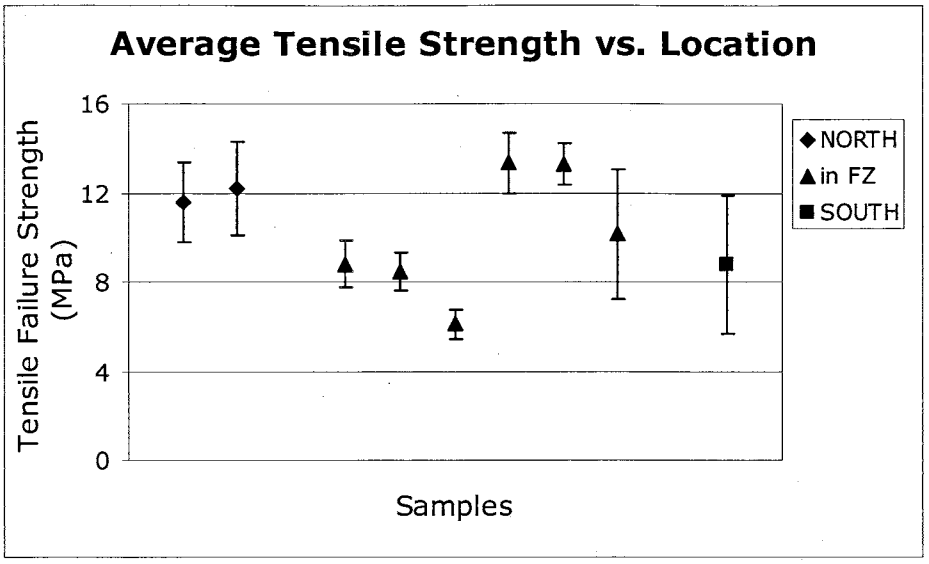

Figure 28: Tensile strength as a function of location with respect to the DFZ; error bars are shown for the tensile strength and are equal to the standard deviation.

4.2.2 COMPRESSIVE STRENGTH

Method Overview:

Uniaxial compressive tests were used to measure compressive strength. Similar to the tensile tests, cylindrical samples were carefully drilled and prepared according to accepted standards outlined in Appendix II. Strain gages were attached to the sample; UB collected samples had lateral and axial gages, while many of the Amoco samples had only axial gages (due to type of strain gage that was available and used). Vertical compressive strength was measured for all samples; horizontal compressive strength was measured for a number of Amoco samples in which enough core was available.

Load was applied to the top of the sample while leaving the load on the sides of the sample at atmospheric pressure. Strains in the axial and lateral directions were monitored by a strain gage and recorded using National Instruments Virtual Bench Logger. The load is cycled at a near-constant strain rate multiple times (up to

4 when possible) to demonstrate the elastic behavior of the rock. The test is finished when the sample is broken.

A number of elastic rock parameters may be calculated from this type of test. Young's Modulus (E) is the ratio of lateral stress to lateral strain and is generally associated with the stiffness of a material. Poisson's Ratio (υ) is the ratio of axial strain to lateral strain and gives an indication of the compressibility of the material being tested; for a perfectly incompressible material, υ=0.5. Bulk Modulus is the ratio of normal stress to change in volume, and provides an indication of a sample's resistance to change in volume, or shape.

Results:

Because the size of the plug required for testing compressive strength and related elastic parameters is relatively small, most samples could be tested. Results and calculated elastic parameters are reported in Tables 10 and 11.

A basic statistical analysis of the compressive strength measurements and associated elastic parameter calculations was performed. The results of the statistical analysis for these measurements are given in Tables 12 and 13. For *all samples* (N=43), the range of measured compressive strengths is 55-233, the mean strength is 132, and the standard deviation is 52 (values of compressive strength reported in MPa). For *all UB samples* (N=14), the range is 66-228, the mean is 149, and the standard deviation is 48; *UB samples north of the DFZ* (N=3) have a range of 123-149, a mean of 136, and a standard deviation of 13; *UB samples in the DFZ* (N=9) have a range of 66-228, a mean of 160, and a standard deviation of 57; *UB samples south of the DFZ* (N=2) have a range of 105-136, a mean of 120, and a standard deviation of 22. *Amoco samples* (N=27) have a range of 55-233, a mean of 124, and a standard deviation of 53.

Values of E for *all UB samples* (N=14) ranged from 2.8×10^4-6.1×10^4 with a

SAMPLE		COMPRESSIVE STRENGTH (MPa)	AVG COMP STRENGTH (MPa)	LOCATION
35A	V	136		north of DFZ
48B	V	123	136	north of DFZ
48C	V	149		north of DFZ
21D	V	66		DFZ: Wells Canyon
22E	V	97	99	DFZ: Wells Canyon
22F	V	102		DFZ: Wells Canyon
23B	V	228		DFZ: Wells Canyon
26A	V	201	200	DFZ: Wells Canyon
26C	V	199		DFZ: Wells Canyon
27D	V	125		DFZ: Duchesne Graben
31A	V	130	146	DFZ: Duchesne Graben
31C	V	163		DFZ: Duchesne Graben
39B	V	224		DFZ: south
40H	V	136		south of DFZ
41A	V	105		south of DFZ
A_4645A	V	107	107	northeast of DFZ
A_4645B	V	108		northeast of DFZ
A_4645C	H	108		northeast of DFZ
A_4672A	V	90	85	northeast of DFZ
A_4672B	H	79		northeast of DFZ
A_4712A	H	86	77	northeast of DFZ
A_4712B	H	55		northeast of DFZ
A_4712C	V	87		northeast of DFZ
A_4712D	V	83		northeast of DFZ
A_4712E	V	75		northeast of DFZ
A_4712F	V	73		northeast of DFZ
A_4743A	H	57	57	northeast of DFZ
A_4743B	V	57		northeast of DFZ
A_4774A	V	172	183	northeast of DFZ
A_4774B	V	186		northeast of DFZ
A_4774C	H	192		northeast of DFZ
A_5320A	V	111	102	northeast of DFZ
A_5320B	H	101		northeast of DFZ
A_5320C	H	93		northeast of DFZ
A_8602	V	231		northwest of DFZ
A_10157	V	160		northwest of DFZ
A_10168	V	161		northwest of DFZ
A_10171A	V	128	151	northwest of DFZ
A_10171B	V	173		northwest of DFZ
A_10176A	V	188	168	northwest of DFZ
A_10176B	V	148		northwest of DFZ
A_11030	V	233		northwest of DFZ

Table 10: Values of compressive strength and average compressive strength (where applicable) for UB samples and Amoco samples; V indicates vertical orientation with respect to drilled core; H indicates horizontal.

SAMPLE		POISSON'S RATIO (no units)	YOUNG'S MODULUS (MPa)	BULK MODULUS (GPa)	LOCATION
35A	V	0.24	54,396	95,086	north of DFZ
48B	V	0.15	31,571	40,461	north of DFZ
48C	V	0.14	50,033	68,429	north of DFZ
21D	V	0.17	28,461	41,867	DFZ: Wells Canyon
22E	V	0.16	64,224	86,306	DFZ: Wells Canyon
22F	V	0.14	51,349	72,426	DFZ: Wells Canyon
23B	V	0.25	57,438	103,010	DFZ: Wells Canyon
26A	V	0.24	53,646	100,030	DFZ: Wells Canyon
26C	V	0.19	60,365	97,926	DFZ: Wells Canyon
27D	V	0.18	43,305	72,969	DFZ: Duchesne Graben
31A	V	0.20	42,909	71,763	DFZ: Duchesne Graben
31C	V	0.19	39,175	68,407	DFZ: Duchesne Graben
39B	V	0.26	61,087	127,330	DFZ: south
40H	V	0.21	47,027	79,391	south of DFZ
41A	V	0.26	35,641	72,870	south of DFZ
A_4645A	V		35,738		northeast of DFZ
A_4645B	V		22,604		northeast of DFZ
A_4645C	H		31,351		northeast of DFZ
A_4672A	V		33,976		northeast of DFZ
A_4672B	H		36,792		northeast of DFZ
A_4712A	H		45,227		northeast of DFZ
A_4712B	H		69,299		northeast of DFZ
A_4712C	V		33,227		northeast of DFZ
A_4712D	V		68,389		northeast of DFZ
A_4712E	V		56,621		northeast of DFZ
A_4712F	V		36,374		northeast of DFZ
A_4743A	H		24,402		northeast of DFZ
A_4743B	V		26,338		northeast of DFZ
A_4774A	V		56,902		northeast of DFZ
A_4774B	V		61,682		northeast of DFZ
A_4774C	H		62,312		northeast of DFZ
A_5320A	V		48,780		northeast of DFZ
A_5320B	H		33,236		northeast of DFZ
A_5320C	H		32,621		northeast of DFZ
A_8602	V	0.17	62,747	88,975	northwest of DFZ
A_10157	V	0.12	48,941	50,658	northwest of DFZ
A_10168	V		16,904		northwest of DFZ
A_10171A	V		50,739		northwest of DFZ
A_10171B	V		61,784		northwest of DFZ
A_10176A	V		49,021		northwest of DFZ
A_10176B	V		40,114		northwest of DFZ
A_11030	V	0.10	57,354	55,139	northwest of DFZ

Table 11: Values of elastic parameters for UB samples and Amoco samples; V indicates vertical orientation with respect to drilled core; H indicates horizontal.

	All Samples	*UB Samples*	*North of DFZ*	*In DFZ*	*South of DFZ*	*Amoco Samples*
N	43	14	3	9	2	27
Minimum	55	66	123	66	105	55
Maximum	233	228	149	228	136	233
Mean	132	149	136	160	120	124
Median	125	136	136	163	120	108
Standard Deviation	52	48	13	57	22	53

Table 12: Statistical analysis of measured compressive strength data; all values in MPa; N is the number of samples.

		All Samples	*UB Samples*	*North of DFZ*	*In DFZ*	*South of DFZ*	*Amoco Samples*
YOUNG'S MODULUS (MPa)	N	43	14	3	9	2	27
	Minimum	1.7×10^4	2.8×10^4	3.2×10^4	2.8×10^4	3.6×10^4	1.7×10^4
	Maximum	6.9×10^4	6.1×10^4	5.4×10^4	6.1×10^4	3.6×10^4	6.9×10^4
	Mean	4.5×10^4	4.7×10^4	4.5×10^4	4.9×10^4	4.1×10^4	4.5×10^4
	Median	4.7×10^4	4.9×10^4	5.0×10^4	5.1×10^4	4.1×10^4	4.5×10^4
	Standard Deviation	1.4×10^4	1.0×10^4	1.2×10^4	1.1×10^4	8.1×10^3	1.5×10^4
POISSON'S RATIO (no units)	N	17	14	3	9	2	3
	Minimum	0.10	0.14	0.14	0.14	0.21	0.10
	Maximum	0.26	0.26	0.24	0.26	0.26	0.17
	Mean	0.19	0.20	0.18	0.20	0.23	0.13
	Median	0.19	0.20	0.15	0.19	0.23	0.12
	Standard Deviation	0.05	0.04	0.05	0.04	0.04	0.04
BULK MODULUS (GPa)	N	17	14	3	9	2	3
	Minimum	4.0×10^4	4.0×10^4	4.0×10^4	4.2×10^4	7.3×10^4	5.1×10^4
	Maximum	1.3×10^5	1.3×10^5	9.5×10^4	1.3×10^5	7.9×10^4	8.9×10^4
	Mean	7.7×10^4	7.9×10^4	6.8×10^4	8.4×10^4	7.6×10^4	6.5×10^4
	Median	7.3×10^4	7.3×10^4	6.8×10^4	7.3×10^4	7.6×10^4	5.5×10^4
	Standard Deviation	2.3×10^4	2.4×10^4	2.7×10^4	2.5×10^4	4.6×10^3	2.1×10^4

Table 13: Statistical analysis of calculated elastic parameters; N=number of samples.

mean of $4.7x10^4$ MPa; the *Amoco samples* (N=27) ranged from $1.7x10^4$-$6.9x10^4$ with a mean of $4.5x10^4$ MPa. Values of E for *all UB samples* (N=14) ranged from $2.8x10^4$-$6.1x10^4$ with a mean of $4.7x10^4$ MPa; the *Amoco samples* (N=27) ranged from $1.7x10^4$-$6.9x10^4$ with a mean of $4.5x10^4$ MPa. Typical values of E for siltstones and shales range from $1x10^4$-$6x10^4$ MPa (Middleton and Wilcock, 1994); Narr and Currie (1982) used an estimate of $4x10^4$-$7x10^4$ MPa for the general Uinta Basin; a DOE Report (Lemmon and others, 1998) reported values ranging from $9.0x10^3$-$2.8x10^4$ MPa for samples collected from a depth of 1,500 m in the Balcron field area, and used a value of $1.4x10^4$ MPa in associated numerical analyses. Generally speaking, larger values of E are expected for harder, more resistant materials.

For *all UB samples* (N=14), υ ranged from 0.14-0.26 with a mean of 0.20 (no units); the *Amoco samples* (N=3) ranged from 0.10-0.17 with a mean of 0.13 (no units). A typical range of values of υ for shales is 0.1-0.2; sandstones commonly have a value between 0.2-0.3 (Middleton and Wilcock, 1994); Narr and Currie (1982) used values of 0.25 and 0.45 for the general Uinta Basin. Values determined in this study fall in this suggested shale/sandstone range.

Bulk Modulus for *all UB samples* (N=14) ranged from $4.0x10^4$-$1.3x10^5$ with a mean of $7.9x10^4$ GPa; *Amoco samples* (N=3) ranged from $5.1x10^4$-$8.9x10^4$ with a mean of $6.5x10^4$ GPa. There is no statistical difference between the porosity of UB samples north of, in, and south of DFZ based on an ANOVA test (P-value of 0.543).

In a number of cases, replicates were tested from the same sample to verify the method being used. The variability present in these tests is relatively small (Figure 29). The variability present is thought to be the result of heterogeneities within the sample and is expected. Compressive strength versus location shows no particular trend (Figure 30).

Horizontal-oriented plugs were tested for a number of the Amoco rock samples. The average for all vertical samples is 135 MPa; for horizontal samples the average is 96 MPa. This appears to be a difference at first glance. This is not the case, however, since the horizontal samples were tested only for Amoco samples corresponding to depths less than 6,000 feet (northeast of the DFZ). The average for vertical samples <6,000 feet is 104 MPa, which is not significantly different than the 96 MPa average for horizontal samples in the same depth range. The average for vertical samples with depths greater than 8,000 feet (northwest of the DFZ) is 178 MPa. There does not appear to be a significant difference between vertical and horizontal compressive strength. However, there is a general difference in strength between the two locations due to the difference in depths between the two locations. Figure 31 illustrates the difference in depth versus location (samples northeast of the

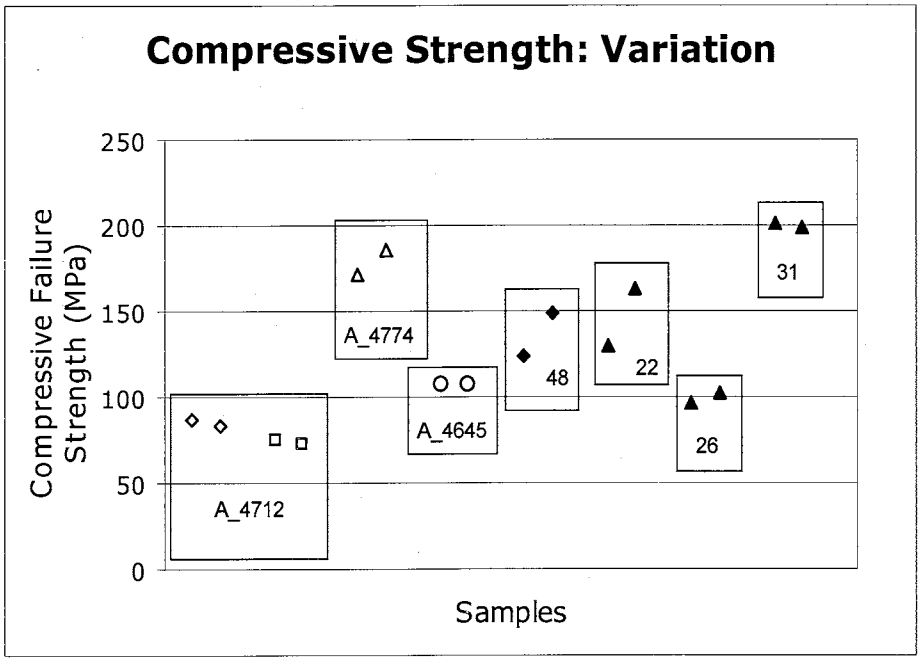

Figure 29: Compressive strength variation; data shown is for vertical compression only; *symbols used for the Amoco samples do not correspond to the notation normally used.*

DFZ are from shallower depths) as well as the lack of difference in orientation of the plug with respect to compressive strength (horizontal and vertical samples from the northeast show no difference).

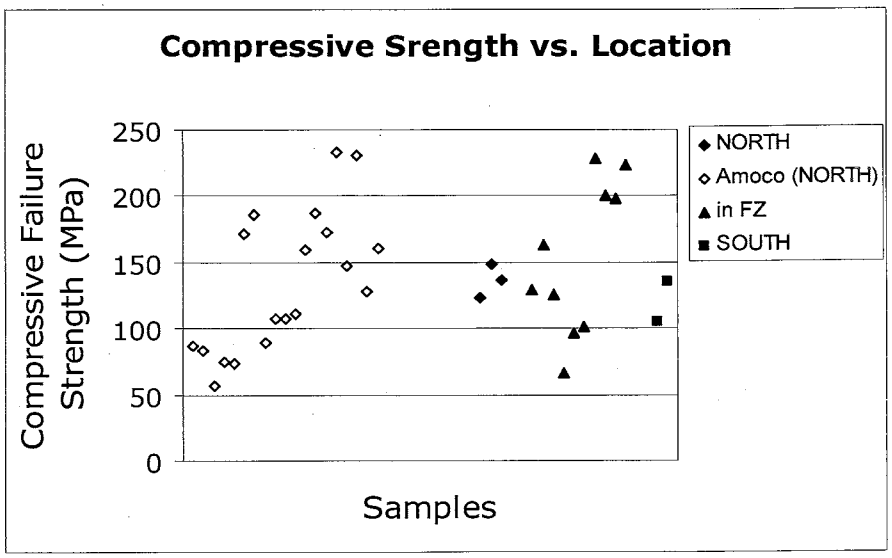

Figure 30: Compressive strength as a function of location with respect to the DFZ; data shown is for vertical compression only.

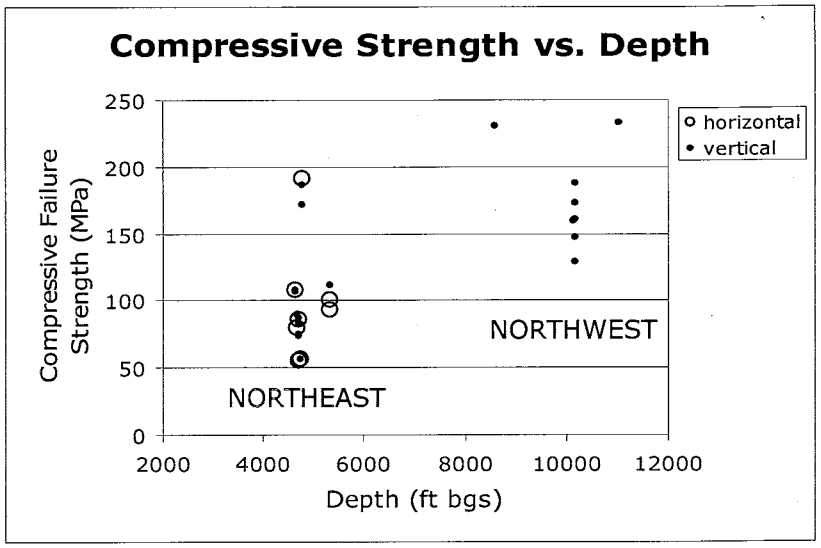

Figure 31: Compressive strength plotted as a function of depth illustrating the lack of difference between horizontal and vertical compressive strength; Amoco samples only are plotted; samples with depths <6,000 ft are located northeast of the DFZ; depths >8,000 ft are located northwest of the DFZ.

mean of $4.7x10^4$ MPa; the *Amoco samples* (N=27) ranged from $1.7x10^4$-$6.9x10^4$ with a mean of $4.5x10^4$ MPa. Values of E for *all UB samples* (N=14) ranged from $2.8x10^4$-$6.1x10^4$ with a mean of $4.7x10^4$ MPa; the *Amoco samples* (N=27) ranged from $1.7x10^4$-$6.9x10^4$ with a mean of $4.5x10^4$ MPa. Typical values of E for siltstones and shales range from $1x10^4$-$6x10^4$ MPa (Middleton and Wilcock, 1994); Narr and Currie (1982) used an estimate of $4x10^4$-$7x10^4$ MPa for the general Uinta Basin; a DOE Report (Lemmon and others, 1998) reported values ranging from $9.0x10^3$-$2.8x10^4$ MPa for samples collected from a depth of 1,500 m in the Balcron field area, and used a value of $1.4x10^4$ MPa in associated numerical analyses. Generally speaking, larger values of E are expected for harder, more resistant materials.

For *all UB samples* (N=14), υ ranged from 0.14-0.26 with a mean of 0.20 (no units); the *Amoco samples* (N=3) ranged from 0.10-0.17 with a mean of 0.13 (no units). A typical range of values of υ for shales is 0.1-0.2; sandstones commonly have a value between 0.2-0.3 (Middleton and Wilcock, 1994); Narr and Currie (1982) used values of 0.25 and 0.45 for the general Uinta Basin. Values determined in this study fall in this suggested shale/sandstone range.

Bulk Modulus for *all UB samples* (N=14) ranged from $4.0x10^4$-$1.3x10^5$ with a mean of $7.9x10^4$ GPa; *Amoco samples* (N=3) ranged from $5.1x10^4$-$8.9x10^4$ with a mean of $6.5x10^4$ GPa. There is no statistical difference between the porosity of UB samples north of, in, and south of DFZ based on an ANOVA test (P-value of 0.543).

In a number of cases, replicates were tested from the same sample to verify the method being used. The variability present in these tests is relatively small (Figure 29). The variability present is thought to be the result of heterogeneities within the sample and is expected. Compressive strength versus location shows no particular trend (Figure 30).

Horizontal-oriented plugs were tested for a number of the Amoco rock samples. The average for all vertical samples is 135 MPa; for horizontal samples the average is 96 MPa. This appears to be a difference at first glance. This is not the case, however, since the horizontal samples were tested only for Amoco samples corresponding to depths less than 6,000 feet (northeast of the DFZ). The average for vertical samples <6,000 feet is 104 MPa, which is not significantly different than the 96 MPa average for horizontal samples in the same depth range. The average for vertical samples with depths greater than 8,000 feet (northwest of the DFZ) is 178 MPa. There does not appear to be a significant difference between vertical and horizontal compressive strength. However, there is a general difference in strength between the two locations due to the difference in depths between the two locations. Figure 31 illustrates the difference in depth versus location (samples northeast of the

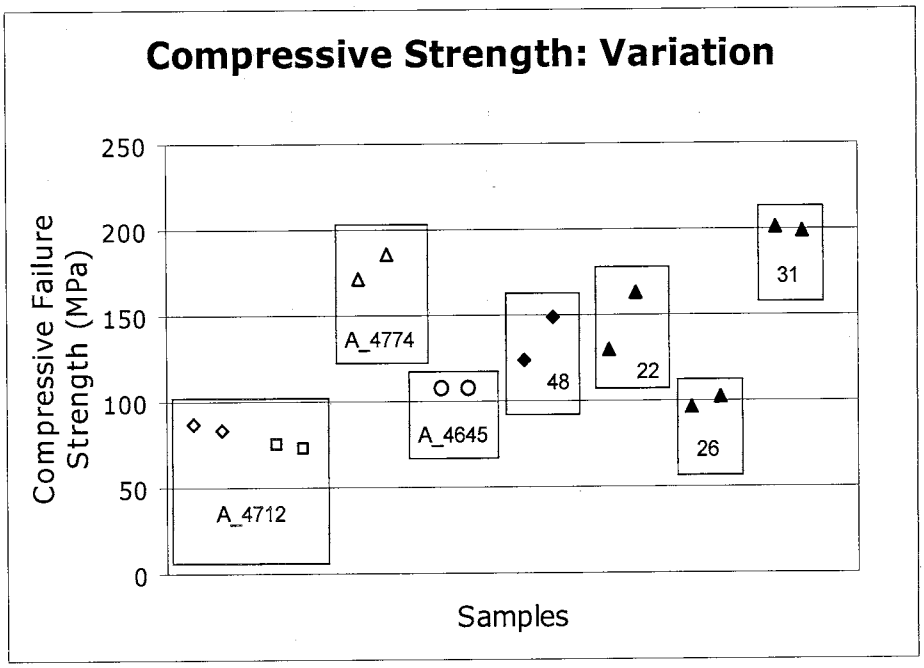

Figure 29: Compressive strength variation; data shown is for vertical compression only; *symbols used for the Amoco samples do not correspond to the notation normally used.*

DFZ are from shallower depths) as well as the lack of difference in orientation of the plug with respect to compressive strength (horizontal and vertical samples from the northeast show no difference).

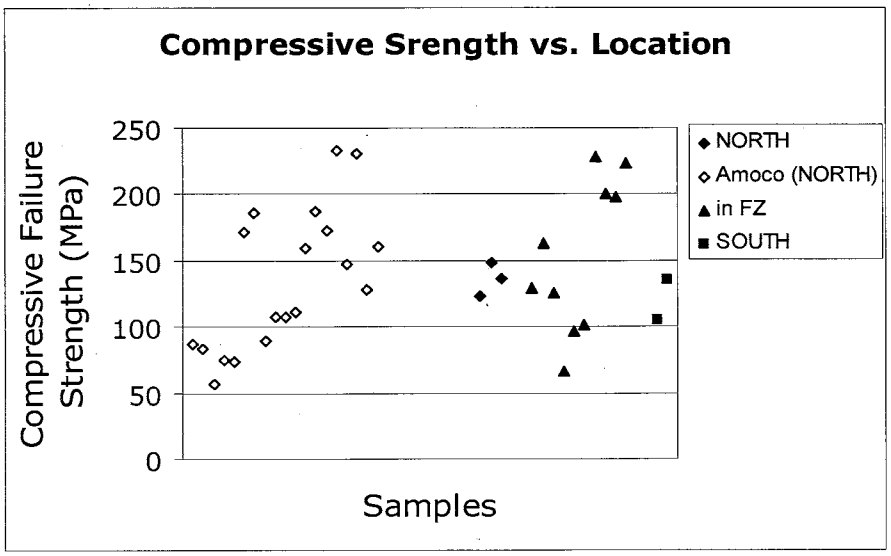

Figure 30: Compressive strength as a function of location with respect to the DFZ; data shown is for vertical compression only.

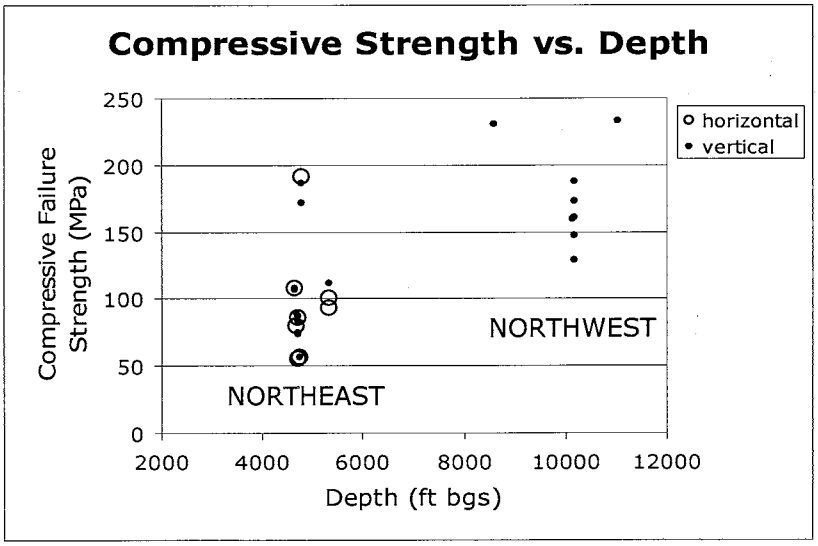

Figure 31: Compressive strength plotted as a function of depth illustrating the lack of difference between horizontal and vertical compressive strength; Amoco samples only are plotted; samples with depths <6,000 ft are located northeast of the DFZ; depths >8,000 ft are located northwest of the DFZ.

4.3 PHYSICAL

4.3.1 ROCK FRAMEWORK

4.3.1.1 *PETROGRAPHIC ANALYSIS*

Method Overview:

Thin sections were prepared from a location as close as possible to the samples drilled for mechanical testing. The sections were stained with alizarin red-S to facilitate differentiation between calcite and dolomite; this was not as successful as planned, since the acid dissolved many of the grains. Thin sections were analyzed along with the assistance of Dana Ulmer-Scholle. Analysis included rock type, relative grain size, and degree of compaction (this section); mineralogical and biological components (Section 4.3.2.2); cement type, amount, and character (Section 4.3.3). Results regarding general rock type, relative grain size, and degree of compaction are discussed here; the rest will be discussed in the following sections.

Results:

The results of the thin section analysis of the collected UB samples are presented in Table 14. Samples fell into two broad categories: carbonate micrites and clastic litharenites. Thin sections of fracture-filling calcite material were also briefly examined, but the results are not presented here due to lack of a final and complete analysis. There was no geographical division corresponding to this trend which is not too surprising since the DFZ area is a transition zone. Relative grain size has previously been described as decreasing from north to south across the DFZ. This trend is visible in the thin sections, but may be dampened due to limited sampling. A general trend of increasing compressive strength with decreasing grain strength is illustrated in Figure 32. There is no similar trend with

SAMPLE	ROCK TYPE	RELATIVE GRAIN SIZE 1= finer	COMPACTION	LOCATION
035	-carbonate -micrite	mud (4)	none evident	north of DFZ
048	-clastic -litharenite w/ muddy layers	9	major	north of DFZ
021	-clastic -feldspathic litharenite	10	significant	DFZ: Wells Canyon
022	-clastic -feldspathic litharenite	10	significant	DFZ: Wells Canyon
023	-carbonate -micrite	mud (2.5)	none evident	DFZ: Wells Canyon
026	-carbonate -micrite	mud (6)	minimal	DFZ: Wells Canyon
027	-clastic -feldspathic litharenite	10	significant	DFZ: Duchesne Graben
031	-carbonate -micrite	mud (7)	significant	DFZ: Duchesne Graben
039	-carbonate -micrite	mud (5)	minor	DFZ: South
040	-carbonate -micrite	mud (1)	minor; more than 041	south of DFZ
041	-carbonate -micrite	mud (2.5)	minor	south of DFZ

Table 14: Results of thin section analysis regarding rock type, grain size, and compaction; arbitrary numbers were assigned to grain size and for graphical purposes.

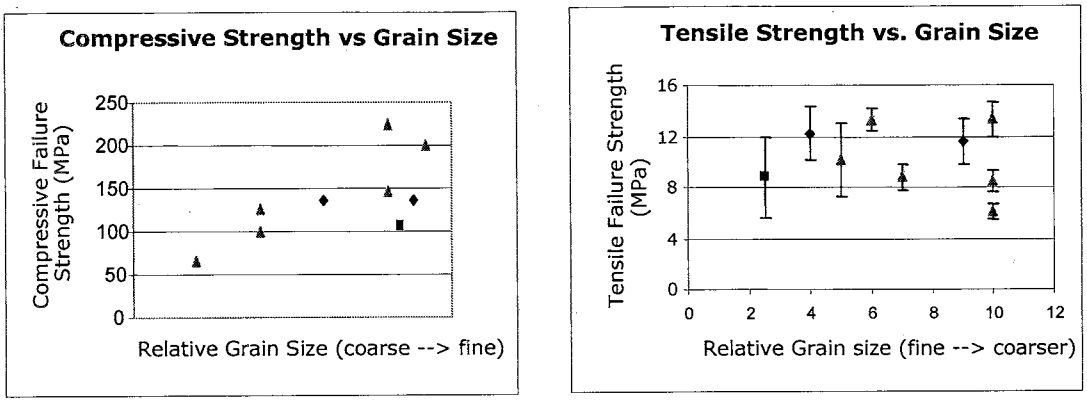

Figure 32: Graphs of compressive and tensile strength versus grain size showing the general trend of decreasing compressive strength with increasing grain size; there is no evident trend with tensile strength.

tensile strength. Compaction in the samples varied from none evident to major amounts, and had no geographical trend. Strength was expected to be influenced by amount of compaction; however, this was not evident in the analysis.

4.3.1.2 *SCANNING ELECTRON MICROSCOPE (SEM) IMAGING*

Method Overview:

Samples were analyzed using the Cameca SX-100 electron microprobe facility at the New Mexico Bureau of Geology and Mineral Resources along with the assistance of Lynn Heizler to create secondary electron images. As with XRD analysis, SEM imaging is strongly influenced by any heterogeneity in the sample. These images were analyzed and compared in terms of rock framework. This was expected to be useful in explaining character (porosity and permeability) and mechanical behavior. All of the SEM images that were taken are in Appendix IV, available only in the electronic version of this thesis (due to size).

Results:

When interpreting the differences and meaning of the SEM images, it is important to keep in mind that carbonate and clastic samples should be compared

with caution. These two classes of rocks are inherently different in terms of framework and composition and respond to stresses differently. SEM images were taken for all of the carbonate samples (see Table 14 for those classified as carbonates) and one clastic sample (#21) for general comparison.

Overall, there were no significant patterns evident in the samples. The results presented are extreme cases; the rest of the samples fell between the extremes. Grain size differences are illustrated in Figure 33. The images show a very fine-grained carbonate sample (#40) with grains ranging in size from ~1-5 μm, a less fine-grained carbonate sample (#31) with grain sizes of ~2–10 μm, and a clastic sample (#21) with grain sizes of ~2-150 μm. Minor but obvious differences are present. SEM images in Figure 34 are compared with strength. Values for minimum and maximum measured compressive and tensile strength are given in the table. Sample #41 was a relatively weak sample, and sample #26 was relatively strong. The major difference between the samples is that of grain size and distribution. Sample #26 is fine-grained, and most grains are the same size. On the other hand, sample #41 has a non-uniform grain size, with the average size being larger than the grain size of sample #26. This distribution of grain size is likely to impact packing within the samples, which may influence strength.

4.3.2 MINERALOGY

Mineralogy of the collected UB samples was analyzed using two different methods: X-ray diffraction (XRD) and petrographic analysis. The benefits to be gained from each were unique. XRD analysis is quick and machine-analyzed; thin sections are more time consuming but allow an analysis of spatial distribution and can give quantitative results. Results from the two methods are not the same, probably because of heterogeneities within the samples. In addition, thin sections

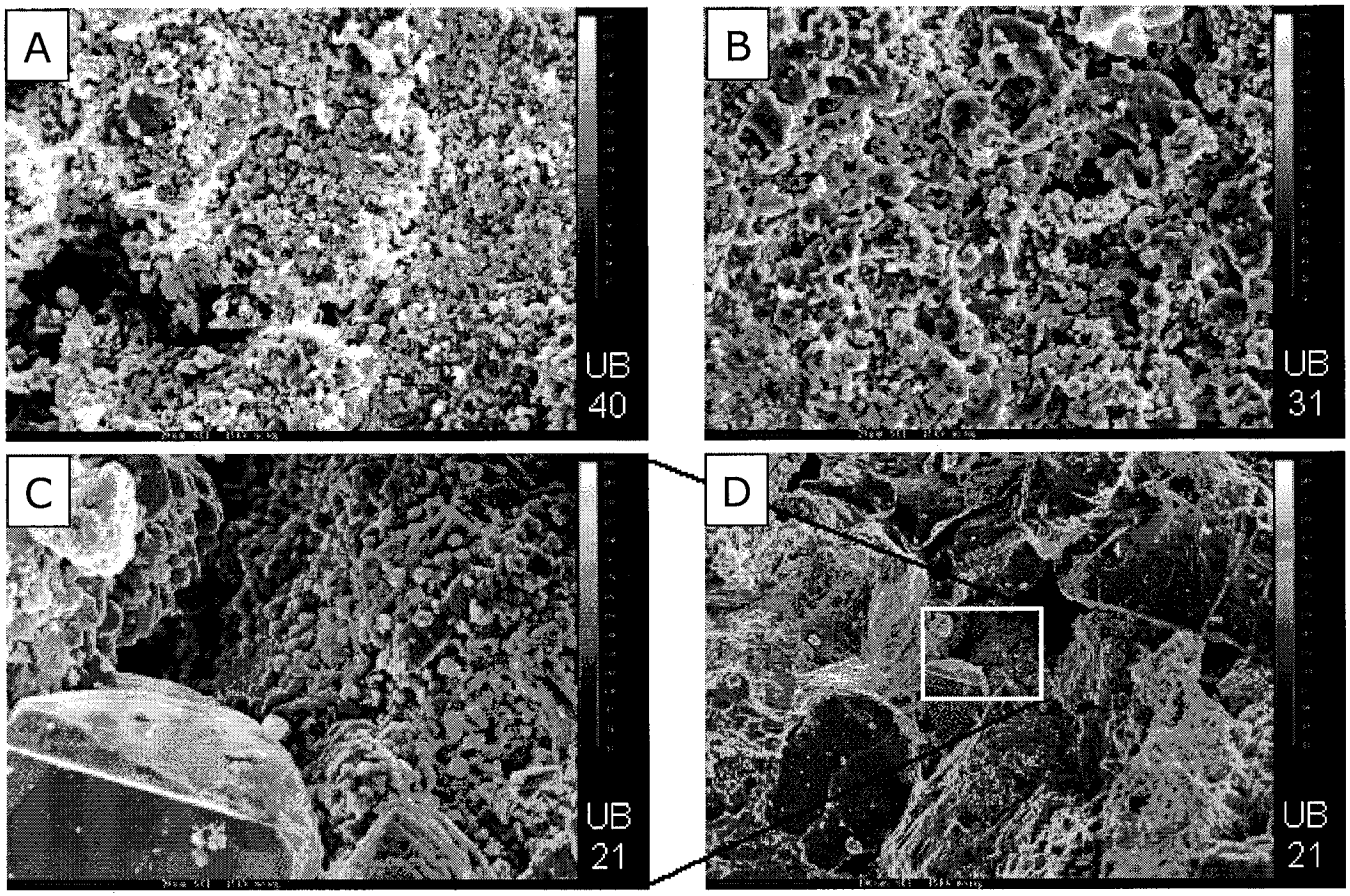

Figure 33: SEM images illustrating differences in grain size between (A) finer-grained carbonates, (B) less fine-grained carbonates, and (C) a clastic rock sample; images (A-C) are taken at the same scale with a field of view of 120 µm; image (D) shows UB21 in a zoomed out view as well as the location of (C) and has a field of view of 600 µm.

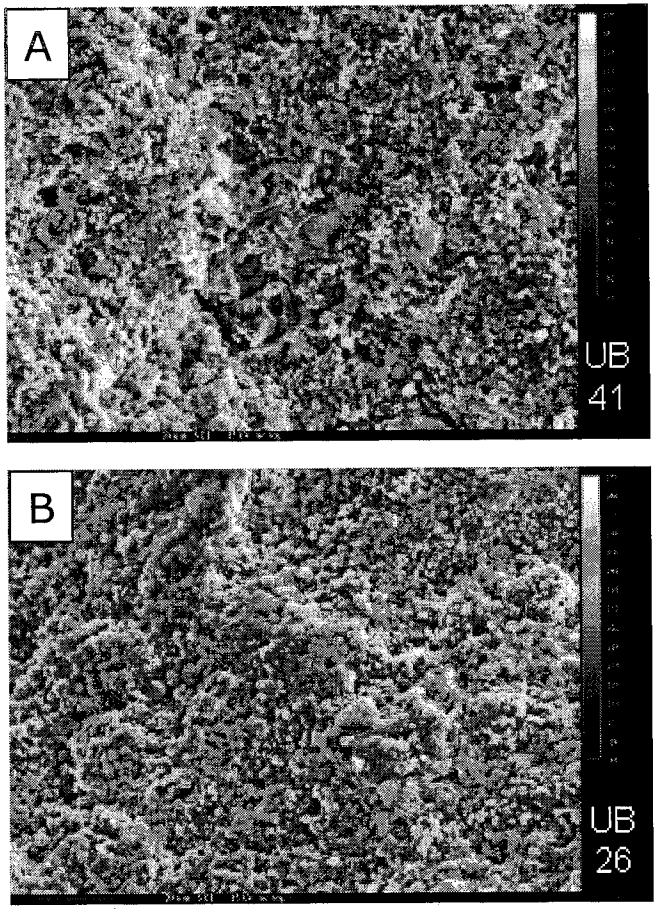

	Tensile Strength (MPa)	Compressive Strength (MPa)
Minimum	8.78 (#21: 6.10)	105 (#21: 66)
Maximum	13.31	224
UB 41	8.78	105
UB 26	13.31	200

Figure 34: SEM images illustrating samples with relatively (A) low and (B) high compressive and tensile strengths; field of view is 120 μm; table shown gives values for the two samples illustrated as well as the range of values for the samples tested.

were used from the middle of the rock, while samples for XRD were broken from the edges of the original, larger sample.

4.3.2.1 *X-RAY DIFFRACTION (XRD)*

Method Overview:

Samples were analyzed using the X-ray facility at the New Mexico Bureau of Geology and Mineral Resources along with the assistance of Chris McKee. The data was collected using DataScan 3.1 then analyzed for major mineral components using MDI Jade 6.5. It should be noted that XRD is a rough method of identifying major mineralogical components in rocks and should not be used in a quantitative sense. It is very dependent on heterogeneities within the sample since only a small portion of the sample is used for analysis. Method details are discussed in Appendix II.

Results:

XRD-analyzed samples are shown in Figure 35 are presented as relative amounts. For example, the analysis of sample #48 showed strong peaks for quartz

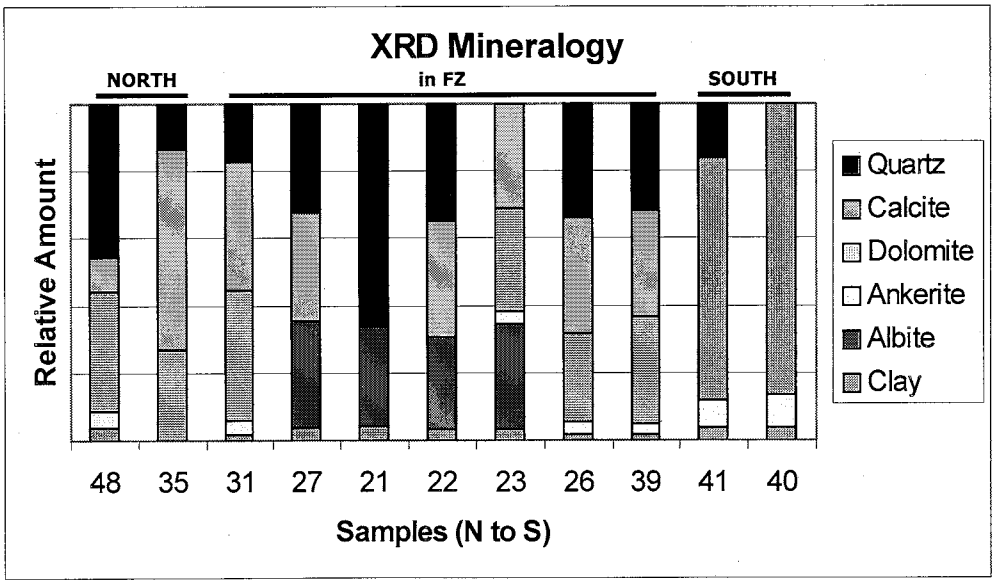

Figure 35: Qualitative XRD results showing the major mineralogical components of the UB samples detected by the MDI Jade software; larger areas correspond to more intense peaks.

and dolomite, a not so strong peak for calcite, a weak peak for ankerite, and only a trace peak for clay. Quartz, calcite, and dolomite are present in significant quantities in most of the samples. Trace amounts of clay are also noted in almost all of the samples. The most evident pattern is that of albite occurring only in the DFZ. This trend is weak. Albite occurs in both the eastern and western parts of the DFZ, but not in all samples from the DFZ. Additionally, there is no corresponding pattern in mineralogy from thin section analysis (will be discussed in Section 4.3.2.2). Investigating this trend in more depth is a suggestion made in Chapter 6: Recommendations for Future Work.

4.3.2.2 *PETROGRAPHIC ANALYSIS*

Method Overview:

Thin sections were analyzed for mineralogical and biological components using a point count of 200-300 grains. Specific bioclast identification is not presented.

Results:

Mineralogy resulting from thin section analysis is slightly different than XRD analysis. This isn't too surprising since both methods use a very small sample size, which can enhance heterogeneities that are present. Amounts of calcite, dolomite, and quartz are present in most of the samples in significant quantities. Mud is the major constituent of the carbonate samples. Rock fragments include both sedimentary and volcanic; the majority are volcanic. Other components that comprise less than 5% of the sample include biotite, muscovite, hydrocarbon, iron oxide, and unidentified opaques. See Table 15 for a complete description of composition. For location of samples, see Table 14.

SAMPLE	QUARTZ (%)	ROCK FRAG's (volc. and sed.) (%)	FELDSPAR (%)	CALCITE/ DOLOMITE (%)	MUD (%)	BIOCLASTS (%)	OTHER (<5%)
035	5	none	none	10	75	10	FeO
048	39	7.5	1	21.1	29.1	none	FeO opaques
021	59	19.3	8	5.1	4	none	biotite muscovite FeO
022	59.5	20.2	16.1	3.6	none	none	biotite muscovite opaques hydrocarbon
023	2.5	none	none	3	90	3	FeO
026	1	none	none	None	90	7	FeO
027	54.5	13.1	29	12.6	none	none	biotite muscovite FeO
031	5	none	none	None	85	8	FeO
039	1	none	none	1	95	2	FeO
040	1	none	<1	7	90	1	FeO
041	2	none	none	3	95	0	FeO

Table 15: Results of thin section analysis regarding mineralogical and biological components.

4.3.3 CEMENTATION: Type, Amount, and Location

Method Overview:

Thin sections were analyzed in terms of cement amount, type, and character. For the clastic samples, a point count of 200-300 grains provided a percentage of cement. For the carbonates, grain size was so fine that a quantitative point count could not be performed. For these fine-grained samples, a coating of cement on the grains was assumed; this seemed reasonable in all of the cases where an abundance of carbonate was present.

Results:

Table 16 shows results regarding cementation in the collected UB samples. For location of samples, see Table 14. A quantitative count of percent of cement is given for the clastic samples only. Cement type was generally 'carbonate' (calcite or dolomite) in all samples; a differentiation between these was only possible in the

clastic samples where crystal forms were present. Amount of cement versus compressive and tensile strength is plotted (Figure 36). Although a trend might be expected to exist between cement and strength, none is evident.

Because of the lack of any obvious trend with amount of cement, the character of the cement was investigated. This was determined by looking at where the cement was located in the sample. An arbitrary value between 1 and 5 was

SAMPLE	CEMENT (%)	CEMENT TYPE	CEMENT CHARACTER 1=spotty; 5=continuous
035	n/a	n/a	coating grains (5)
048	2.6	dolomite	small isolated patches; coating grains (in mud layers) (4)
021	11.5	dolomite	Patchy (1)
022	32.8	calcite	Patchy (2)
023	n/a	n/a	coating grains (5)
026	n/a	n/a	coating grains (5)
027	20.8	calcite	relatively continuous throughout (3)
031	n/a	n/a	coating grains (5)
039	n/a	n/a	coating grains (5)
040	n/a	n/a	coating grains (5)
041	n/a	n/a	coating grains (5)

Table 16: Results of thin section analysis regarding cement amount (for clastic samples), cement type, and the character of the cement.

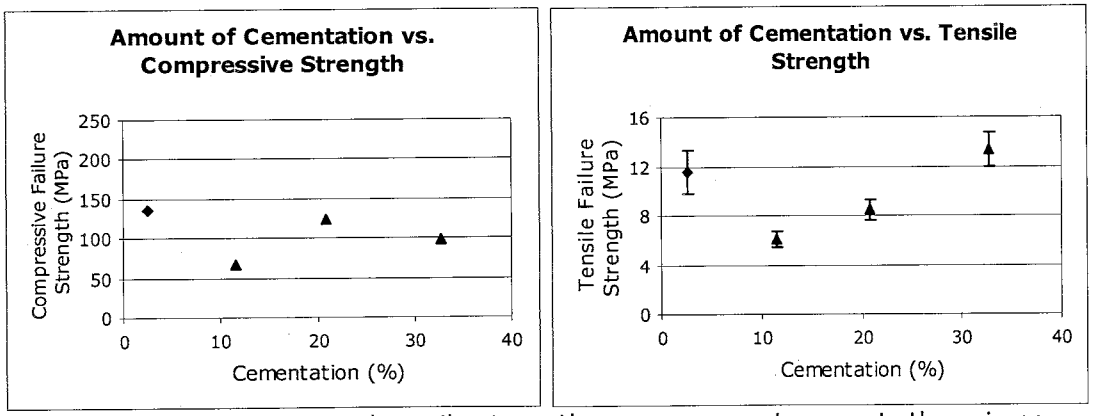

Figure 36: Compressive and tensile strength versus percent cement; there is no apparent correlation.

assigned to the cement character so that a plot could be made to look for patterns or trends. A value of 1 corresponded to those samples that had cement spotted throughout the sample; a value of 5 corresponded to samples that had continuous cement throughout the sample. Overall, there is a general increase in mechanical strength with increasing cement continuity (Figure 37).

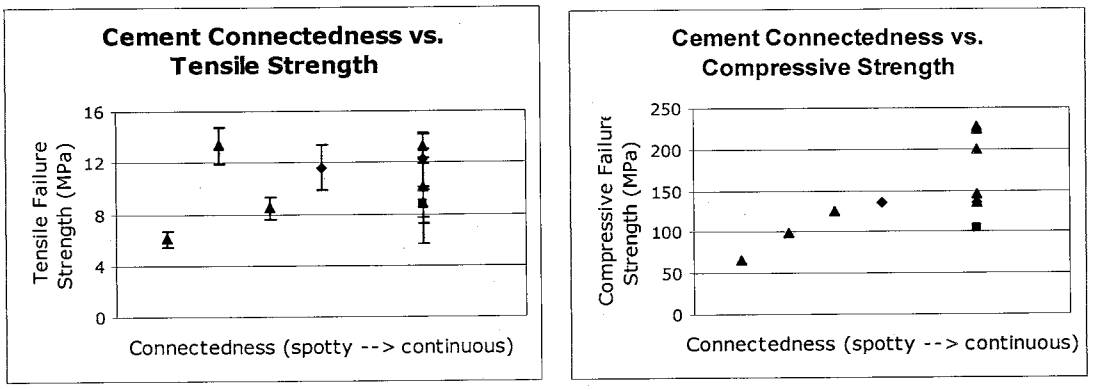

Figure 37: Tensile and compressive failure strength versus the connectedness of the cement that illustrates the general increase in strength with increasing connectedness of the cements.

4.4 SUMMARY: Rock Characterization

The data presented in this chapter covers a broad spectrum of hydrological, mechanical, and physical parameters. This type of characterization allows us to investigate any number of trends that may exist. An analysis and interpretation of the data collected is in Chapter 5.

Chapter 5: Interpretation and Discussion

For the sake of interpretation and discussion, we defined three different categories of possible fracture mechanisms. The conceptual models presented in Chapter 3 were examined in the context of these categories. All three possibilities include observed local flexure as a primary component. The main difference between the categories is the relative role that this flexure plays in fracturing. The categories created and used for this analysis include:

A. "material-controlled" – changes in rock properties control fracturing,

B. "flexure-controlled" – flexure alone controls fracturing,

C. "flexure/pressure-controlled" – a combination of flexure and overpressures control fracturing.

Recall the specific conceptual models developed in this study from Chapter 3. The fracturing in CM#1 (Figure 20) is attributed to elevated fluid pressures in conjunction with local flexure, or "flexure/pressure-controlled"; this model will be addressed in Section 5.3.1. CM#2 (Figure 21) and CM#3 (Figure 22) explore fracturing as a result of structural-induced stresses such as "flexure-controlled"; Sections 5.2.1 and 5.2.2 address these models. Fracturing in all three conceptual models may also be enhanced by differences in physical properties, or "material-controlled."

We examined all observations and data collected during the course of this research project with the ultimate goal of identifying what caused fractures in the DFZ. We investigated a range of potential fracturing mechanisms, with a specific

interest in the role of fluid overpressures, and looked for trends in measured rock properties that may help explain why fractures formed.

For the case of the DFZ, we determined that flexure/pressure-controlled fracturing was the best fit for observed fracturing. This chapter addresses reasons for classifying the DFZ as flexure/pressure-controlled (Section 5.3), as well as discussing the reasons that the other two categories, material-controlled or flexure-controlled, do not apply (Sections 5.1 and 5.2).

5.1 MATERIAL-CONTROLLED FRACTURING

The "material-controlled" category refers to whether the formation of fractures is best explained simply by the variability in rock properties across the DFZ. This category is actually process-based but enhanced by material changes. Changes in rock type or facies are likely to correspond to changes in physical rock strength. A distinct change in rock properties could allow for minor and otherwise unremarkable structural flexure to induce fracturing at this transition. If this were the case in the DFZ, we would expect to see rocks of a critical weakness located in the fault zone. If the same stress was imposed over the entire area, weaker rocks would fracture before others. This pattern in mechanical strength is likely to correspond to a similar trend in other physical properties.

This section (5.1) presents an analysis of our rock characterization in terms of material properties and existing trends. Based on this interpretation, the argument is made that the DFZ fracturing was not material-controlled.

5.1.1 GEOGRAPHICAL TRENDS

Material differences between fractured and un-fractured regions may indicate that the fractures occurred because the rocks were weaker in one area versus

another. Additionally, any pattern across the DFZ may indicate a critical transition that allowed the strains present to fracture the rocks only once that critical value was reached.

Simply stated, weaker rocks are likely to fracture before stronger rocks. In the case of the DFZ, perhaps the facies change across the DFZ provides a transition to a weaker zone. Other rock properties may also play a critical role in fracture processes. The range and distribution of hydrological, mechanical, and other physical properties that were measured throughout the course of this research may lend insight about possible fracture mechanisms. We attempted to identify properties and/or processes important to fracture formation. For example, abundant fluid flow in a discharge area may lead to well-cemented rocks, which may increase brittleness and make strata more prone to fracturing. We also wanted to examine the coupling (correlations) between hydrological, mechanical, and/or other physical parameters. For example, physical grain size may control permeability, which influences the likelihood of fluid pressure buildup and could potentially lead to hydraulic fracturing. Unfortunately, such relationships regarding hydrological parameters could not be fully investigated in this project due to laboratory difficulties (equipment associated with the high pressure permeameter developed unexpected and severe electrical instability problems) and lack of published data.

In the case of the DFZ, a general trend identified from the fieldwork is that of decreasing grain size from north to south. Graphs of particular parameters versus location with respect to the DFZ are illustrated in Chapter 4. Figure 24 plots porosity versus location; Figure 28 is a plot of tensile strengths versus location; Figure 30 plots compressive strength as a function of location with respect to the DFZ. None of these plots demonstrate any apparent qualitative trend. For the sake of quantifying these relationships, R-squared valued were calculated using Microsoft Excel© for

these plots as well as mineralogy and elastic parameters versus location (Table 17, column labeled 'vs. location'). An R-squared value of 1 correlates to a perfect linear relationship between the variables. In this case, no significant trends exist.

5.1.2 PHYSICAL CONTROLS on STRENGTH

Porosity and mineralogy are commonly linked to strength. One might expect to see a decrease in strength as porosity increases, for example. Some mineralogical components (such as quartz) are known to be stronger than others (such as albite), which could influence overall rock strength. Clays are also known to have a strong influence on decreasing sample strength, even if present only in small amounts.

Using the collected data, plots of particular physical parameters versus tensile and compressive strength were plotted and analyzed for any correlation that may

Parameter:	*vs. LOCATION*	*vs. COMPRESSIVE STRENGTH*	*vs. TENSILE STRENGTH*
Porosity	0.0137	0.0000	0.1140
Depth	n/a	0.4355	n/a
Amt. quartz (from XRD analysis)	0.1318	0.0406	0.0049
Calcite (XRD)	0.1252	0.3168	0.3105
Dolomite (XRD)	0.1164	0.3873	0.0240
Ankerite (XRD)	0.1676	0.3571	0.0112
Albite (XRD)	0.0088	0.0097	0.0560
Clay (XRD)	0.1833	0.0037	0.0830
Tensile Strength	0.0166	0.1802	n/a
Comp. Strength	0.1993	n/a	0.1802
Young's Modulus	0.0101	0.2160	n/a
Poisson Ratio	0.4702	0.0394	n/a
Bulk Modulus	0.2453	0.3212	n/a

Table 17: Computed R-squared values for select parameters versus general location with respect to the DFZ, compressive strength, and tensile strength.

exist. Rock strength was plotted versus depth (Figure 31), grain size (Figure 32), rock framework (Figure 34), percent of cement (Figure 36), and connectedness of the cement (Figure 37). No strong trends are evident in the plots except that of increasing compressive strength with decreasing grain size. The likely explanation for this relationship is linked to percent of surface area covered by cement. Smaller grain size provides for a larger surface area per volume of rock. This in turn leads to strengthening grain contacts and the overall rock strength. Calculated values of R-squared for strength versus a number of measured parameters do not indicate any significant trends (Table 17, columns 'vs. compressive' and 'vs. tensile strength').

5.1.3 MICRO- versus MACRO- SCALE TRENDS in rock properties

Scaling issues are an important factor to keep in mind, especially with this particular rock characterization. As countless previous researchers have pointed out, measurements of the same parameter may vary by orders of magnitude depending on the scale at which it is evaluated (Figure 38). Permeability is commonly the topic of interest in many of these studies. Such investigations include but are not limited to Bredehoeft et al. (1983), Willett and Chapman (1987), Neuzil (1994), Garven (1995), and McPherson et al. (2001). It is not always clear which scale is appropriate to use when evaluating and quantifying water resources, calibrating models, or testing hypotheses in general.

Macro-scale trends may likely control where fractures form. As discussed previously, a general trend of decreasing grain size from north to south across the DFZ was noted in the field. Grain size is likely to be a proxy for permeability, which is known to influence the ability of fluid overpressures to develop. The possibility exists that this trend provides some transition and critical value of permeability at which fluid pressures can increase to an amount significant enough to induce

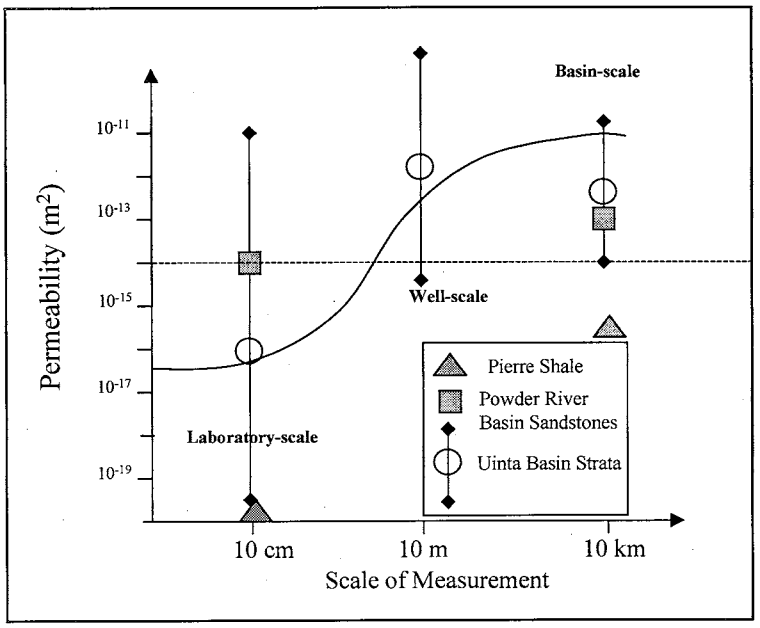

Figure 38: Effect of scale on permeability as illustrated by examples from three sedimentary basins; Uinta Basin, Utah (Willett and Chapman, 1987); Powder River Basin, Wyoming (McPherson et al., 2001); Pierre shale, South Dakota (Bredehoeft et al., 1983 and Neuzil, 1994); Dashed line indicates average crustal permeability from Brace, 1980; Error bars apply to Uinta Basin only; Figure modified from McPherson et al., 2003.

fracturing in the rocks.

Micro-scale trends influence and may control physical rock strength. In the case of the DFZ and this study, surface area covered by cement appears to be the strongest correlation to physical failure strength of the samples measured. This is likely to be related to historical fluid flow in the area, which may have transported the calcite in solution to precipitate, as well as providing a mechanism to coat the grains.

It is important to keep in mind that point measurements, such as the samples collected from the DFZ and vicinity, are not necessarily representative of the system as a whole. Caution should be used when analyzing the data for trends since inherent heterogeneity within the system may distort measurement results. With

this in mind, however, it is still likely that larger-scale trends would be evident in point measurements.

5.1.4 SUMMARY: Material-controlled fracturing

No major geographical trends are evident in the DFZ rock characterization and property data. We realize that this lack of trend may be due to not enough data. Because the DFZ is a transition area, sampling may be simply incomplete, and not able to capture the true character of the fault zone. If any significant trends exist, however, some indication of the trend(s) would likely be reflected in the data to some extent.

Given that we observe no data trends to suggest a material-controlled fracturing mechanism, we turn our attention to our two other suggested categories of fracture mechanism for the DFZ, "flexure-controlled" and "flexure/pressure controlled."

5.2 FLEXURE-CONTROLLED FRACTURING

"Flexure-controlled" refers to the possibility that rocks in the DFZ are sufficiently weak such that the very mild local flexure alone could have induced fractures. Intense fracturing without a marked contrast in rock properties would require sufficient flexure and increased strain. The anticline documented by Groeger and Bruhn (2001) spans the DFZ almost exactly. The difference between this category and the previously discussed material-controlled is that in this case, the location of fracturing is controlled by the induced strain of the flexure rather than by the weakness associated with the facies change. Two of the three competing conceptual models (CM#2 and CM#3) described in Chapter 3 fall into this category.

This section (B) specifically examines these two cases and presents reasons why flexure-controlled fracturing does not appear to be a good explanation for the DFZ. Particular flaws or unanswered questions in each model are pointed out.

5.2.1 REASONS CM#2 CANNOT EXPLAIN the DFZ

The anticline that spans the DFZ is the principal cause of the fractures for the case of the extension–anticline model, or CM#2 (Chapter 3, Figure 21). Considering this mechanism alone does not explain why other anticlines in the area do not show the intense fracturing we see in the DFZ. In this study, local flexure is mapped (Figure 39) and calculated slope values are tabulated (Table 18); data used for this analysis were formation top data from Petroleum Info (McPherson, 2004, written communication). The propensity for fracturing should be similar in cases of comparable flexure, facies or rock type, and geological history. These other anticlines are of slightly larger magnitude and are located in the Uinta Fm only 800–3,200 m (0.5–2 miles) south of the DFZ. However, they are not fractured to the same degree as the strata in the DFZ.

The material properties testing established no mechanical strength difference for the case of the rocks in the DFZ and vicinity. It seems highly unlikely that local flexure would cause such intense fracturing in one area, while a slightly larger flexure in a nearby area would show no visible effects. The fact that the two un-fractured anticlines have greater flexure than the fractured DFZ anticline implies that an additional process must have occurred to initiate the fractures. Additionally, subtle local flexure does not explain the presumed cyclic nature of calcite precipitation in the fractures. Flexure of this (subtle) magnitude would not typically produce recurring fracturing.

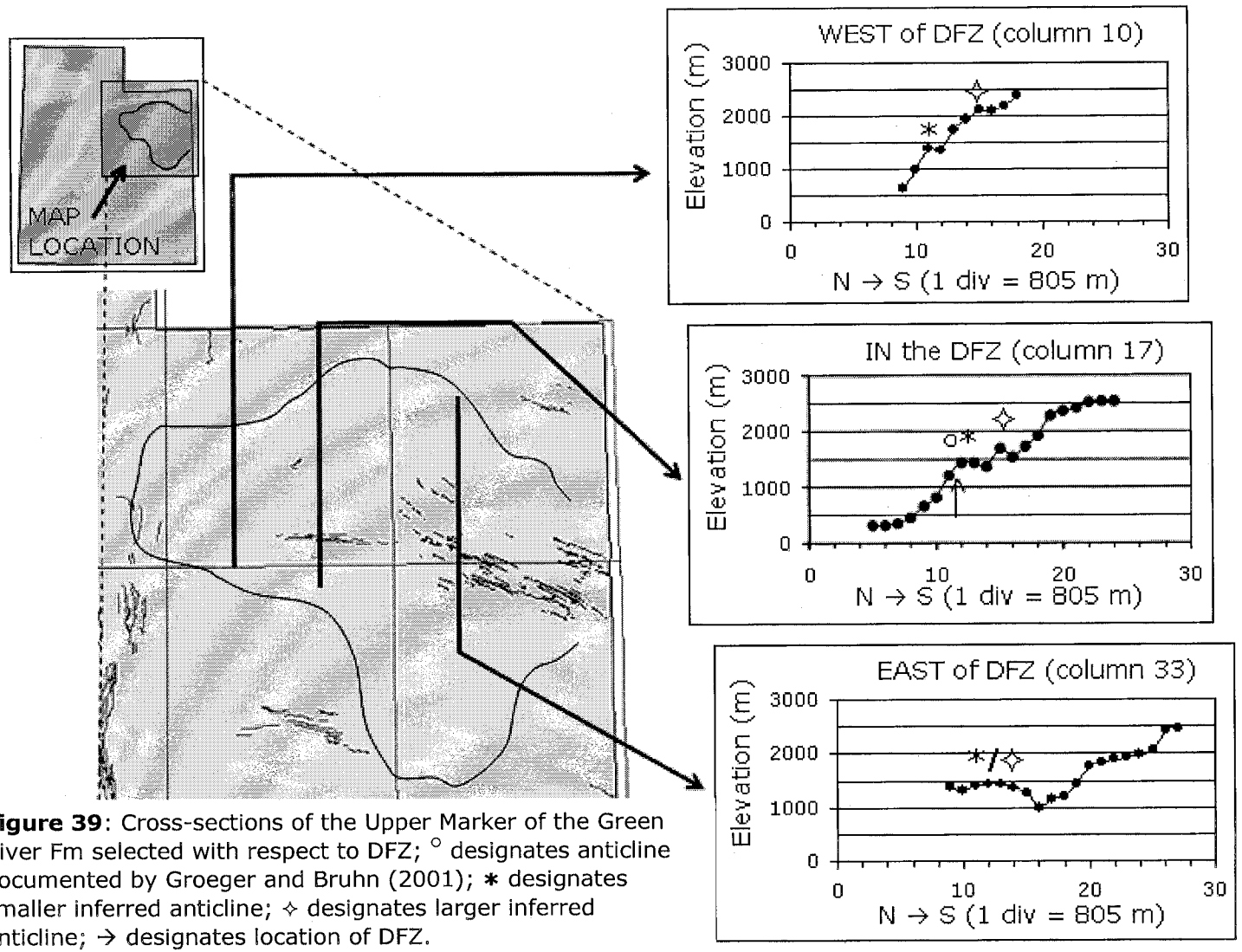

Figure 39: Cross-sections of the Upper Marker of the Green River Fm selected with respect to DFZ; ° designates anticline documented by Groeger and Bruhn (2001); ∗ designates smaller inferred anticline; ✧ designates larger inferred anticline; → designates location of DFZ.

KEY:	DFZ									
	smaller inferred anticline						slope >0 : N dip			
	larger inferred anticline						slope <0 : S dip			

Location with respect to DFZ →		west of FZ	slightly west of FZ	in FZ	in FZ	in FZ	eastern FZ	eastern edge of FZ	slightly east of FZ	east of FZ	eastern edge of UB
Dist. E or W of town of Duchesne (m) →		WEST 4830 column 10	2415	0	805 column 17	1610	4830	7245	10465	13685 column 33	EAST 18515
Distance N or S of DFZ (m) ↓											
NORTH	8050						-0.138				
	7245						-0.086				
	6440					0.236	0.037				
	5635					-0.124	0.075	-0.048			
	4830			-0.037	0.000	0.000	0.124	-0.248			
	4025			0.037	0.037	0.161	0.287	0.037	0.094		
	3220		-0.019	0.124	0.124	0.124	0.123	0.000	-0.019		
	2415		0.267	0.267	0.267	0.267	0.143	0.143	0.267		
	1610	0.429	0.393	0.193	0.193	0.193	0.317	0.193	-0.180	-0.099	
	805	0.498	0.497	0.497	0.497	0.373	0.373	0.497	0.373	0.124	
DFZ	0	**-0.062**	**0.025**	0.273	0.273	0.273	0.149	0.273	0.149	0.025	-0.124
	805	0.497	0.124	**0.000**	**0.000**	0.124	0.373	0.248	0.236	0.000	0.137
	1610	0.248	0.286	0.037	**-0.087**	**-0.087**	**-0.087**	**-0.087**	**-0.075**	**-0.087**	**-0.335**
	2415	0.224	0.286	0.286	0.410	0.286	0.037	0.037	0.037	**-0.112**	0.435
	3220	*-0.012*	*-0.236*	*-0.087*	*-0.199*	*-0.075*	*-0.224*	*-0.410*	*-0.519*	*-0.337*	*-0.435*
	4025	0.112	0.261	0.124	0.248	0.124	0.248	0.211	0.147	0.188	0.174
	4830	0.248	0.199	0.360	0.236	0.236	0.112	0.224	0.087	0.075	-0.634
	5635		0.385	0.360	0.435	0.522	0.410	0.161	0.248	0.273	0.174
	6440		-0.174	-0.099	0.112	0.075	0.099	0.037	0.410	0.398	0.857
	7245		0.037	0.360	0.075	0.075	0.000	0.000	0.161	0.087	0.124
	8050			0.037	0.112	0.149	-0.075	0.149	0.037	0.075	0.037
	8855			0.037	0.037	-0.037	-0.037	0.000	0.075	0.037	0.075
	9660			0.000	0.000	0.037	0.000	0.075	0.037	0.075	
	10465					0.075	0.037	0.087	0.037	0.112	
	11270						-0.124	0.112	0.335	0.447	
SOUTH	12075						0.199	0.000	0.000	0.037	

Table 18: Calculation of slope (in vertical m / horizontal m) for selected N-S sections in the Uinta Basin; emphasis is placed on the DFZ (in box) and inferred anticlines from well data (smaller, northern anticline in bold text; larger, southern anticline in italics and shaded in gray); recall the anticline documented by Groeger (1997) corresponds to the DFZ.

5.2.2 REASONS CM#3 CANNOT EXPLAIN the DFZ

The conceptual model that considers fractures unrelated to high fluid pressures, CM#3 (Chapter 3, Figure 22), also leaves a number of unanswered questions. Recall that this model suggests the DFZ formed due to regional stresses and/or local flexure before and independently of high fluid pressures. Fluid pressures south of the DFZ could dissipate through the fractures, and therefore could not be maintained south of the DFZ. Considering this mechanism alone does not explain the presumed multiple generations of calcite growth that are observed from the field.

Furthermore, this conceptual model does not explain a mechanism that could have fractured the DFZ without affecting the nearby areas, similar to that discussed in the previous section. We assume that if regional stresses and/or local flexure led to fracturing, an area larger than the present-day DFZ would have been affected. If CM#3 was applicable to the DFZ and initial fractures formed due to regional stresses and/or local flexure, another mechanism(s) would be necessary to explain subsequent generations of fracturing.

5.3 FLEXURE/PRESSURE-CONTROLLED FRACTURING

The category of "flexure/pressure-controlled" accounts for observed elevated fluid pressures in the vicinity which terminate at the DFZ boundary. These elevated fluid pressures are thought to have reduced effective stress in the area so that the propensity for strain and subsequent fracturing is increased. For the case of the DFZ, we believe that CM#1, which falls into the category of flexure/pressure-controlled, is the most reasonable explanation for the fractures. The discussion that follows in this section (5.3) outlines reasons that support this argument. A brief

overview of numerical simulations (done by McPherson, 2004) as an additional analyses is also presented.

5.3.1 CM#1: A CONSISTENT MODEL for the DFZ

The high fluid pressures / fault value model, or CM#1 (Chapter 3, Figure 20), provides a conceptual framework for reduced effective stresses and increased strains. In this model, fractures would not have formed without overpressure buildup. Petrographic and fluid inclusion analysis by Hulen concluded that multiple growths of calcite exist in single fractures in the Balcron area, and that the different generations possess different paleo-temperatures. Field observations from this study observed fractures of different orientations at a single location that possessed different fill (recall Figure 16). These observations imply that conditions changed throughout the history and formation of the DFZ, or that a "cycle" of fracturing and subsequent healing must have taken place. CM#1 explains this presumed cyclic nature of cements remnant in the system through a type of fault valve behavior.

We do not have evidence that definitively proves that high fluid pressures were the fracturing mechanism. Evidence of this type may not exist, since distinguishing between pressure conditions at the time of fracturing and at the time physical remains (such as calcite precipitation) are deposited in the system may be impossible. Based on the data we collected, this CM#1 model seems reasonable as it accounts for all field evidence and observed rock properties. At the least, we found no evidence to disprove this particular hypothesis of hydraulic fracturing.

5.3.2 NUMERICAL MODELING

We developed and conducted numerical models of coupled fluid flow and poroelastic strain, to provide a quantitative test of the flexure/pressure-controlled

fracturing mechanism. Results of these models suggest that fluid overpressures definitively increase the propensity for strain, which is to be expected. Details of this analysis are in the form of a separate manuscript submitted to Geophysical Research Letters (McPherson and Smith, to be submitted June 2004).

5.4 SUMMARY and CONCLUSIONS

With sufficiently low rock permeability, fluid pressures are more inclined to build up, reducing effective stress and increasing the propensity for fractures to form. If fluid pressures exceed the least principle stress, no additional stress (referring to structural flexure in the specific case of the DFZ) would be required for fracturing. The overpressure models of McPherson and Bredehoeft (2001) suggest that such high pressures were possible in the area north of the DFZ. It is likely that these overpressures were just high enough to reduce the effective stress and permit the mild flexure present in the area to induce fracturing. Pressure-driven fluid flow through the fault zone may have permitted calcite cement precipitation as calcite-saturated fluids encountered lower partial pressure of CO_2. Areas south of the DFZ did not fracture because pressures escaped locally through the fault zone. Ultimately, we hypothesize that a recurring cycle developed that included: 1. fluid pressure buildup, 2. fracturing, 3. fluid flow through the fractures and fault zone, 4. calcite precipitation, 5. subsequent sealing of fracture permeability, then 1-5 again, etc. (refer to Figure 20).

Five specific hypotheses were presented in Section 1.3. The following addresses each of these individually:

(1) *Original Hypothesis*: The rocks in the DFZ are mechanically different than those outside of the DFZ.

Results: The rocks in the DFZ are not mechanically different than those outside of the DFZ. Our characterization did not find the existence of any geographical trends in porosity, mechanical strength, or mineralogy between the fractured and unfractured zones in the DFZ and vicinity. A trend of decreasing grain size from north to south across the fault zone is likely to correspond to permeability.

(2) *Original Hypothesis*: Hydrologic properties influence the mechanical strength or response of rocks.

Results: There is no apparent correlation between hydrologic properties and the mechanical strength (or response) of rocks based on the data we collected. This possibility was not explored to its full potential due to laboratory equipment problems associated with permeability measurements, however. Grain size decreases from north to south across the DFZ. Knowing that grain size is often a proxy to permeability, some critically low value of permeability likely occurs at the DFZ, which leads to an increased propensity for fluid pressure buildup.

(3a) *Original Hypothesis*: DFZ fracture formation is attributed to local flexure aided by abnormally high fluid pressures.

Results: For the case of fracturing in the DFZ, fracture formation due to local flexure aided by abnormally high fluid pressures is the best-fitting explanation. No specific evidence to disprove this hypothesis could be found. Furthermore, the observations made and data collected supports this hypothesis.

(3b) *Original Hypothesis*: DFZ fracture formation occurred due to local flexure only and (3c) *Original Hypothesis*: DFZ fracture formation occurred before high fluid pressures due to local flexure, regional extension, and/or unloading.

Results: The conceptual models that explore fracture formation due to local flexure only and fracture formation before high fluid pressures do not explain all

observations made in the field and the resulting trends from the rock characterization.

In the case of the Duchesne Fault and Fracture Zone in the Uinta Basin in northeastern Utah, we conclude that anomalously high fluid pressures and low permeability are crucial to fracture development. Without such fluid pressures, we contend that the intense fracturing observed would not have occurred. The most important conclusions of this project include:

1. No distinct trends in material properties exist across the DFZ despite a trend of decreasing grain size from north to south.
2. Fracturing was probably controlled by a locally-induced stress, such as local flexure or an area of overpressure.
3. Other nearby anticlines are not intensely fractured; it is not probable that the DFZ anticline alone caused the intense fracturing.
4. No evidence against the case of high fluid pressure induced fracturing was found. The observations made and data collected suggest that fluid pressures most likely played a crucial role in the DFZ fracturing.

These findings are a significant contribution to the overall study of the DFZ. Initial goals of this research included investigation of the mechanisms involved in DFZ fracturing with the specific consideration of hydraulic fracturing and providing a baseline of data including properties of the Uinta Fm and in the vicinity of the DFZ. The developed conceptual model considers how high fluid pressures likely played a role in the fracturing, and also suggests that the intense fracturing would not have formed without these high fluid pressures. This theory has been the speculation among many researchers that work specifically in the area for some time, but until this study had not been investigated in detail. The rock characterization provides an extensive baseline data set for the Uinta Fm and for the fractures rocks in the vicinity

of the DFZ. Mechanical data of this sort did not exist previously, and is necessary for any farther investigation in this area.

These goals and conclusions are relevant on a larger scale and can be applied to basins with similar conditions elsewhere. Additionally, this research should be used to introduce an investigation of the possibility of hydraulic fracturing in basins where the necessary conditions may exist even if another, perhaps simpler explanation also exists.

Chapter 6: Recommendations for Future Work

The data assembled and analyses performed during this research project are meant to serve as a basis for evaluating the cause of fracture formation in the DFZ and the role that high fluid pressures may play in fracturing in general. Results suggest that high fluid pressures were necessary to create the intense degree of fracturing observed in the DFZ. No evidence was found to disprove this hypothesis. However, a few uncertainties remain. The following discussion serves to present these ambiguities (*problem*) and suggest a method for clarification (*recommendation*). Any or all of these could provide invaluable additional insight on the overall history of the DFZ and the role of fluids in geologic fracturing.

6.1 *Problem*: Geographical trends in physical properties may exist, but may not have been identified due to lack of data. The spatial distribution used in this study had the majority of samples located in the western DFZ (recall Figure 5). *Recommendation*: Collect additional samples from the DFZ and vicinity and perform a similar rock characterization. Due to the spatial distribution used in this study, focus should be placed on obtaining some samples from new locations outside the DFZ, especially from the east and south of the DFZ. Samples should be also be collected from areas similar to this study; this will augment the data set and clarify the (lack of) trends observed in the current data set. Consideration should also be given to measurement of parameters planned but not completed as part of this research study, specifically permeability.

6.2 *Problem*: In this study, the existence and location of minor anticlines in the area was determined from well data. Such data are not always reliable. The approach for mapping and analyzing these 3-dimensional structures used a high density of wells in an attempt to counteract the lack of precision associated with formation tops picked from well data (McPherson, personal communication, 2004).

Recommendation: Another approach to this analysis would be a detailed mapping of strike and dip in the suspected areas of flexure south of the DFZ. This work should be similar to the work done by Groeger (1997) in the Duchesne Graben and anticline area and could provide a better constraint on location, extent, and amplitude. Because of the small amplitude of these features, manual mapping and personal attention is probably the best approach to yield significant results.

6.3 *Problem*: It doesn't seem reasonable that an anticline of small amplitude (such as that in the Duchesne Graben area) would be able to result in intense fracturing.

Recommendation: An obvious approach to this uncertainty is searching for other documented anticlines of comparable amplitude. This is a difficult task, however, since flexures this minor are not usually mapped. Additionally, unless the amplitude is of the exact magnitude, in the exact rock type, and has experienced an exact geologic history including amount of overburden removed, there is still some degree of uncertainty that would remain.

6.4 *Problem*: Comparable anticlines in the area should show similar fracturing if the local flexure is responsible for the fracturing. This premise assumes that the anticlines have similar material properties.

Recommendation: The assumption of no significant difference in rock properties could be tested by performing a detailed characterization of the strata from other

anticlines in the area. Detailed observations of facies and rock types would also be beneficial.

6.5 *Problem*: Cements were determined to be a significant control on mechanical strength in this investigation. The fine grain size did not allow for an analysis to the precise degree of differentiation that may be necessary (between "fine" and "very fine", for example), nor were we able to conclude cement type with a high degree of confidence due to improper sample preparation.
Recommendation: Backscattered electron images could be used to produce a chemical map of the sample surface. Determination of exact cement type and location would be possible due to the small scale capabilities of the electron microprobe.

6.6 *Problem*: Definitive documentation that high fluid pressures were/are present in the DFZ does not exist. Published studies that refer to high fluid pressures in the area usually are focused to the north of the DFZ and rely on personal accounts of well blowouts or high values of head as observed from wells.
Recommendation: Fluid inclusion analysis may be able to determine paleo-conditions, including temperature and pressure, at the time of calcite precipitation in the fractures. The conditions at the time of precipitation were not necessarily the same conditions at the time of fracturing. However, documentation that high fluid pressures were present or passed through the DFZ at some time in history would be significant. Different paleo-conditions in the layers of calcite would support multiple generations of precipitation.

6.7 *Problem*: Although relative timing of some events related to the DFZ have been determined, quantitative ranges are not certain.

Recommendation: Calcite from fractures may be dated, although it is not clear whether or not it would be successful. A detailed investigation of cross-cutting relationships may lead to better relative age dating.

6.8 *Problem*: Whether the DFZ fractures formed at the surface or at some depth is not definite. If the DFZ did form at depth, mechanical behavior at the time of fracturing may have been significantly different than what is now tested in the laboratory from surface samples.

Recommendation: The total amount of overburden removed has been determined for a number of areas in the Uinta Basin. This information may be useful if we could establish the relative timing of certain events with more precision. Buried rocks have an additional confining stress of the weight of the rocks above it, and may be less prone to fracturing. If it is the case that the DFZ formed at depth, it is recommended that samples should be located from laterally equivalent units occurring at depth and characterized to investigate how the properties vary with increasing depth.

6.9 *Problem*: The presumed cyclic precipitation in of fracture-filling calcite is not firsthand data.

Recommendation: Completion of the fluid inclusion analysis in progress can support the interpretation of different conditions in the layers of calcite. Additionally, more fracture-filling calcite veins should be collected from the field, with particular caution placed on keeping the wallrock intact.

6.10 *Problem*: A very weak and indistinct geographical trend in albite occurrence was identified in the XRD analysis labwork, but no similar trend existed in the petrographic analysis.

Recommendation: Collect additional samples from the DFZ and vicinity and perform a similar mineralogical analysis. Additional, field notes relating specifically to mineralogy and rock type as observed in the field should be taken.

Appendix I: Sample Summary and Description

The table in this appendix lists all of the samples collected from the Uinta Basin, Utah field trip. The column headings are explained below:

Samp#: gives the sample number; UB denotes those samples collected from the Uinta Basin from surface outcrops, along with an arbitrary number for identification; A_ denotes those samples donated to the project by Amoco, along with a number which corresponds to the depth at which they were located.

Loc'n: gives the general location name of where the samples were located. These locations are commonly referred to in the text. **Lat** (°N)**/Long** (°W): given in degrees and minutes.

Fig#: gives numbers of figures within the main text of pictures corresponding to sample locations.

Poro (porosity)**, Ten** (tensile)**, Comp** (compressive)**, XRD** (x-ray diffraction)**, SEM** (scanning electron microscope)**, TS** (thin sections): for those samples where this particular parameter were measured, the *sample number* is listed; these numbers correspond to the results as reported in the main text.

Brief Description: gives a very general description of the sample.

Samp #	Loc'n	Lat/Long °N, °W	Fig#	Poro	Ten	Comp	XRD	SEM	TS	Description
UB 1	Balcron oil field	40° 06.099′ 109° 57.482′	11 12 17							gilsonite in sandstone
UB 2	Balcron oil field	40° 06.099′ 109° 57.482′	11 12 17							calcite vein; used for fluid inclusion analysis
UB 3	Balcron oil field	40° 06.099′ 109° 57.482′	11 12 17							calcite vein; used for fluid inclusion analysis
UB 4	Balcron oil field	40° 06.099′ 109° 57.482′	11 12 17							calcite vein; used for fluid inclusion analysis
UB 5	Balcron oil field	40° 06.088′ 109° 57.368′	11 12 17							misc samples (mound)
UB 6	Balcron oil field	40° 06.088′ 109° 57.368′	11 12 17							misc samples w/ gilsonite (mound)
UB 7	Balcron oil field	40° 06.088′ 109° 57.368′	11 12 17				7			gilsonite
UB 8	Balcron oil field	40° 06.088′ 109° 57.368′	11 12 17							calcite (mound)
UB 9	Balcron oil field	40° 05.822′ 109° 57.038′	11 12 17							slickenslides, fault fill, gilsonite in calcite, broken plug, typical piece of sandstone
UB 10	Balcron oil field	40° 05.822′ 109° 57.038′	11 12 17							taken through calcite fault fill
UB 11	Balcron oil field	40° 05.822′ 109° 57.038′	11 12 17							plug through fault fill
UB 12	Balcron oil field	40° 05.822′ 109° 57.038′	11 12 17	12						
UB 13	Balcron oil field	40° 05.822′ 109° 57.038′	11 12 17							plug through sandstone
UB 14	Balcron oil field	40° 05.822′ 109° 57.038′	11 12 17	14, 14A			14			
UB 15	Balcron oil field	40° 05.822′ 109° 57.038′	11 12 17	15-3					UB 015	

Samp #	Loc'n	Lat/Long °N, °W	Fig#	Poro	Ten	Comp	XRD	SEM	TS	Description
UB 21	Wells Canyon	40° 06.112′ 109° 57.911′	8 13 14	21A	21-T1 T2 T3 T4	21D	21	21	UB 021	
UB 22	Wells Canyon	40° 05.736′ 110° 10.427′	8 13 14	22D	22-T1 T2 T3 T4 T5 T6 T7	22E 22F	22		UB 022	
UB 23	Wells Canyon	40° 05.736′ 110° 10.427′	8 13 14	23		23B	23		UB 023 x2	
UB 24	Wells Canyon	40° 05.736′ 110° 10.427′	8 13 14	24, 24B					UB 024	
UB 25	Wells Canyon	40° 05.736′ 110° 10.427′	8 13 14	25A						
UB 26	Wells Canyon	40° 05.736′ 110° 10.427′	8 13 14	26B	26-T1 T2 T3	26A 26C	26	26	UB 026 x2	
UB 27	Duchesne Graben	40° 07.692′ 110° 28.855′		27A	27-T1 T2	27D	27		UB 027 x2	dips to S
UB 28	Duchesne Graben	40° 07.692′ 110° 28.855′		28					UB 028	dips to N (?)
UB 29	Duchesne Graben	40° 07.692′ 110° 28.855′								calcite pieces in float
UB 30	Duchesne Graben	40° 07.692′ 110° 28.855′								calcite crystals
UB 31	Duchesne Graben	40° 07.799′ 110° 27.501′	15	31B	31-T1 T2 T3 T4 T5	31A 31C	31	31	UB 031	
UB 32	Duchesne Graben	40° 07.903′ 110° 21.985′	16							calcite crystals with gilsonite
UB 33	Duchesne Graben	40° 07.903′ 110° 21.985′	16	33A					UB 033	
UB 34	Duchesne Graben	40° 07.903′ 110° 21.985′	16							

Samp #	*Loc'n*	*Lat/Long °N, °W*	*Fig#*	*Poro*	*Ten*	*Comp*	*XRD*	*SEM*	*TS*	*Description*
UB 35	north of FZ	40° 09.764' 110° 23.384	9	35B	35-T1 T2 T3 T4	35A	35	35	UB 035	
UB 36	north of FZ	40° 09.764' 110° 23.384	9							cementation/ mineralized coating
UB 37	north of FZ	40° 09.764' 110° 23.384	9	37-1						
UB 38	south (IN) of FZ; Indian Canyon Rd	40° 07.543' 110° 26.510'	7							chertified limestone
UB 39	south (IN) of FZ; Indian Canyon Rd	40° 07.543' 110° 26.510'	7	39A	39-T1 T2 T3 T4 T5 T6 T7 T8 T9	39B	39	39	UB 039	
UB 40	south of FZ; Indian Canyon Rd	40° 06.280' 110° 28.233'		40B		40H	40	40	UB 040	
UB 41	south of FZ; Indian Canyon Rd	40° 06.280' 110° 28.233'		41B	41-T1 T2	41A	41	41	UB 041	
UB 42	north of FZ	40° 11.210' 110° 31.168'	10							
UB 47	north of FZ	40° 11.210' 110° 31.168'	10							
UB 48	north of FZ	40° 10.833' 110° 31.771'		48A	48-T1 T2 T3 T4	48B 48C	48	48	UB 048	
A_ 4645	Broadhurst (NE)			A_ 4645A A_ 4645B A_ 4645C		A_ 4645A A_ 4645B A_ 4645C				
A_ 4672	Broadhurst (NE)			A_ 4672A A_ 4672B		A_ 4672A A_ 4672B				

Samp #	Loc'n	Lat/Long °N, °W	Fig#	Poro	Ten	Comp	XRD	SEM	TS	Description
A_ 4712	Broadhurst (NE)			A_ 4712A A_ 4712B A_ 4712C A_ 4712D A_ 4712E A_ 4712F		A_ 4712A A_ 4712B A_ 4712C A_ 4712D A_ 4712E A_ 4712F			BH 1 BH 2 BH 3 BH 4 --- ---	
A_ 4743	Broadhurst (NE)			A_ 4743A A_ 4743B		A_ 4743A A_ 4743B			BH 5 BH 9	
A_ 4774	Broadhurst (NE)			A_ 4774A A_ 4774B A_ 4774C		A_ 4774A A_ 4774B A_ 4774C				
A_ 5320	Broadhurst (NE)			A_ 5320A A_ 5320B A_ 5320C		A_ 5320A A_ 5320B A_ 5320C				
A_ 8569	Smith-Emory (NW)			A_ 8569						
A_ 8602	Smith-Emory (NW)			A_ 8602		A_ 8602				
A_ 10157	Smith-Emory (NW)			A_ 10157		A_ 10157				
A_ 10168	Smith-Emory (NW)			A_ 10168		A_ 10168				
A_ 10171	Smith-Emory (NW)			A_ 10171 A		A_ 10171A A_ 10171B				
A_ 10176	Smith-Emory (NW)			A_ 10176 A		A_ 10176A A_ 10176B				
A_ 11030	Smith-Emory (NW)			A_ 11030		A_ 11030				
A_ 11055	Smith-Emory (NW)			A_ 11055						

Appendix II: Lab Procedures for Rock Properties Testing

This manual was developed along with the laboratory work that accompanied this research. Previously, a manual of this type did not exist for rock properties testing in the Rock Mechanics and Properties laboratory. The purpose of such a manual is to provide a guide to standard and accepted methods for rock properties testing in the Rock Mechanics Laboratory at New Mexico Tech.[2]

Outline:

I. General Laboratory Descriptions

Rock Mechanics and Properties Laboratory

X-Ray facility

II. Laboratory Safety

III. Porosity Measurements: Stereopycnometer

IV. Load Cell Calibration (Triaxial Tests)

V. Brazil (Indirect) Tensile Strength Measurements: Triaxial Machine

VI. Uniaxial Compressive Strength Measurements: Triaxial Machine

Glossary for compressive tests

VII. Mineral Identification: X-Ray Diffraction (XRD)

[2] General references used for this manual include: Bieniawski, Z. T. and and I. Hawkes , 1978; Boutt, 2002, personal communication; Chen et al., 1998a and 1998b; Gunsallus and Kulhawy, 1984. See thesis references for details.

I. *General Laboratory Descriptions*

The Rock Mechanics and Properties Laboratory (RML) at New Mexico Institute of Mining and Technology has the capabilities to measure rock properties as well as hydrological parameters at elevated confining pressures. This laboratory was built and developed at CONOCO and brought to New Mexico Tech by Larry Teufel of the Department of Petroleum Engineering who formerly ran the laboratory. The lab has one four pole loading frame capable of delivering up to 1.3 MN of force at strain rates ranging from 10^{-2} to 10^{-8} s^{-1} (Figure 1). These loads are applied to a pressure vessel that accepts a 1.9-cm diameter and 3.8-cm length sample. A maximum of 400 MPa confining fluid pressure is delivered to the pressure vessel via a hydraulic accumulator and intensifier. Together these instruments compose what we call our "Triaxial Deformation Rig". The rock strains are measured using Vishay Micro-Measurements Group strain gages (oriented parallel and normal to the maximum stress direction) and Schaevitz LVDTs at 0.100", 0.500", and 2.00" sensitivities. Strain gage output is fed through a Vishay Series 2100 10 channel strain indicator and post processed using a Pentium II class workstation installed with a National Instruments 4351 16-channel data acquisition card. Pore pressures are generated with a Sprague-Teledyne air over oil pump

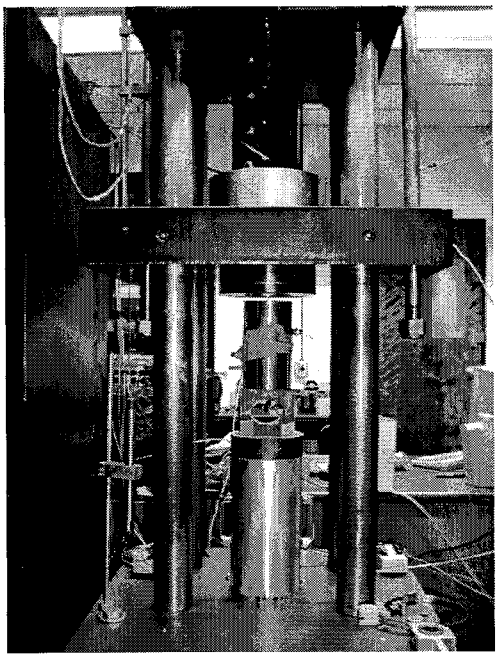

Figure 1: NMT's four pole loading frame setup for a Brazil test.

coupled with a Superpressure Inc. double acting circulating pump capable of generating 276 MPa of pore pressure. Pore pressure measurements are made with two Setra Datum 2000 pressure transducers and transmitters with ports located at the top and the bottom of the rock sample. Compressibility measurements are made with using the method described in Sampath (1982) with a Temco 70 MPa positive displacement pump and a Validyne 1 MPa differential pressure transducer. An optional Thermacraft ceramic furnace is available for raising the temperature of the pressure vessel up to 400 °C. Data is logged from all instruments through the National Instruments card using the National Instrument software LABVIEW.

The X-Ray facility at The New Mexico Bureau of Geology and Mineral Resources (NMBGMR) provides mineralogical/crystallographic analyses of solid materials by X-ray diffraction (XRD).

II. *Laboratory Safety*

In most cases, common sense is sufficient for laboratory safety in the RML. However, a few particular cautions are mentioned below.

1. Safety glasses should be worn while drilling and while running uncontained tests (i.e., Brazil tests) in the triaxial machine.
2. Close-toed shoes should be worn at all times.
3. A dust mask should be worn when working at times when large amounts of rock dust is present (i.e., facing samples).
4. A mask when soldering is optional but a good idea, since lead fumes are given off during the process. Good ventilation is also recommended.

The XRD Laboratory is a separate laboratory, and therfore has a different se tof safety procedures. These will be be explained in detail by the laboratory manager.

III. *Porosity Measurements: Stereopycnometer*

Theory: This method is particularly useful since you can use irregularly shaped samples. The pycnometer uses a pressure change and the Ideal Gas Law to calculate the volume added (the sample) to a chamber of known volume. In addition to the pycnometer measurements, the dry and saturated weights of the sample are also measured.

We use the basic principle that porosity is the ratio of the volume of voids to the total volume and the total volume is equal to the solid volume (grains) plus the volume of voids. Additionally we assume that when the sample is saturated all of the voids are filled with water.

Procedure:

1. Gather samples
2. Record original weight
3. Saturate samples:
    a. Wet cloth/paper towel on bottom of vacuum (Room 393)
    b. Place samples in vacuum
    c. Spray with water
    d. Leave in vacuum for 24 hours
4. Record saturated weight
5. Dry samples:
    a. Place samples in oven at 105° (outside Room 158)
    b. Leave for 24+ hours
6. Record dry weight
7. Pycnometer measurements (Room 158)

a. Turn on He-gas tank

i. OPEN gray valve on the tank

ii. OPEN valve that controls flow to the pycnometer (this is the leftmost valve)

b. Turn ON pycnometer

c. Let machine warm up for 10-15 minutes

Where to have controls:

i. VENT ∇

ii. CELL VENT CONTROL slightly open

iii. V_A IN

iv. FLOW Δ

v. FLOW CONTROL slightly open

You should see some slow bubbling from the end of the tube if placed in a beaker of water

d. Running samples:

i. Carefully place sample in chamber

ii. Screw lid on tightly; make sure white arrows are lined up

iii. Purge sample:

1. Open flow- FLOW Δ
2. close CELL VENT CONTROL (turn right)
3. Open cell vent- VENT ∇
4. Get reading to 17 or 18 psi (This is what it will go to on its own; you can control the speed by opening FLOW CONTROL). If you can't get the pressure to 17, open larger valve on the gas tank.
5. Wait 5-15 minutes, or until pressure is changing <0.001 psi in about 20 seconds

iv. Close flow- ON-OFF∇

v. Open CELL VENT CONTROL (turn left); pressure should go to 0

vi. Close cell vent- CELL Δ

vii. V_A OUT

viii. Zero the pressure if necessary, by turning knob on top screen

ix. Open flow- FLOWΔ

x. Get pressure to 17-20 psi by turning FLOW CONTROL

xi. Turn flow off when pressure reaches 17-20 psi- ON-OFF ∇

xii. Record P (This is P2)

xiii. V_A IN

xiv. Record P (This is P3)

xv. Close CELL VENT CONTROL (turn right)

xvi. Open cell vent- VENT ∇

xvii. Slowly open CELL VENT CONTROL (turn left)

xviii. P should drop

xix. Open chamber and remove sample

e. Close valves on gas tank

f. Turn off pycnometer

8. Calculate porosity (n) using saturated weight (W_{sat}), dry weight (W_{dry}), P2, P3 and the following equations (all of these equations have been entered into a spreadsheet which calculates porosity given W_{sat}, W_{dry}, P2, and P3):

a. Volume of water (V_w); Density of water (ρ_w)*

$$V_w = (W_{sat} - W_{dry}) / \rho_w$$

*For most cases, you can assume that ρ_w = 1 g/mL = 1 g/cm^3

b. Volume of sample (grains) determined by pycnometer (V_s)

$$V_s = VCL + VA / (1 - P3/P2)*$$

*VCL and VA are constants of the pycnometer; they may be assumed constant (VCL= 154.9380114 cm^3; VA= 78.2012 cm^3) or may be re-

measured with each trial

c. $n = V_w / (V_w + V_s)$

IV. *Load Cell Calibration (Triaxial Tests)*

Theory: When a load is applied to the setup in the triaxial machine, the load cell outputs a certain voltage depending on the magnitude of the load. Therefore, we are interested in knowing this conversion from voltage to force/applied load, which should be a linear relationship. Through the process of calibration, we apply a known load to a sample, read the corresponding voltage output, graph this relationship to find the slope, then enter this value into the data software program.

Procedure:

1. Setup of the Ring Force Gage (aka 'calibration ring'; SN: 52352 from Morehouse Instruments Co.)
   a. Remove the ring gauge from the metal box in which it is stored
   b. Put the ring gauge on the triaxial platform
   c. Screw the extra piece kept in the box into the top of the ring gage
   d. Place the (small) load cell on top of the extra piece
   e. Bring platen down until force just registers on gage; back off slightly
   f. Zero the gage on the ring
2. Computer
   a. Open MAX Software program
   b. Under volts --> axial load (properties); the enter m (slope) from calibration

and b=0; this allows the computer to convert volts → MPa

c. To view the voltage during the test, right click on axial load; choose "test"

3. Calibration

a. Balance load cell channel (Ch.5)

b. Record the following values; It is important to remember that any tests you run in the future using this calibration must have the same settings!

i. Balance

ii. Gain (should be 8.0)

iii. Excitation (should be 10.0)

c. Begin slowly loading the setup; At each division, stop the platen

d. Record divisions and resulting output voltage (1-20 by 1's; 20-60 by 5's; 60-100/200 by 10's); →1 ring division = 725 pounds

e. Unload the setup

f. Remove the ring gage and load cell; place in proper storage locations

4. Analysis and Results

a. Plot stress (in N) versus voltage (in mV)

Conversion: 4.45 * pounds = Newtons (ref: www.igus.com/conv.htm)

Expect: 1 mV = 26.19 psi

b. Regression analysis

c. Convert to MPa for compressive tests (compressive plug = 2.794 x 10-4 m^2; ref: Dave Boutt)

d. Example: *May 2003 calibration*

i. Graph; See figure below

ii. y = 27046 x - 1099.5 (N); R^2 = 0.9999

→ Enter **27046** in axial load properties in MAX

iii. 27046 N / 2.794 x 10-4 m^2 = 96.80029 MPa

→ Enter **96.80029** in axial stress properties in MAX

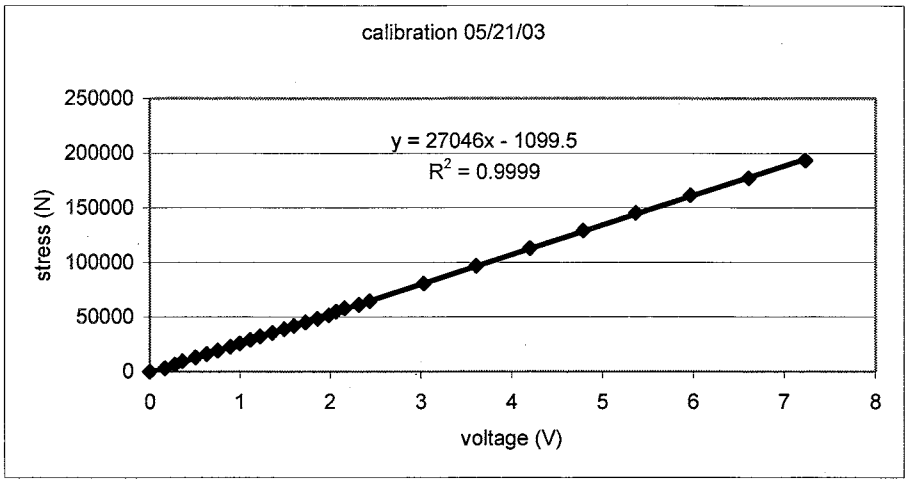

V. *Brazil (Indirect) Tensile Strength Measurements: Triaxial Machine*

Theory: A disc-shaped sample is loaded across the diameter by an apparatus such as a triaxial machine. It is crucial that the compressive load can be precisely measured. This loading (F) generates a compressive stress ($\sigma 1$) as well as a tensile stress ($\sigma 3$) oriented in a direction perpendicular to the applied load. See Figure 2. When the applied load reaches a critical level, the sample will fail in tension. Such a fracture will be oriented in a direction perpendicular to the maximum stress, $\sigma 3$ in this case. This stress at which the rock fails or yields is known as the tensile strength.

An alternative method in which the sample is physically attached (cemented) to the apparatus applying the stress may be preferred. However, the Brazil test is recognized as a valid indirect measure of tensile strength, and is a much quicker procedure.

In either method, it is suggested that a number of tests should be run for each rock sample. Ten replications are preferred, but practical considerations should be kept in mind.

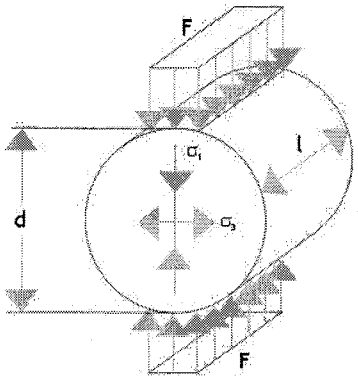

Figure 2: A load is applied (F) which generates both a compressional ($\sigma 1$) and tensional ($\sigma 3$) stress on the sample. When a critical load is reached, the sample will fail perpendicular to $\sigma 3$.

Procedure:

1. Sample Preparation

   a. Drill plug from desired rock. The diameter should be greater than 54 mm (ISRM). The plug should be drilled perpendicular to the desired direction of the tensional field to be tested. In the example in Figure 3, the desired tensional field was to be oriented north-south. The orientation should be carefully noted on the plug (Figure 4).

   b. Cut the plug into discs. The length should be approximately equal to the radius. The orientation should be carefully noted on each disc. A line along the length indicates north (Figure 5). The surfaces should have no visible tool marks or irregularities. Faces should be flat to within 0.25 mm and parallel to the edges within 0.25°.

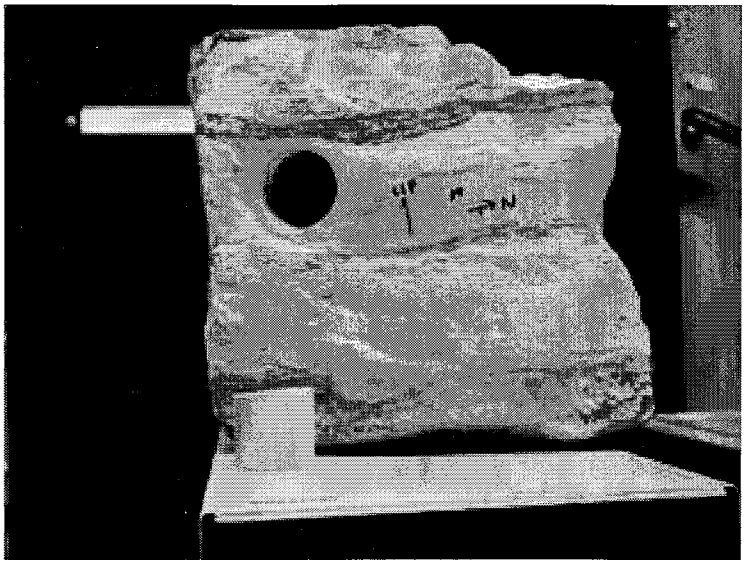

Figure 3: Drill a plug from the sample, making sure the orientation is correct for the desired tensional field to be tested.

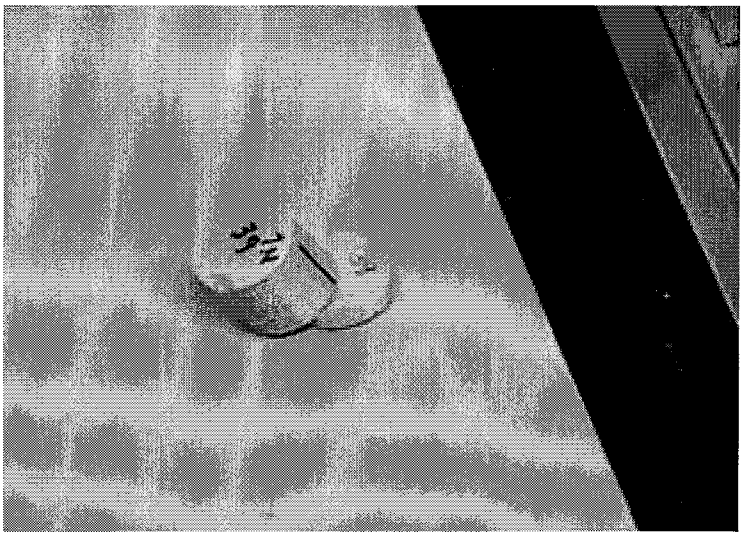

Figure 4: Carefully mark the orientation on each plug.

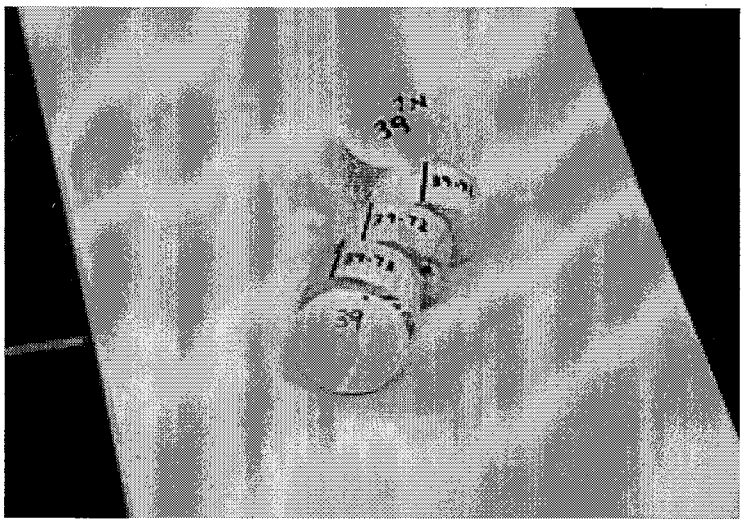

Figure 5: Cut the plug into slices, and carefully label each slice.

c. Record the dimensions (diameter and length) of each plug. Since variation is inherent in the sample and is also likely due to human error, the following method is suggested:

   i. Record 2 diameters – one at any location and another perpendicular to the first measurement. Use the average in future calculations.

   ii. Record 4 lengths – one at any location then at 90°, 180°, and 270° (relative to first measurement). Use average in future calculations.

d. Mark a line on the face of the sample. This line should be oriented such that it represents the expected orientation of the failure that will be generated. It should also be perpendicular to the desired tensional stress (Figure 6).

e. Wrap cellophane or masking tape around the diameter of the sample. The edges should overlap the sample slightly (~10 mm). Caution should be taken to make sure the tape is flat against the sample and not overhanging the edges significantly (<1 mm).

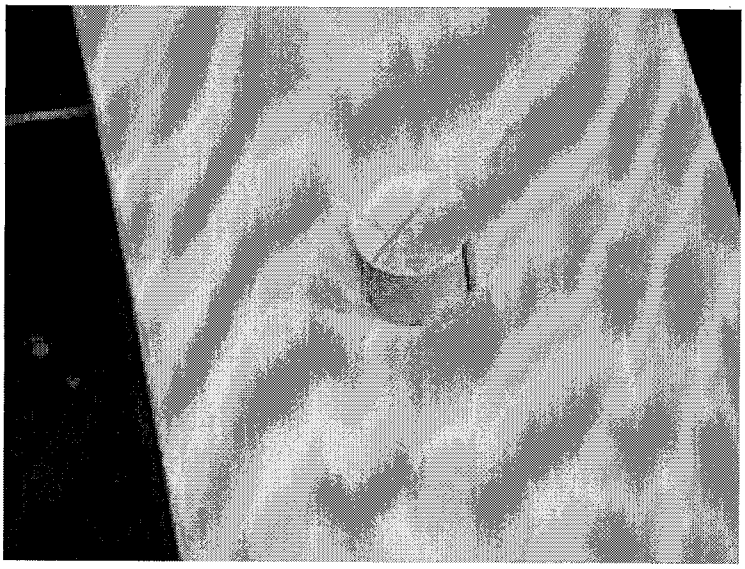

Figure 6: Mark a line perpendicular to the desired tensional field on the face of the sample.

2. Computer

    a. Open Virtual Bench Logger

    b. Edit > Load Settings > brazil_jen.lgr > Open

    c. Edit > Settings >

        i. File Configuration

            1. enter filename, user name(s), and comments

            2. start new file after 100000 lines

            3. (check) enable logging

            4. (check) begin logging on start

            5. field length: 10; precision: 6

            6. > OK

        ii. Timing Configuration

            1. (check) begin logging on start

            2. (check) stop manually

3. recording rate: fast

4. log to disk every: 1 time

5. display length: 15 min

6. > OK

iii. (Under Logger Settings window) – Channels:

1. Axial Load, channel 0

a. (check) log

b. units: MPa

c. max= 2 E 4; min= 0

d. M= 2.705 E 4; B= 0

2. Platen LVDT, channel 9

a. (check) log

b. units: inches

c. max= 1 E 1; min=0

d. M= 1.101 E 0; B=0

3. > OK

d. You can manually change the axes- both scale and what they are graphing as the test is being run; this will have no effect on how the program runs or how the data is logged

3. Sample Testing

a. Set up the triaxial machine

i. Place 1.7" tall steel disc on the platform

ii. Place 11" tall metal cylinder with handles on the side on top of (i)

iii. Place metal sample holder and steel ball bearing in the center of (ii)

iv. Place a (metal) object in the side of the holder; the sample will be placed here later, but this enables you to change samples without performing this step (3a: i. – iv.) for each sample; see Figure 7

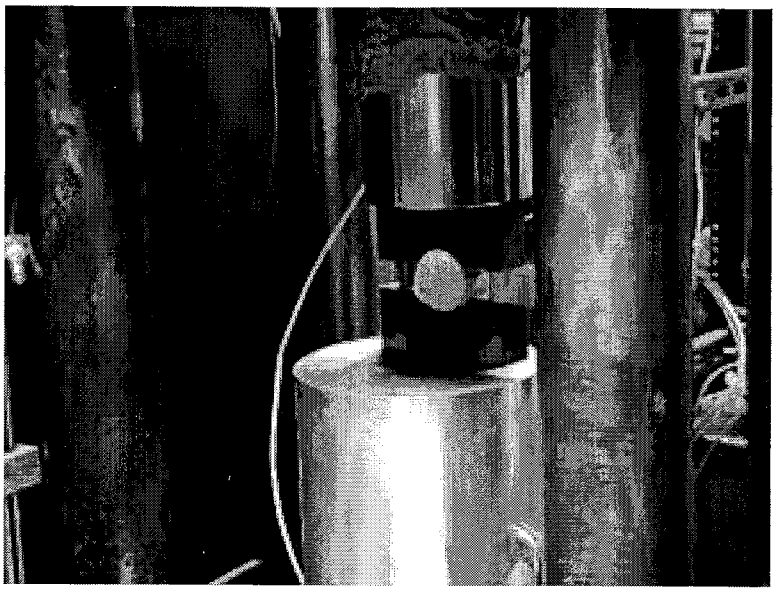

Figure 7: Load the sample into the triaxial machine.

v. Place the load cell on top of (iii); you will have to balance it in place

vi. Bring the platen down on top of the load cell, making sure that the load cell fits perfectly and straightly into the platen bottom

vii. Continue bringing the platen downward until the load cell fits into the circular indentation on the bottom of the platen; you want to be close to loading the sample, but not yet applying stress

viii. The load cell should still spin; if not, the setup may be crooked and should be fixed!

b. Load the sample into the triaxial machine (see Figure 7 for setup)

i. Place the sample slice into the holder

ii. Orient the sample so that the line previously drawn on the face is exactly vertical; induced tensional field will be oriented horizontally

iii. Center the sample in the holder

iv. Remove the metal object carefully

v. Carefully make sure that the holder is exactly straight and will stay that way even when the sample is loaded

c. Start the data logger (START on bottom of screen)

d. Check to make sure that the data is being recorded in the specified file; the file should have headings and data for a number of time steps

e. Begin loading the sample by bringing the platen down (forward) at a speed of 0 (slowest speed)

f. When the samples starts to 'feel' the loading, you should see the changes in the logging program

g. Continue loading the sample at a speed of 0 until the sample fails

h. Immediately stop loading as soon as the sample breaks

i. Unload sample by raising platen (reverse) at a speed of 10 (Figure 8)

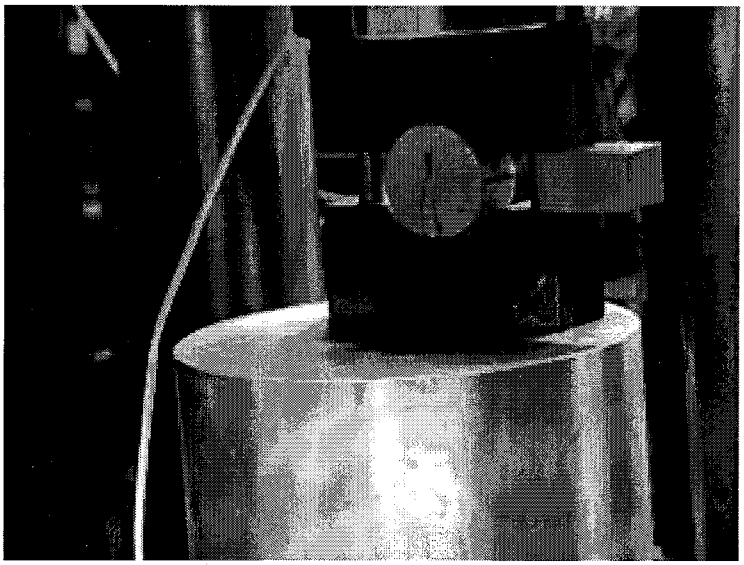

Figure 8: After the sample is loaded to failure, unload the sample.

4. Data Analysis

a. Transfer data to spreadsheet program (such as Excel)

b. Enter the measured thickness (T) and diameter (D) of the sample

c. Calculate axial stress (MPa) from axial force (N):

Stress = (2 * Force) / (PI * D * T)

i. In all cases, axial stress at the time of failure is the tensile strength

ii. In most cases, the maximum value of axial stress is the tensile strength; typical range: 5-20 MPa

VI. *Uniaxial Compressive Strength Measurements: Triaxial Machine*

Theory: Load is applied (σ_1) to a cylindrical sample while leaving the load on the sides of the sample at atmospheric pressure. Strains in both axial and lateral directions may be non-zero. The sample is loaded at a near-constant strain rate until a load of ~30% of the failure strength is reached, as estimated from porosity and bulk mineralogy of the rock. The load is then cycled in order to demonstrate the elastic behavior of the rock. The

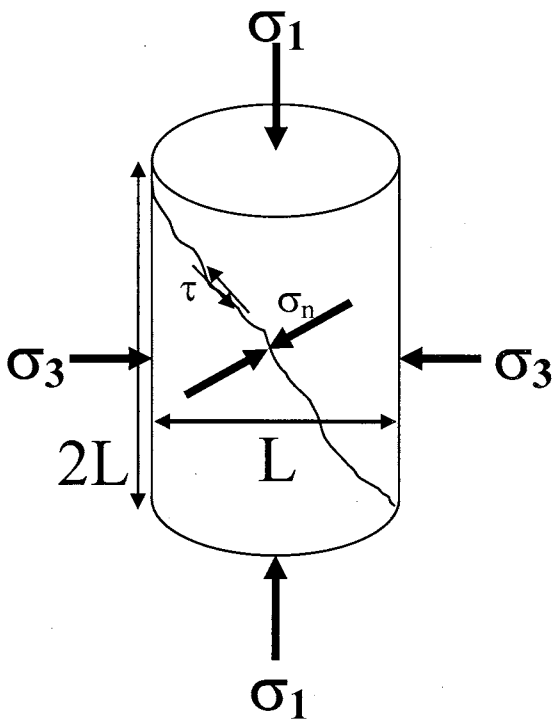

Figure 9: Schematic of stress state on cylindrical sample.

test is finished when the sample is broken and there is an overall decrease in stress for an increase in strain. See Figure 9 for schematic of general setup and loading orientation.

Procedure[♦]:

1. Sample Preparation
    a. Drill plug from desired rock with ¾" diameter diamond drill bit. Care should be taken so that the plug is oriented in the desired direction (vertical in many instances). The plug should be 1.75 - 2.0" long. Clearly label the sample number and (vertical) orientation on the plug.
    b. Trim both ends of the plug to roughly parallel using the Buheler isocut saw in the RML
        i. The sample is held tightly in place in an aluminum machined piece as it is cut. The closer the saw is to this machined piece, the better and straighter the cut.
        ii. The sample should be trimmed to ~1.6" in this step
        iii. This step ensures less passes with the time-consuming lathe
    c. Face both sides of the sample in the Model 4500 Micro-Lathe II (For safety, a dust mask should be worn!)
        i. Ends need to be parallel to one another to within 5/1000"
        ii. Ends need to be at perfect right angles to the sides
        iii. Use a diamond tipped bit. Depending on the sample lithology, the bit may need to be changed after 5-10 samples. These bits are available from Enco (Model 388-8866) for a cost of ~$7.00 per bit.
        iv. Cover moving parts of the lathe with ceran-wrap to prevent rock

[♦] At the end of this section, there is a glossary that defines various terms (italicized in the text). There are also a number of corresponding pictures.

dust from damaging the machinery

v. Once sample is secured tightly in the lathe, mark a single thin line on the side of the sample that at a 90° angle to the end/face

vi. Make multiple passes (normally should take 3-6 passes) at small increments (~6/1000")

vii. After you think the entire end face has been touched in a single pass, move the bit 3/1000" closer and make a final pass

viii. During the facing process, use the air hose to remove excess rock dust at least once after each pass

ix. Carefully mark the end with an "X" once the end has been faced

x. Optional: record length and diameter of sample

d. Apply strain gages

i. General Information

1. Strain gages and other application materials are available from Vishay Micro-Measurements Group

2. It is suggested that you purchase strain gage types from the "Super Stock" section of catalog for faster delivery

3. Gage used for Uinta Basin work: EA - 06 - 125 TM – 120

a. E => indicates backing type

b. A => indicates alloy

c. 06 => depends on thermal expansion coefficient

d. 125 => active gage length in mils

e. TM => grid and tab geometry

f. 120 => resistance in ohms

4. Cost: ~$56.00 / 5 gages (also- educational discount)

ii. Glue strain gage onto sample plug (latex gloves should be worn) using M-Bond 200 Adhesive

* Detailed directions for application are available from Vishay *Instruction Bulletin B-127-14*; a copy should be in the laboratory *

1. Using tweezers, place the gage - bonding side down - on a clean surface
2. Place a piece of cellophane tape ~2" long on the gage, sticky side down. Take care not to place any tension on the tape!
3. Align the triangles along the side of the gage with the line drawn on the sample while it was in the lathe. Attach the gage to the sample with the tape.
4. Carefully peel back the tape to ~ ½" past the gage
5. Apply 200 Catalyst-C and let dry (~1 minute)
6. Apply a small amount (1-2 drops) of glue to the gage back using a toothpick
7. Press the gage (and tape) to the sample smoothly
8. Use rubber and metal curved pieces and clamps to hold the gage firmly to sample for at least several minutes; let dry ~24 hours

iii. Solder *lead wires* to strain gage

* Detailed directions and tips for soldering are available from Vishay *Tech Tip TT-609* Bulletin; a copy should be in the RML *

1. Cover gage and tip of soldering tab with masking tape (if solder comes in contact with the gage itself the resistance will be altered and the gage may be ruined)
2. Soldering temperature: ~500° F
3. Tin the *lead wire*; trim the end of the wire (part not tinned, or so that ~$^1/_8$" of the wire is exposed)
4. Attach to soldering tab on strain gage by laying the wire on the

tab, then firmly pressing down on the wire with the soldering iron; the iron should touch for only 1 - 1 ½ seconds! If you need to try again, let the tab cool first!

5. Carefully remove masking tape

iv. Coat strain gage

1. Apply 1 coating of M-Coat D Air-Drying Acrylic Coating to the gage; air dry 15 minutes; cure 24 hours
2. Apply 1-2 coatings of M-Coat B Nitrile Rubber Coating to the gage and soldering tabs with *lead wires*; air dry (between each coat) 1 hour; cure 24 hours

2. Computer

a. Open (National Instruments) Virtual Bench Logger

b. Edit > Load Settings > jensummer2003.lgr > Open

c. Edit > Settings >

i. File Configuration

1. enter filename, user name(s), and comments
2. start new file after 100000 lines
3. (check) enable logging
4. (check) begin logging on start
5. field length: 10; precision: 6
6. > OK

ii. Timing Configuration

1. (check) begin logging on start
2. (check) stop manually
3. recording rate: fast
4. log to disk every: 1 time
5. display length: 15 min

6. > OK

iii. (Under Logger Settings window) – Channels:

1. Axial Load, channel 0

a. (check) log

b. units: MPa

c. max= 2 E 4; min= 0

d. M= 2.705 E 4; B= 0

2. Axial Strain, channel 5

a. (check) log

b. units: strain

c. max= -1 E -2; min= 0

d. M= 1 E -2; B= 0

3. Lateral Strain, channel 6

a. (check) log

b. units: strain

c. max= -1 E -2; min= 0

d. M= 1 E -2; B= 0

4. *Platen* LVDT, channel 9

a. (check) log

b. units: inches

c. max= 1 E 1; min=0

d. M= 1.101 E 0; B=0

5. > OK

d. You can manually change the axes - scale and channel - as the test is being run; observing axial strain and axial load is a good idea; a good max for the axial load is 300 MPa; default for strain is usually good.

3.Sample Testing

a. Turn on the (2 switches on the) strain indicator. Let it warm up for 30 minutes (D. Boutt's recommendation) to 12 hours (J. Smith's recommendation); there seems to be a slight drift while warming up

b. Begin sample setup

i. Clamp the *base* into the *stand*

ii. Carefully place the wires of the *wired base* through the *base*

iii. Place 1 spacer on the *wired base*, holes only side up; Figure 10.

iv. Place the sample on top of the spacer and secure with a piece of cellophane tape wrapped around the bottom of the sample and the 1st spacer

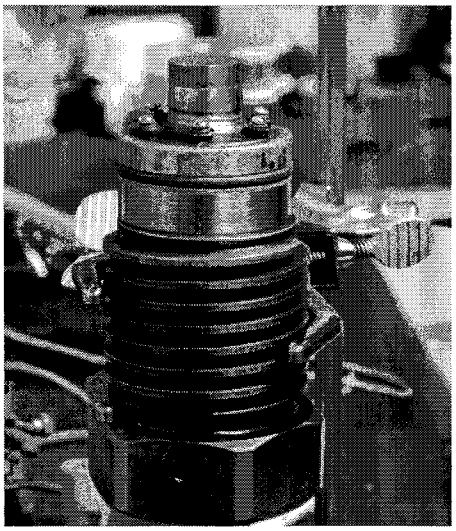

Figure 10: One spacer on the wired base.

c. Hook up the *lead wires* from the sample as illustrated below in Figures 11 and 12. (This is not the only configuration that will work!)

i. Attach the lateral's right *lead wire* to the left silver screw (from the side point-of-view). Do this by placing the bare end of the wire between the two washers and tightening.

ii. Attach the lateral's left *lead wire* to the brass screw to the left of the (silver) one you just used. On the opposite side of the screw, attach a small piece of wire ~1" long.

iii. Attach the loose end of the wire to the brass screw to the left of the (brass) one you just used.

iv. Attach the axial's left *lead wire* to the right silver screw.

v. Attach the axial's right *lead wire* to the brass screw to the right of the (silver) one you just used. On the opposite side of the screw, attach a small piece of wire ~1" long.

vi. Attach the loose end of the wire to the brass screw to the right of the (brass) one you just used.

vii. Make sure that no bare wire is touching any part of the *wired base* (not counting the screws).

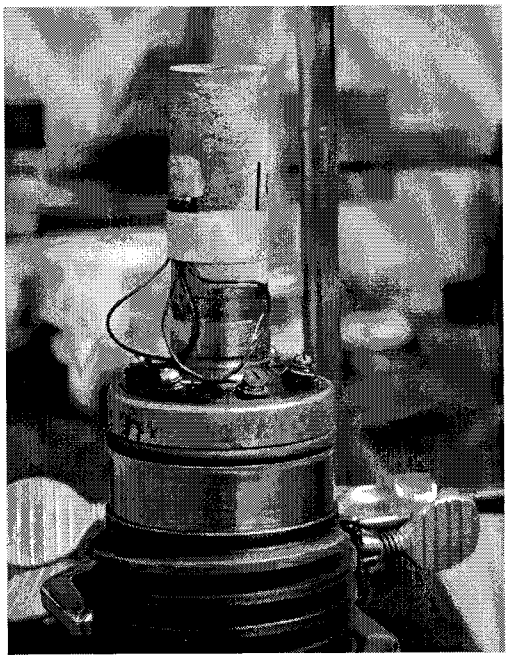

Figure 11: The wired base, spacer, and sample connected by lead wires.

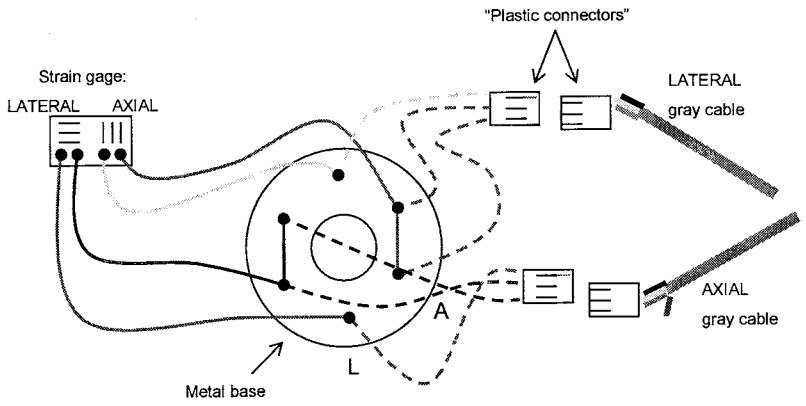

Figure 12: Schematic of how the *lead wires* from the strain gage should be attached to the *wired base*. Dashed lines represent wires coming out of the bottom of the *wired base*.

viii. The wires connected to the bottom of the *wired* base do endure a lot of wear; inspect them regularly for kinks that may lead to possible short circuits.

d. Check that axial and lateral strain channels are working. This is done by attaching the *plastic connectors* attached to the *wired base* to those attached to the *gray cables* and balancing the axial (ch 7) and lateral (ch 4) strain channels. Balancing channels is done by turning the 'balance' knob on the *strain indicator* until the red light is no longer on. In theory, you want a balance at 5. If the balance is <0.5 or >9.5, the channel may not be balanced and you probably have a problem.

TROUBLESHOOTING (if channels won't balance):

i. As an aid, you can use the Measurement and Automation Studio software. Note: the channels don't necessarily correspond to the strain indicator (also known as the "silver monster")

ii. Test the *gray cable*. Switch axial and lateral if one channel is working

iii. Test electrical connections using a voltmeter (the answer you want to get is in parenthesis):

1. Are all (3) axial screw connected to one another? (yes)
2. Are any axial screws connected to the lateral? (no)
3. Are any axial screws connected to the *wired base*? (no)
4. Are all (3) lateral screw connected to one another? (yes)
5. Are any lateral screws connected to the *wired base*? (no)

iv. Test the *plastic connectors*. Pop out the individual wires. Use the voltmeter to make sure there is a connection between the end of

the wire and the corresponding screw(s). If you really want to check this, you may need to detach the *lead wires* from the *wired base*.

v. Test connection straight from the gray wire to the wires in the *plastic connectors*. Do this by physically holding them together and try to balance the channel.

vi. Test the resistance across the gage; should be 120.0 to 120.3 ohms exactly. If not, the gage may be damaged.

e. Finish sample setup

i. Place another spacer on top of the sample (holes only side down)

* The length of the 2 spacers plus the sample should be ~55 mm long (a range including 53-60 mm will work); if it is too long, it may not fit in the *chamber*! *

ii. Place the *steel bar* on top of and flush with the spacer; clamp into place with the *stand*; Figure 13

iii. Secure with a piece of cellophane tape wrapped around the sample, 2nd spacer, and steel bar

iv. Wrap a piece of cellophane tape around the middle of the sample to hold the *lead wires* flat against the sample

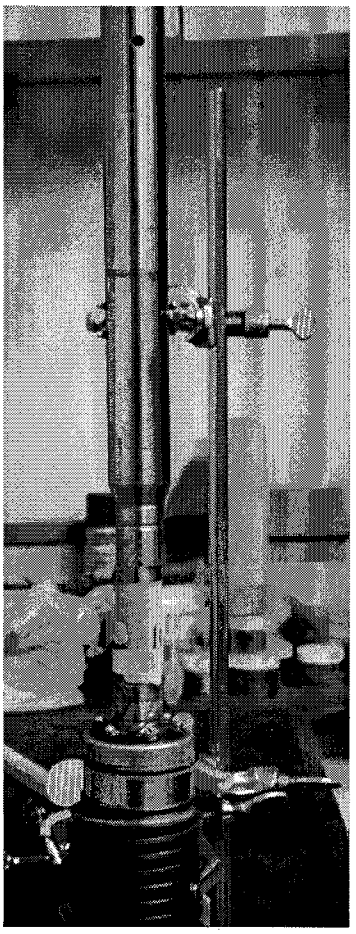

Figure 13: Sample prepared in stand with spacers and steel bar.

v. Cut a piece of heat shrink long enough to go from the base of the sample to just past the thicker

part of the steel bar; Figure 14

vi. Hold the heat wrap in place from the top as you start heating with the *heat gun* from the bottom; Be careful not to overheat – this could actually melt the wires; Figure 15

Figure 14: Heat shrink cut long enough to cover from the base to the steel bar.

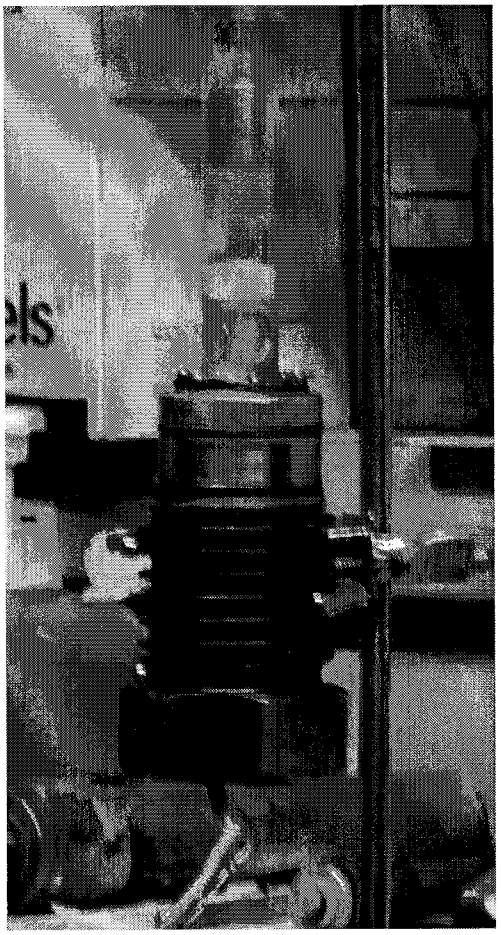

Figure 15: Heat shrink heated tightly around the sample.

vii. Check that the axial and lateral strain channels are working

viii. Attach two pieces of wire around the heat wrap and sample (one at the top, one at the bottom) to hold things tightly in place; tighten with pliers

f. Secure the sample *setup* into the *chamber*

i. Carefully carry the *setup* to the *platform*

ii. Fit the *setup* into the *chamber* from below

iii. Screw *base* into the *chamber*. Make sure it is screwed in very tightly (this is probably past where you think it has been tightened); you should not be able to see any threads.

iv. Place the *O-ring* thread side up (very important!) over the steel bar and gently push down; should fit into *chamber* slightly; Figure 16a

v. Fit *T-screw* piece over bar and screw down tightly: Figure 16b

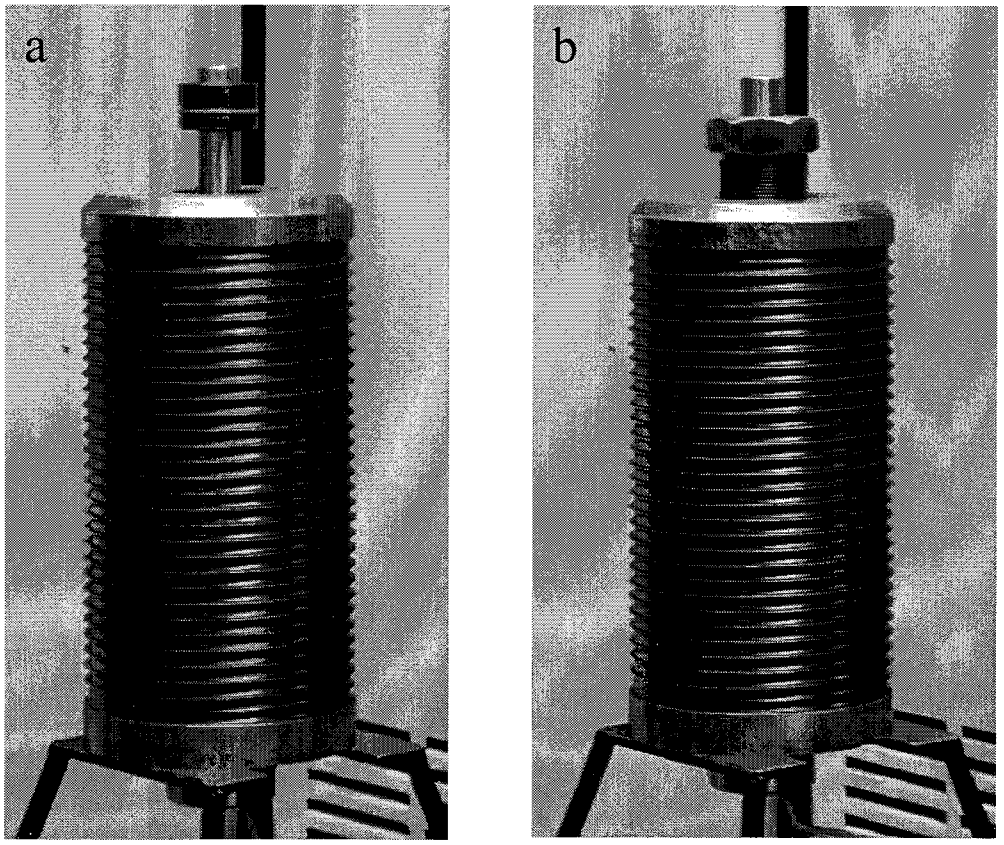

Figure 16: (a) *Setup* screwed tightly into *chamber* with *O-ring* and (b) *T-screw* placed carefully on the *steel bar*.

g. Move the *assembly* onto the *platform* of the triaxial machine and set on its

side. Note: the *chamber* is very heavy!

h. Carefully stand the *assembly* upright on top of the *base piece*; be careful not to pinch any of the wires and make sure they fit through the slot in the *base piece*

i. Check that axial and lateral strain channels are working; leave the *gray cables* connected

j. Place the *load cell* on top of the *assembly*

k. Bring the *platen* down on the *load cell*. Make sure that the *load cell* can rotate freely. Continue bringing the *platen* down until it just barely starts loading (can't rotate). Reverse the *platen* slightly.

l. Check that axial and lateral strain channels are working

m. TESTING

i. Record gain (should be 0.5 for axial and lateral strain channels; 8.0 for load cell; 2.0 for platen LVDT) and excitation bridge voltage using the voltmeter placed into red and black holes on the strain indicator (6.00 for axial and lateral strain gages; 10.00 for *load cell*, 12.00 for *platen* LVDT; if not, tweak with screwdriver) for each channel being used

ii. Balance axial strain (ch 7), lateral strain (ch 4), *load cell* (ch 5), and *platen* LVDT (ch 9) channels; record balance

iii. Record gage factor for the strain gage (this information can be found on the pink sheet in the package with the strain gages)

iv. Start data logger

v. Check to make sure that the data is being recorded in the specified file; the file should have headings and data for a number of time steps

vi. Recheck balances; not too critical since you will normalize data

vii. Begin loading the sample by bringing the *platen* down (forward) at a speed of 0

viii. The strain gages should be responding. "If not, it's bad" (Dave Boutt, 05/29/03).

ix. Load/Unload loops

1. Idea is to go up ~20 MPa of stress then down 10 MPa
2. Do first loop near the beginning of the test
3. Do 3 or 4 more loops
4. Example looping schedule: 0 to 20 MPa, 20-15, 15-40, 40-35, 35-60, 60-55, 55-80, 80-75, 75-100, 100-95, 95 upward until failure
5. Range of failure strengths for the Uinta Basin samples was usually 100-200 MPa

x. Continue loading the sample to failure (should hear a "pop")

xi. Unload the sample by raising the *platen* (reverse) at a speed of 10

xii. Stop the data logger

n. Physically unload the sample from the triaxial machine

i. Remove the *load cell* once the *platen* has been raised far enough

ii. Take the entire *assembly* off the *platform*

iii. Remove the *T screw*

iv. Carefully unscrew the base from the bottom while putting firm, even pressure on the *steel bar*; you might have to tap the top of the *steel bar* with a hammer (cover with towel first – do not hit the *steel bar* directly!)

v. Remove the *setup* from the *chamber*

vi. Remove the *O-ring* with the *ring tool*

o. Use a razor blade to cut the *heat shrink* right above and below the sample;

it is ok to cut the wires now

p. Turn off the strain indicator if you will not be testing more samples soon (in the next day); it tends to warm slightly with time if left on.

1. Data Analysis

Theory: The data obtained is analyzed for a number of parameters: Young's Modulus (taken as the slope of the load/unload loops of the axial stress, σ_1, versus axial strain plot), Poisson Ratio (lateral strain, σ_3, versus axial strain, σ_1), and Bulk Modulus (mean stress versus volumetric strain). Mean stress in the case of a uniaxial compression test is the same as axial stress. Volumetric strain, σ_V), is the sum of all the rock strain; in this case, $\sigma_v = \sigma_1 + 2\sigma_3$.

The failure strength of the sample was taken as the maximum stress level obtained during the test. This analysis was performed using an interactive MATLAB program written by David Boutt.

a. Prepare the data file

   i. Remove headers and footers

   ii. Remove data after failure (not necessary, but makes for a better graph)

   iii. Save as a different, but similar name (I had the originals saved as UB##_C.log, and the modified files were saved as UB##.txt)

b. In the MATLAB program, enter the name of the file on the line that reads " data=load('*filename here*') " ; save

c. Press F5 to run program

d. Three graphs will appear, one at a time. A large "+" will also appear. The objective is to visually pick the slope of the part of the curve at early time that represents elastic behavior.

e. For each graph:

i. Click once at the beginning of a loop

ii. Click once at the end of the same loop

iii. You can do this as many times as you want (3 times is suggested), but you must do it the same number of times for all 3 graphs

iv. Press enter to go on to the next graph

v. Figure 17 shows an example graph

f. When you have completed all 3 graphs, go to the MATLAB window

g. Values of E, K, NU, and PKSTRESS should be displayed

i. E = Young's Modulus, in GPa

(expected range should be on the order of $x10^4$ GPa)

ii. K = Bulk Modulus, in GPa

(expected range should be in the range of $x10^4$ to $1x10^5$ GPa)

iii. NU = Poisson Ratio, unitless

(expected range shoult be in the range of 0.10 to 0.40)

iv. PKSTRESS = maximum (loading) stress obtained during loading

(might be in the range of 50 to 300 MPa)

h. Interpretation of results, *overview*

i. Young's Modulus- defn: the ratio of applied axial stress to axial strain; a value near 0 indicates compressible and a value nearer 0.5 indicates a more incompressible sample

ii. Bulk Modulus- defn: the change in volume as stress is applied

iii. Poisson Ratio- defn: the ratio of lateral to axial strain

iv. Peak Stress- gives you an estimate of the pure strength of the rock

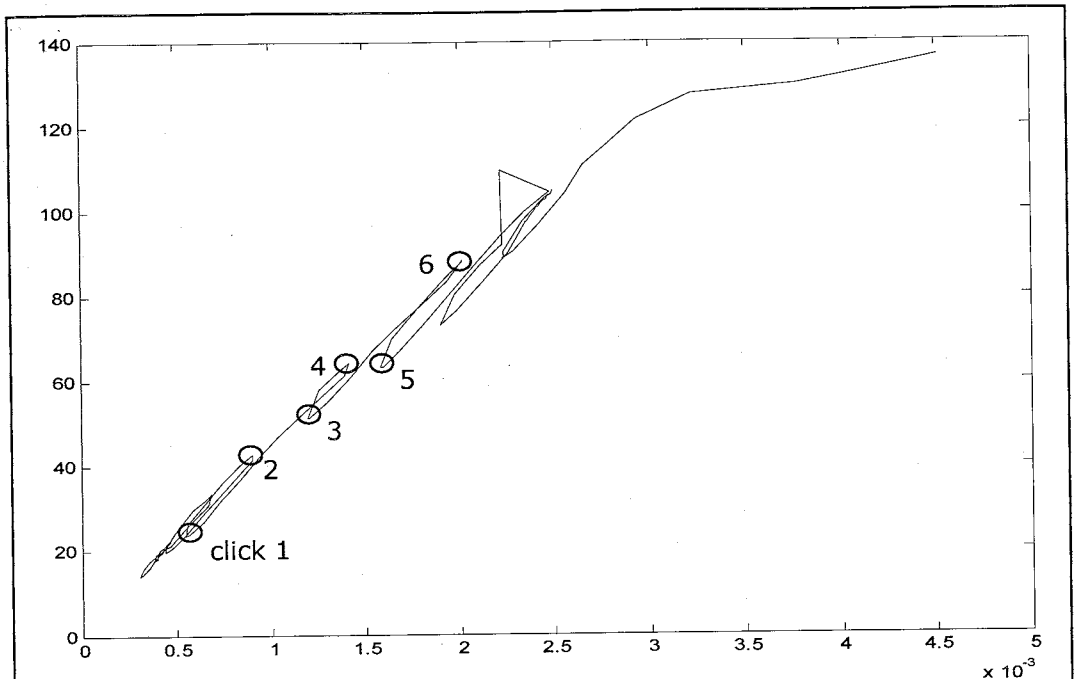

Figure 17: Example graph showing loops and desired slope for calculation of parameters.

Glossary for compressive tests:

Note: These are not all technical terms! Many are simply names that were made up for the purposes of explaining the above procedures.

1. *assembly* - setup inside chamber

2. *base* –bottom piece of the setup;

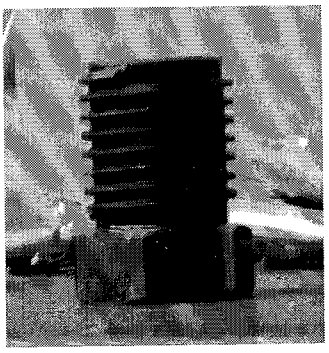

enables the setup to be screwed into the chamber from bottom

3. *base piece* – placed beneath the chamber when on platform; allows for

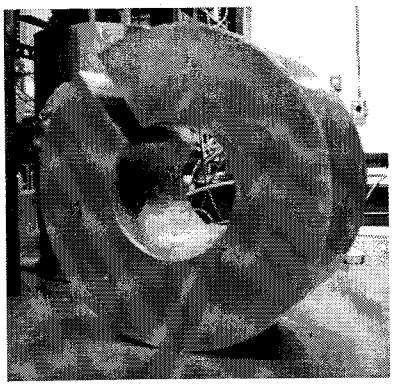

(1) a better suited height for loading and (2) protects the gray cables from being pinched

4. *chamber* - the large metal cylinder; setup is screwed into the chamber from the bottom; the chamber provides a means to run confined tests as well as protection from any possible violent failure

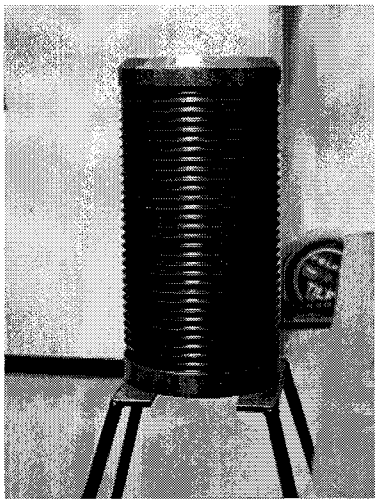

5. *gray cable(s)* – connects the wires coming from the strain gage on the sample to the strain indicator

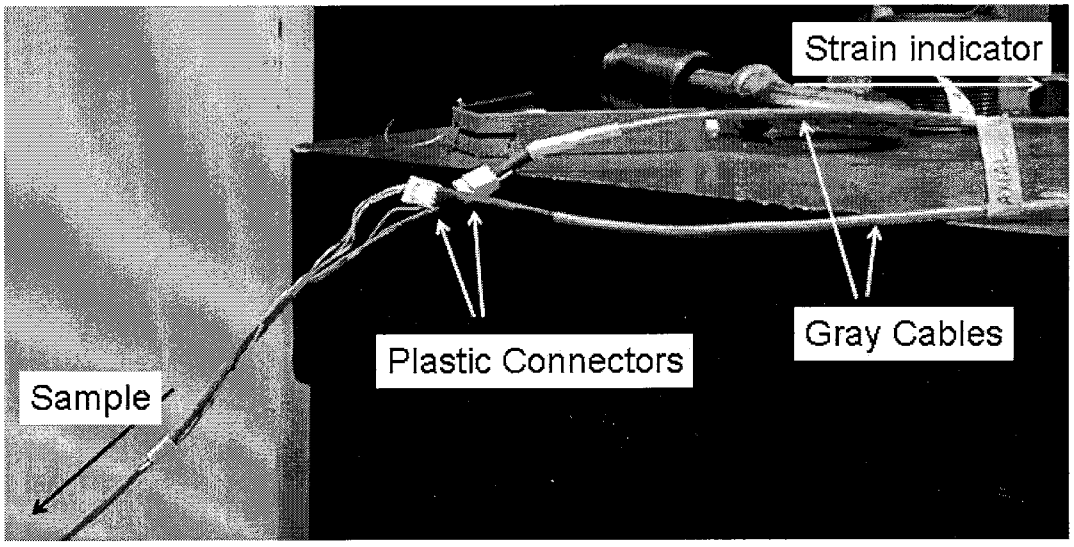

6. *heat gun* – used to shrink the heat shrink covering the sample, spacers, and part of the steel bar

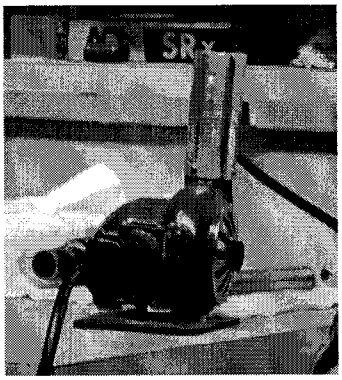

7. *heat shrink* – clear tubing ~1" in diameter that, when heated, shrinks to a tight fit around the sample, spacers, and (part of) steel bar)

8. *lead wire* – the (thin) wires which are soldered to the strain gage and attach the strain gage on the sample to the wired base

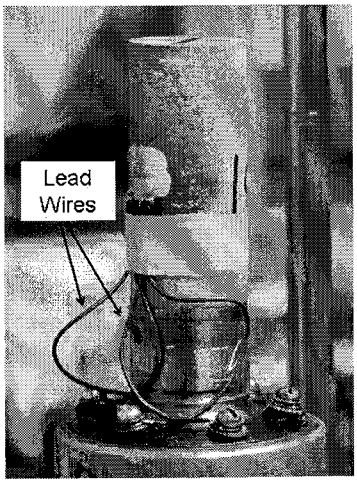

9. *load cell* – measures the load being applies; placed on top of the steel bar after the setup is inside the chamber and the chamber on the platform

10. *O-ring* – fits (tightly) into the top of the chamber around the steel bar; prevents the bar and setup from shifting during loading and testing; threaded inside must be oriented upward!

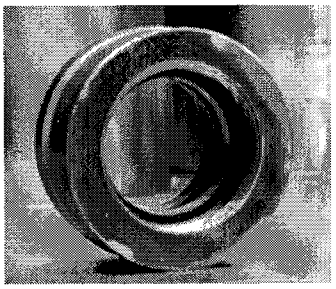

11. *platen* – part of the triaxial machine that is lowered down on the sample; results in an induced stress on the sample

12. *platform* – part of the triaxial machine; where the chamber is placed for testing

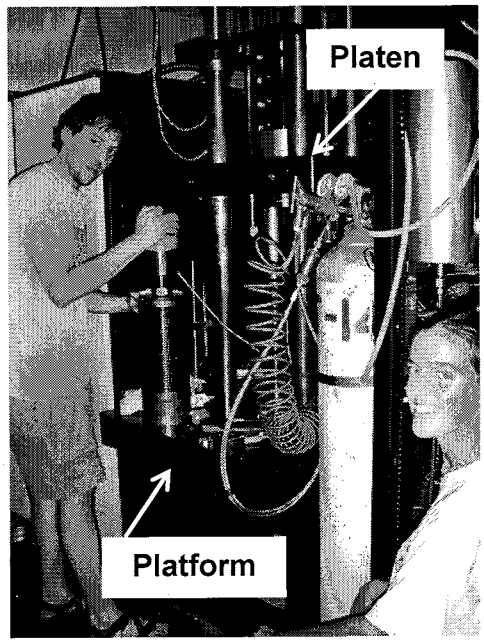

13. *plastic connector(s)* – a means to attach the strain gage to the strain indicator for transmission of a signal; see also gray cables

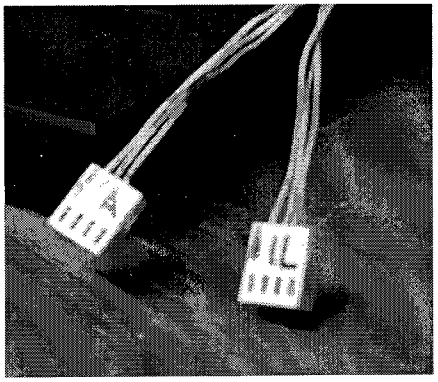

14. *ring tool* - used to remove the O-ring from the chamber after testing

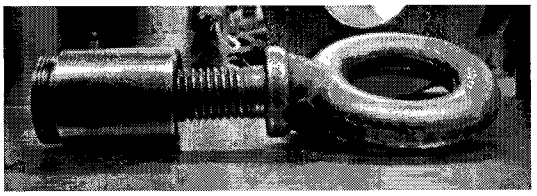

15. *setup* – sample, attached to wired base (by wires), base, heat shrink, and steel bar

16. *stand* – used to clamp the base into place so that the sample can be set up and wired to the wired base; also has a clamp to hold the steel bar in place during heat shrink application

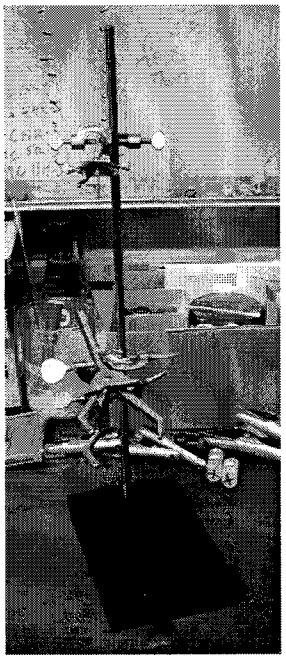

17. *steel bar* - cylindrical solid steel bar, 9" long, 1" diameter at the top (near the hole)

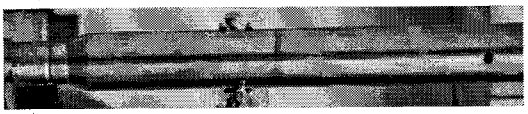

18. *strain indicator* - MicroMeasurements Series 2100; 10 channels; used to process the signal received from the strain gage; also known as the "silver monster"

19. *T-screw* – screwed into the top of the chamber once the setup has been placed inside

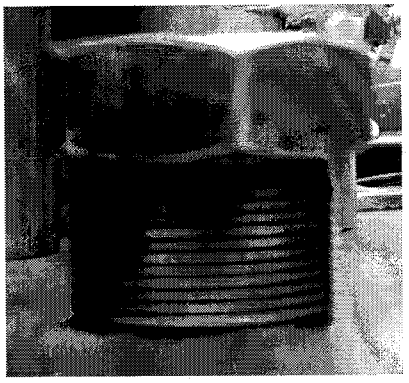

20. *wired base* – wired such that lead wires connected to the screws on top of the wired base transmit a signal to and through the gray cables to the strain indicator; some details on wiring setup is described in the procedure

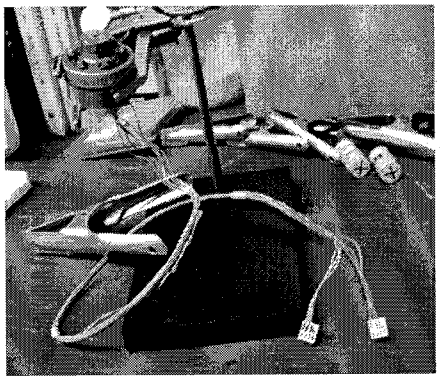

VII. *Mineral Identification: X-Ray Diffraction (XRD)*

Theory: When x-rays are passed through matter, the radiation interacts with electrons in the atoms and is scattered. Diffracted x-rays are emitted at distinct angles depending on the spaces between the atoms organized in planes. Each set of planes has a specific interplanar distance and will give rise to a characteristic

angle of diffracted x-rays. If the wavelength (λ) of the x-ray is known and the angle (θ) measured with a diffractometer, the interplanar distance (d) can be calculated from the Bragg Equation:

$$n \lambda = 2 d \sin\theta$$

A set of 'd-spaces' obtained from a single compound is compared with sets of d-spaces obtained from standard compounds for mineralogical makeup. (XRD theory from Rigaku/MSC website.)

Procedure:

1. Sample Preparation
    a. Gather samples
    b. Crush ~3 g of sample wrapped in a paper towel with a hammer
    c. Using a ceramic mortar and pestle, grind the sample into a fine powder; it should have the 'consistency of flour' and you should not be able to feel any grains between your fingers
    d. Make sure you have at least 20 mg of powdered sample
    e. XRD prep room
        i. Use a slide specifically designed for running XRD; this slide is approximately 2" x 1" and has an indented area in which the powdered sample is placed
        ii. Pour a small amount of powdered sample into this indented area
        iii. Using a blank glass slide, carefully 'scrape' excess away from edges of indented area
        iv. Place the glass slide on the pile of powder and apply a small amount of pressure to pack down the sample
        v. Turn the slide with sample upside down to make sure that the sample will not fall out during the XRD process

2. Sample Testing

a. Turn on computer

b. On XRD –

i. Turn POWER ON

ii. Turn XRD ON

iii. Turn kV to 40 (one notch at a time!)

iv. Turn mA to 25 (one notch at a time!)

c. Run silica standard (Details not explained here)

d. On XRD – press FS RELEASE (failsafe release) on the front of the machine; the red light should start blinking

e. Open doors

f. Place a glass slide over the powdered sample on the slide (as an extra precaution should it decide to fall out)

g. Place sample into the holder by pressing on the metal tabs and carefully remove the glass slide

h. Close glass doors

3. Computer

a. Open Data Scan 3.1

b. Click SCAN

c. Enter file ID, setup (09 → Mineral ID), and scan ID

i. Files are automatically saved under directory C:/Datascan/Data-03

d. Standard scan is set for a range of 2-70° at intervals of 0.3° and 0.5 seconds for each interval; this means the time of scan will be 30 minutes

e. After setting up the XRD, press GO to start the scan

f. When the red light is lit up on the equipment INSIDE the XRD, x-rays are being produced

4. Data Analysis

a. Open MDI Jade 6.5

b. FILE → PATTERNS → Find and select data file you want to analyze

c. Click BG (This looks at and will let you remove background noise)

i. If there is not a significant amount of scatter on the left hand side, click BG again

ii. If there is significant deviation above the BG line, alter it by moving the red dots

d. PRINT a copy of the spectrum (click on printer button on toolbar)

e. IDENTIFY → SEARCH/MATCH SETUP → (check) Minerals → OK

f. Match peaks

i. Click on a suggested mineral

ii. If the peaks of that mineral (will be in blue) match well with peaks of your sample, check the box beside that mineral

iii. Continue to do so for each mineral suggested by the program

g. Press the BACK arrow

h. ANALYZE → FIND PEAKS → APPLY → CLOSE

i. VIEW → REPORTS & FILES → PEAK ID (COMPACT)

i. Print this report

j. Make sure you have a backup copy of all data files

5. Before leaving XRD laboratory

a. Fill out log book

b. On XRD –

i. POWER OFF

ii. XRD OFF

iii. kV to 20 (one notch at a time)

iv. mA to 5 (one notch at a time)

c. Turn off computer

Appendix III: Characteristics of Uinta Formation aquifers

Results presented in the table below are hydrologic parameters of Uinta Fm aquifers in the northern Uinta Basin in Utah. Values of porosity, hydraulic conductivity, and transmissivity are directly from Hood (1976). Permeability was calculated from hydraulic conductivity for the purposes of this research. Ranges and median values are presented in the main text in Table 5. Hydraulic conductivity values are horizontal unless noted (V=vertical). Well location in latitude and longitude was determined from township/range notation, and is not accurate to more than 1 section (1 mile or 805 km). Regarding location with respect to (LOC wrt) the DFZ: N is north of, NW is northwest of, and N edge is the northern edge of the DFZ.

WELL LOCATION (Lat, °N/ Long, °W)	*LOC wrt DFZ*	*PORO -SITY (%)*	*HYDRAULIC CONDUCTIVITY (m/s)*	*Calculated PERMEABILITY (m^2)*	*TRANSMISSIVITY (m^2/s)*
40°14.154', 110°12.468'	N	16	1.37E-5 V= 1.22E-6	1.4E-12	4.48E-5
40°10.674', 110°39.600'	NW	23.1	1.22E-5 V= 1.52E-5	1.2E-12	3.99E-5
40°12.414', 110°46.410'	NW	22.3	6.08E-6	6.2E-13	1.99E-5
40°10.674', 111°1.092'	NW	12.7	7.97E-7	8.1E-14	2.62E-5
40°21.114', 110°41.982'	NW	n/d	2.66E-6	2.7E-13	< 0.001
40°16.764', 110°7.950'	N	n/d	1.52E-3	1.5E-10	< 0.249
40°17.844', 110°9.084'	N	n/d	1.52E-3	1.5E-10	0.399
40°15.894', 110°9.078'	N	n/d	2.81E-1	2.9E-08	3.737
40°17.844', 110°10.218'	N	n/d	7.59E-6	7.7E-13	0.004
40°17.844', 110°10.218'	N	n/d	7.97E-4	8.1E-11	0.436

WELL LOCATION (Lat, °N/ Long, °W)	*LOC wrt DFZ*	*PORO -SITY (%)*	*HYDRAULIC CONDUCTIVITY (m/s)*	*Calculated PERMEABILITY (m^2)*	*TRANSMISSIVITY (m^2/s)*
40°15.894', 110°13.608'	N	n/d	7.59E-5	7.7E-12	0.075
40°17.844', 110°22.674'	N	n/d	1.52E-5	1.5E-12	0.006
40°15.894', 110°22.688'	N	n/d	2.66E-5	2.7E-12	0.014
40°15.894', 110°19.272'	N	n/d	7.59E-5	7.7E-12	0.034
40°17.634', 110°27.216'	N	n/d	3.80E-3	3.9E-10	0.598
40°16.764', 110°27.210'	N	n/d	3.80E-3	3.9E-10	0.187
40°16.764', 110°27.210'	N	n/d	7.59E-5	7.7E-12	0.006
40°16.764', 110°28.344'	N	n/d	7.59E-3	7.7E-10	0.386
40°15.894', 110°28.320'	N	n/d	7.59E-5	7.7E-12	0.012
40°15.894', 110°26.070'	N	n/d	3.04E-5	3.1E-12	0.004
40°15.894', 110°24.936'	N	n/d	7.59E-5	7.7E-12	0.009
40°13.284, 109°58.884'	N	n/d	2.28E-5	2.3E-12	0.004
40°15.024', 110°5.682'	N	n/d	3.04E-4	3.1E-11	0.019
40°14.154', 110°7.944'	N	n/d	1.14E-5	1.2E-12	0.004
40°15.024', 110°13.608'	N	n/d	1.90E-5	1.9E-12	0.006
40°13.284', 110°11.334'	N	n/d	1.14E-3	1.2E-10	0.017
40°10.674', 110°11.322'	N	n/d	7.59E-6	7.7E-13	< 0.001
40°14.154', 110°22.662'	N	n/d	3.04E-5	3.1E-12	0.006
40°11.544', 110°22.644'	N	n/d	1.14E-3	1.2E-10	0.002
40°11.544', 110°22.644'	N	n/d	2.28E-6	2.3E-13	0.001
40°14.154', 110°29.454'	N	n/d	7.59E-6	7.7E-13	0.002
40°11.544', 110°30.564'	N	n/d	1.14E-5	1.2E-12	0.001
40°12.414', 110°43.014'	NW	n/d	1.90E-4	1.9E-11	0.024
40°14.154', 110°49.830'	NW	n/d	3.80E-4	3.9E-11	0.066

WELL LOCATION (Lat, °N/ Long, °W)	*LOC wrt DFZ*	*PORO -SITY (%)*	*HYDRAULIC CONDUCTIVITY (m/s)*	*Calculated PERMEABILITY (m^2)*	*TRANSMISSIVITY (m^2/s)*
40°13.284', 110°49.818'	NW	n/d	3.04E-5	3.1E-12	0.009
40°11.544', 110°44.136'	NW	n/d	3.04E-5	3.1E-12	0.006
40°11.544', 110°44.136'	NW	n/d	7.59E-6	7.7E-13	< 0.001
40°11.544', 110°44.136'	NW	n/d	1.90E-5	1.9E-12	0.005
40°15.024', 110°50.976'	NW	n/d	2.28E-3	2.3E-10	0.007
40°14.154', 110°50.964'	NW	n/d	3.42E-4	3.5E-11	0.059
40°13.284', 110°50.952'	NW	n/d	2.28E-5	2.3E-12	0.006
40°13.284', 110°50.952'	NW	n/d	3.04E-5	3.1E-12	0.001
40°13.284', 110°52.080'	NW	n/d	1.14E-6	1.2E-13	< 0.001
40°12.414', 110°52.068'	NW	n/d	3.04E-6	3.1E-13	< 0.001
40°12.414', 110°50.940'	NW	n/d	2.28E-5	2.3E-12	0.017
40°12.414', 110°50.940'	NW	n/d	3.80E-5	3.9E-12	0.019
40°9.804', 110°12.450'	N edge	n/d	2.81E-1	2.9E-08	> 0.137
40°9.804', 110°13.584'	N edge	n/d	3.80E-6	3.9E-13	0.001
40°9.804', 110°14.712'	N edge	n/d	1.90E-4	1.9E-11	0.034
40°9.804', 110°23.760'	N edge	n/d	3.80E-6	3.9E-13	< 0.001

Appendix IV: SEM Images

The purpose of this appendix is to document all of the SEM images taken of the Uinta Basin samples. The notes taken from the samples are included in bot (peper and electronic) versions of this thesis. For the purposes of space, the images are included only in the electronic version.

The samples imaged include: 21, 26, 31, 35, 39, 40, 41, and 48. For each of the samples, a number of images were taken. The sample *image* notation below follows the notation: sample number - picture number. Letters (a, b, c, ...) refer to images that were taken at different scales, but from the same location. For each sample, values of measured porosity (n, given in percent) and mechanical strength (T, tensile strength, given in MPa; C, compressive strength, given in MPa) are reported for easier comparison among the samples. *Screen* designates the distance across the image; for reference, a distance of 15 corresponds to 2200x magnification and 600 corresponds to 550x magnification. *Scale* is the scale shown by the white bar below the image on the left hand side, and is given in μm. The location that the image was taken at is given as *(x,y)*; this is an arbitrary coordinate, but can be used for getting a sense of location between two images from the same sample. *Notes* reports any additional observation that were made about the overall sample.

REFERENCES

Bereskin, S. R., D. E. Taff, and R. L. Ballou, Enhanced fracture permeability and unconventional production potential along the Duchesne Fault Zone, Uinta Basin, Utah, *American Association of Petroleum Geology Buletin*, *77*, (abstract), p. 1442, 1993.

Bieniawski, Z. T., and and I. Hawkes, Suggested methods for determining tensile strength of rock materials, *International Journal of Rock Mechanics and Mining Sciences & Geomechanics Abstracts*, *8*, p. 99-103, 1978.

Brace, W. F., Permeability of crystalline and argillaceous rocks, International Journal of Rock Mechanics, Mineral Science & Geomechanics, Abstracts 17, p. 241-251, 1980.

Bredehoeft, J. D., Neuzil, C. E., and Milly, P. C. D., Regional flow in the Dakota aquifer: A study of the role of confining layers, U.S. Geological Survey Water Supply Paper 2237, 1983.

Bredehoeft, J. D., J. B. Wesley, and T. D. Fouch, Origin of fluid pressure, fracture generation, and the movement of fluids in the Uinta Basin, Utah, in *U. S. Geological Survey Research on Energy Resources, program and abstracts, U. S. Geological Survey Circular*, edited by L. M. H. Carter, p. 13, 1992.

Bredehoeft, J. D., J. B. Wesley, and T. D. Fouch, Simulations of the origin of fluid pressure, fracture generation, and the movement of fluids in the Uinta Basin, Utah, *American Association of Petroleum Geologists Bulletin*, *78*, p. 1729-1747, 1994.

Bruhn, R. L., M. D. Picard, and J. S. Isby, Tectonics and Sedimentology of Uinta Arch, western Uinta Mountains and Uinta Basin, in *American Association of Petroleum Geologists Memoir 41: Paleotectonics and Sedimentation in the Rocky Mountain region, United States*, p. 333-352, 1986.

Bruhn, R. L., W. T. Parry, and M. P. Bunds, Tectonics, fluid migration, and fluid pressure in a deformed forearc basin, Cook Inlet, Alaska, *Geological Society of America Bulletin*, *112*, p. 550-563, 2000.

Campbell, J. H., *Lawrence Livermore National Laboratory Report UCRL-52089, Part 2*, Lawrence Livermore National Laboratory, Livermore, CA, 1978.

Chidsey, T. C., Jr., and Michael D. Laine, The Fractured Green River and Wasatch Formations of the Uinta Basin, Utah: Targets for horizontal drilling, in *Hydrocarbon and Mineral Resources of the Uinta Basin, Utah and Colorado*: *Utah Geological Association Guidebook*, vol. 20, edited by T. D. Fouch, V. F. Nuccio, and T. C. Chidsey, Jr., p. 123-134, Utah Geological Association, Salt Lake City, 1992.

Chen, C., E. Pan, and B. Amdei, Determination of deformability and tensile strength of anisotropic rock using Brazilian tests, *International Journal of Rock Mechanics and Mining Sciences & Geomechanics Abstracts*, *35*, p. 43-61, 1998a.

Chen, C., E. Pan, and B. Amadei, Fracture mechanics analysis of cracked discs of anisotropic rock using the boundary element method, *International Journal of Rock Mechanics and Mining Sciences & Geomechanics Abstracts*, *35*, p. 195-218, 1998b.

Clem, K., Oil and gas production summary of the Uinta Basin, in *Geology and Energy Resources, Uinta Basin of Utah, Utah Geological Association Publication 12*, edited by M. D. Picard, p. 159-167, 1985.

Dane, C. H., Stratigraphic and facies relationships of Upper part of Green River Formation and Lower part of Uinta Formation in Duchesne, Uintah, and Wasatch Counties, Utah, *Bulletin of the American Association of Petroleum Geologists*, *38*, p. 405-425, 1954.

Fouch, T. D., Lithofacies and related hydrocarbon accumulations in Tertiary strata of the western and central Uinta Basin, Utah, in *Deep Drilling Frontiers of the Central Rocky Mountain, Rocky Mountain Association of Petroleum Geologists Symposium*, edited by D. W. Bolyard, p. 163-174, 1975.

Fouch, T. D., V. F. Nuccio, J. C. Osmond, L. MacMilan, W. B. Cashion, and C. J. Wandrey, Oil and gas in Uppermost Cretaceous and Tertiary Rock, Uinta Basin, Utah, in *Hydrocarbon and Mineral Resources of the Uinta Basin, Utah and Colorado*: *Utah Geological Association Guidebook*, vol. 20, edited by T. D. Fouch, V. F. Nuccio, and T. C. Chidsey, Jr., p. 9-47, Utah Geological Association, Salt Lake City, 1992a.

Fouch, T. D., C. J. Wandrey, J. K. Pitman, V. F. Nuccio, J. W. Schmoker, D. D. Rice, R. C. Johnson, and G. L. Dolton, Natural gas accumulations in low-permeability Tertiary and Cretaceous (Campanian and Maastrichtian) rock, Uinta Basin, *Report DOE/MC/20422-3051 (DEC92001132)*, 81 p., Office of Fossil Energy, U. S. Department of Energy, 1992b.

Fouch, T. D., V. F. Nuccio, D. E. Anders, D. D., J. K. Pitman, and R. F. Mast, Green River(!) Petroleum System, Uinta Basin, Utah, U.S.A., in *American Association of Petroleum Geologists Memoir 60: The Petroleum System- from Source to Trap*, p. 399-421, 1994.

Garven, G., Continental scale groundwater flow and geologic processes, Annual Review of Earth and Planetary Sciences 25: p. 89-117, 1995.

Glover, K. C., Ground-water flow in the Duchesne River-Uinta aquifer, Uinta Basin, Utah and Colorado, *U. S. Geological Survey Water-Resources Investigation 92-4161*, 24 p., 1996.

Gries, Robbie, North-south compression of Rocky Mountain foreland structures, in *Rocky Mountain Association of Geologists: Rocky Mountain Foreland Basins and Uplifts,* edited by Lowell, p. 9-32, 1983a.

Gries, Robbie, Oil and gas prospecting beneath Precambrian of foreland thrust plates in Rocky Mountains, *The American Association of Petroleum Geologists Bulletin*, *67*, p. 1-28, 1983b.

Groeger, A. Y., Structure and geomorphology of the Duchesne Graben, Uinta Basin, Utah, Masters of Science Thesis, 70 pp., University of Utah, Salt Lake City, 1997.

Groeger, A. and R. L. Bruhn, Structure and geomorphology of the Duchesne graben, Uinta basin, Utah and its enhancement of a hydrocarbon reservoir, *American Association of Petroleum Geologists Bulletin*, *85*, p. 1661-1678, 2001.

Gunsallus, K. L. and F. H. Kulhawy, A comparative evaluation of rock strength measures, *International Journal of Rock Mechanics and Mining Sciences & Geomechanics Abstracts*, *21*, p. 233-248, 1984.

Hintze, L. F., Geologic Highway map of Utah, *Brigham Young University Geology Studies- Special Publication 3*, (calculated) scale 1:1013760, 1997.

Hood, J. W., Characteristics of aquifers in the northern Uinta Basin area, Utah and Colorado, *United States Geological Survey Technical Publication 53*, 1976.

Hubbert, M. K., and W. W. Rubey, Role of fluid pressure in mechanics of overthrust faulting, *Bulletin of the Geological Society of America*, *17*, p. 115-166, 1959.

Hulen, J., *Internal report prepared for* Advanced fracture modeling in the Uinta Basin (Utah) for optimized primary and secondary recovery, Final Report prepared for U. S. Department of Energy, *DOE/PC/91008-21, Contract Number DE-AC22-94PC91008, Subcontract Number G4S51729*, 1998.

Ingebritsen, S. E., and W. E. Sanford, Groundwater in Geologic Processes, Cambridge, Cambridge University Press, Cambridge, United Kingdom, 1998.

Ismail, M. A., H. A. Joer, M. F. Randolph, and A. Meritt, Cementation of porous materials using calcite, *Geotechniques*, *52*, p. 313-324, 2002.

Jaeger, J. C. and N. G. W. Cook, Fundamentals of Rock Mechanics, London, Chapman, and Hall Ltd, United Kingdom, 1976.

Johnson, R. C., and V. F. Nuccio, Surface vitrinite reflectance study of the Uinta and Piceance Basins area, eastern Utah and western Colorado– Implications for the development of Laramide basins and uplifts, *U. S. Geological Survey Bulletin 1787-DD: Evolution of Sedimentary Basins- Uinta and Piceance basins*, 38 p., 1993.

Johnson, S. Y., Phanerozoic evolution of sedimentary basins in the Uinta-Piceance Basin region, northwest Colorado and northeastern Utah, *U. S. Geological Survey Bulletin 1787-FF: Evolution of Sedimentary Basins- Uinta and Piceance basins*, 38 p., 1992.

Kranz, R. L., J. S. Saltzman, and J. D. Blacic, Hydraulic diffusivity measurements on laboratory rock samples using an oscillating pore pressure method, *International Journal of Rock Mechanics and Mineral Sciences and Geomechanics Abstracts, 27*, p. 345-352, 1990.

Lemmon, R. E. (Technology Manager) and others, Terra Tek, Inc., Advanced fracture modeling in the Uinta Basin (Utah) for optimized primary and secondary recovery, Final Report prepared for U. S. Department of Energy, *DOE/PC/91008-21, Contract Number DE-AC22-94PC91008, Subcontract Number G4S51729*, 39 p., 1998.
Lucas, P. T., and J. M. Drexler, Altamont-Bluebell: A major, naturally fractured stratigraphic trap, Uinta Basin, Utah, in *American Association of Petroleum Geologists Memoir 24: North American Oil and Gas Fields*, p. 121-135, 1976.

McPherson, B. J. O. L., A three-dimensional model of the geologic and hydrodynamic history of the Uinta Basin, Utah: Analysis of overpressures and oil migration, Doctor of Philosophy Dissertation, 119 p., University of Utah, Salt Lake City, 1996.

McPherson, B. J. O. L., and G. Garven, Hydrodynamics and overpressure mechanisms in the Sacramento Basin, California, *American Journal of Science, 299*, p. 429-466, 1999.

McPherson, B. J. O. L., Lichtner, P. C., Forster, C. B., Cole, B. S., Regional-Scale Permeability by Heat Flow Calibration in the Powder River basin, Wyoming, Geophys. Res. Lett., v. 28 , No. 16 , p. 3211-3214, 2001.

McPherson, B. J. O. L., and John D. Bredehoeft, Overpressures in the Uinta Basin, Utah: Analysis using a three-dimensional basin evolution model, *Water Resources Research, 37*, p. 857-871, 2001.

McPherson, B. J., and the EarthLab Steering Committee, Earthlab: A subterranean laboratory and observatory to study microbial life, fluid flow, and rock deformation, Geosciences Professional Services, Inc., 60 p., 2003.

Middleton, G. V., and Wilcook, P. R., *Mechanics in the Earth and Environmental Sciences*, Cambridge University Press, Cambridge, Great Britain, 1994.

Monson, B., and J. Parnell, The origin of gilsonite vein deposits in the Uinta Basin, Utah, in *Hydrocarbon and Mineral Resources of the Uinta Basin, Utah and Colorado*: *Utah Geological Association Guidebook*, vol. 20, edited by T. D. Fouch, V. F. Nuccio, and T. C. Chidsey, Jr., p. 257-270, Utah Geological Association, Salt Lake City, 1992.

Morgan, C. D., K. P. McClure, S. R. Bereskin, M. D. Deo, K. Weller, Reservoir Characterization of the Lower Green River Formation, southwest Uinta Basin, Utah: Biannual Technical Progress Report, Contract DE-AC26-98BC15103, Submitted by Utah Geological Survey, Prepared for U. S. Department of Energy, 26 p., 2000.

Mozley, P. S., L. B. Goodwin, M. Heynekamp, and W. C. Haneburg, Using the spatial distribution of calcite cements to infer paleoflow in fault zones: Examples from the Albuquerque Basin, New Mexico, Abstract, *American Association of Petroleum Geologists Annual Meeting 13*, vol. 80, p. A102, 1996.

Mozley, P. S., and J. M. Davis, Relationship between oriented calcite concretions and permeability correlation structure in an alluvial aquifer, Sierra Ladrones Formation, New Mexico, *Journal of Sedimentary Research, 66*, p. 11-16, 1996.

Narr, W., and J. B. Currie, Origin of fracture porosity- Example from Altamont Field, Utah, *American Association of Petroleum Geologists Bulletin, 66*, 1231-1247, 1982.

Neuzil, C. E., How permeable are clays and shales?, Water Resources Research, vol. 30, no. 2, p. 145-150, 1994.

Neuzil, C. E., Abnormal pressures as hydrodynamic phenomena, *American Journal of Science, 295*, p. 742-786, 1995.

Pitman, J. K., K. J. Franczyk, and D. E. Anders, Marine and nonmarine gas-bearing rocks in Upper Cretaceous Blackhawk and Neslen formations, eastern Uinta Basin, Utah, *American Association of Petroleum Geologists Bulletin*, *71*, p. 76-94, 1987.

Pitman, J. K., T. D. Fouch, and M. B. Goldhaber, Depositional setting and diagenetic evolution of some Tertiary unconventional reservoir rocks, Uinta Basin, Utah, *American Association of Petroleum Geologists Bulletin*, *66*, 1581-1596, 1982.

Pollard, D. D., and A. Aydin, Progress in understanding jointing over the past century, *Geological Society of America Bulletin*, *100*, p. 1181-1204, 1988.

Ray, R. G., B. H. Kent, and C. H. Dane, Stratigraphy and photograph-geology of the southwestern part of the Uinta basin, Duchesne and Uintah counties, Utah, *U. S. Geological Society Oil and Gas Inventory Map OM 171*, scale 1:63360, 2 plates, 1956.

Ruble, T. E., M. D. Lewan, and R. P. Philip, New insights on the Green River Petroleum system in the Uinta basin from hydrous pyrolysis experiments, *American Association of Petroleum Geologists Bulletin*, *85*, p. 1333-1371, 2001.

Ryder, R. T., T. D. Fouch, and J. H. Elison, Early Tertiary sedimentation in the western Uinta Basin, Utah, *Geological Society of America Bulletin, 87*, p. 496-512, 1976.

Schmidt, V., and D. A. McDonald, The role of secondary porosity in the course of sandstone diagenesis, *Society of Ecomonic Paleontologists and Moneralogists 26: Aspects of Diagenesis*, (Published by) Society for Sedimentary Geology, Tulsa, OK, 1979.

Secor, D. T., Jr., Role of Fluid Pressure in Jointing, *American Journal of Science*, *263*, p. 633-646, 1965.

Sibson, R. H., Structural permeability of fluid-driven fault-fracture meshes, *Journal of Structural Geology*, 18, p. 1031-1042, 1996.

Sibson, R. H., Brittle failure mode plots for compressional and extensional tectonic regimes, *Journal of Structural Geology*, 20, p. 655-660, 1998.

Spencer, C. W., Hydrocarbon Gereration as a Mechanism for Overpressuring in Rocky Mountain Region, *American Association of Petroleum Geologists Bulletin*, *71*, p. 368-388, 1987.

Sterling, J., Fracture generation and fluids in the Spraberry Formation, Midland Basin, Texas, Master of Science Independent Study, 96 p., New Mexico Institute of Mining and Technology, Socorro, 2000.

Sweeney, J. J., A. K. Burnham, and R. L. Braun, 1987, A model of hydrocarbon generation from type I kerogen: application to the Uinta Basin, Utah, *American Association of Petroleum Geologists Bulletin*, *71*, p. 967-985, 1987.

Verbeek, E. R., and M. A. Grout, Structural Evolution of Gilsonite Dikes in the Eastern Uinta Basin, Utah, in *Hydrocarbon and Mineral Resources of the Uinta Basin, Utah and Colorado*: *Utah Geological Association Guidebook*, vol. 20, edited by T. D. Fouch,

V. F. Nuccio, and T. C. Chidsey, Jr., p. 237-255, Utah Geological Association, Salt Lake City, 1992.

Verbeek, E. R., and M. A. Grout, Geometry and structural evolution of gilsonite dikes in the Eastern Uinta Basin, Utah, *U. S. Geological Survey Bulletin 1787-HH: Evolution of sedimentary basins- Uinta and Picenace Basins*, 42 p., 1993.

Willett, S. D., and D. S. Chapman, On the use of thermal data to resolve and delineate hydrologic flow systems in sedimentary basins: an example from the Uinta Basin, Utah, *in* Hitchon, B., S. Bachu, and C. Sauveplane, ed., Proceedings of the Third annual Canandian/American Conference on Hydrogeology; Hydrology of Sedimentary Basins - Applications to Exploration and Exploitation: Dublin, Ohio, National Water Well Association, p. 159-168, 1987.

Ziegler Chemical and Mineral Corporation, "Physical properties of gilsonite", (Online) http://www.zieglerchemical.com/phyprops.htm, Accessed 24 March 2004.

Zoback, M. L., and M. Zoback, State of Stress in the Conterminous United States, in *Journal of Geophysical Research 85*: *Magnitude of deviatoric stresses in the Earth's crust and uppermost mantle*, 6113-6156, 1980.